

## REMOTE SENSING OF SHALLOW-MARINE IMPACT CRATERS ON MARS

Except where reference is made to the work of others, the work described in this thesis is my own or was done in collaboration with my advisory committee. This thesis does not include proprietary or classified information.

---

Germari de Villiers

Certificate of Approval:

---

Luke J. Marzen, Co-Chair  
Associate Professor  
Geography

---

David T. King, Jr., Co-Chair  
Professor  
Geology

---

Willis E. Hames  
Professor  
Geology

---

George T. Flowers  
Interim Dean  
Graduate School

REMOTE SENSING OF SHALLOW-MARINE IMPACT CRATERS ON MARS

Germari de Villiers

A Thesis

Submitted to

the Graduate Faculty of

Auburn University

in Partial Fulfillment of the

Requirements for the

Degree of

Master of Science

Auburn, Alabama  
December 17, 2007

REMOTE SENSING OF SHALLOW-MARINE IMPACT CRATERS ON MARS

Germari de Villiers

Permission is granted to Auburn University to make copies of this thesis at its discretion, upon request of individuals or institutions at their expense. The author reserves all publication rights.

---

Signature of Author

---

Date of Graduation

## VITAE

Germari de Villiers, daughter of Gerard and Gerda de Villiers, was born on 28 February, 1983, in Pretoria, South Africa, as the first of three daughters. She grew up in Randburg, South Africa, and attended both Laerskool Unika and Hoërskool Randburg. She graduated from Reeltown High School, Alabama, in 2001 and matriculated from Greenside High School, Johannesburg, in 2002. She graduated from the University of Pretoria in 2005 with a Bachelor of Science degree in Geology and entered Auburn University Graduate School in January 2006.

## THESIS ABSTRACT

### REMOTE SENSING OF SHALLOW-MARINE IMPACT CRATERS ON MARS

Germari de Villiers

Master of Science, December 17, 2007  
(B.Sc., University of Pretoria, 2005)

161 Typed Pages

Directed by David T. King, Jr. and Luke J. Marzen

Impact craters are common on solid planetary bodies in our solar system and are one of the most important physical features from which the surface history of these planetary bodies can be deduced. Remote sensing is a crucial tool in planetary science and is essential in the detailed study of impact structures on planetary surfaces.

Oceans have been proposed to have existed on Mars during its history, the shorelines of which would coincide roughly with the crustal dichotomy that divides the smooth, northern lowlands with the cratered, southern highlands. Arabia Terra is a region on Mars that straddles the dichotomy and three proposed shorelines are located in the area. If Mars had a large ocean during its early history, Arabia Terra would be a

continental shelf area and hence an ideal location for the preservation of shallow-marine impact craters.

Shallow-marine impact craters on Earth exhibit characteristic morphological features. Due to the sub-marine formation and the influence of the water column, the morphologies of these craters are distinctly different from that of craters formed on land. Common attributes of marine impact craters include features of wet mass movement such as gravity slumps and debris flows; radial gullies flowing into the crater depression; resurge deposits and blocks of dislocated materials; a central peak terrace or peak ring terrace; crater rim collapse or breaching of the crater wall; and subdued topography. These features are visible from orbital imagery, and can thus be used to evaluate craters on Mars for possible marine origin. This study designed a simple quantification system that can be used to crudely judge and rank shallow-marine impact crater candidates based on the features observed in previously proposed shallow-marine impact crater candidates as well as features observed in terrestrial analogs. With the use of Mars Orbiter Laser Altimeter topographic data and Mars Orbiter Camera and Thermal Emission Imaging System imagery, the area bounded by 20° and 40° north as well as 20° west and 20° east is explored for evidence of shallow-marine impact craters. Based on the quantification system, 77 potential shallow-marine impact craters are found within Arabia Terra of which nine exemplary candidates were ranked with total scores of 70% or more.

## ACKNOWLEDGEMENTS

The author would like to thank Dr. David King, Dr. Luke Marzen, and Dr. Willis Hames, members of her thesis committee, for endless support and guidance in this endeavor. The author is exceedingly grateful to Dr. David King, who took particular effort to ensure that the time spent at Auburn University was a positive experience. The author is grateful also to Dr. Luke Marzen for taking the initiative to apply for funding to NASA's Experimental Program to Stimulate Competitive Research (EPSCoR). Due to his resourcefulness, this study was funded by the Alabama Space Grant Consortium through NASA EPSCoR.

As far as inspiration goes, the author would like to acknowledge Jens Ormö who made valuable suggestions and contributions, and who essentially planted the seed for this study. The author would like to thank Trent Hare and ArunKumar Jayakeerthy for assistance with image processing as well as Filippo Bianchi and Gerard de Villiers for valuable comments and suggestions concerning software applications. The author acknowledges the extensive use of Mars Orbiter Camera (MOC) images that are available at [http://www.msss.com/moc\\_gallery/](http://www.msss.com/moc_gallery/) as well as THEMIS images that are available at <http://themis.asu.edu/mars-bin/webmap.pl>.

The author would like to dedicate this thesis to her family who stood closely by her through these challenging two years:

“Pappa and Mamma, thank you for inspiring me to work and teaching me to dream. Lorida and Marina, thank you for always cheering me up and making me laugh. Filippo, thank you for loving me with all that you have and letting me be your crazy, South African scientist. And finally, to my Heavenly Father, for showing me that all things are possible through Him.”



Journal style used: Meteoritics and Planetary Science

Computer software used: Adobe® Reader® 7.0  
ESRI® ArcGIS™ 9.2  
ISIS 2  
Microsoft® Office Excel 2003  
Microsoft® Office Power Point® 2003  
Microsoft® Office Word 2003  
GRIDVIEW  
WinZip®

## TABLE OF CONTENTS

LIST OF FIGURES .....	xiii
LIST OF TABLES .....	xviii
INTRODUCTION .....	1
Impact Craters.....	3
Distribution of craters.....	3
Types of craters .....	4
Objectives .....	13
Significance .....	18
LITERATURE REVIEW .....	19
Water on Mars .....	20
Oceans on Mars .....	24
Large Noachian ocean and smaller Hesperian ocean.....	24
Smaller local lakes.....	31
Evidence for oceans on Mars .....	31
Physical properties and characteristics of shallow-marine impact craters .....	34
Depth-diameter ratios .....	37
Slopes .....	39
Ejecta deposits .....	40
Wet Mass Movement (WMM).....	42

Radial Gullies (RG).....	43
Resurge Deposits (RD).....	44
Central Terrace (CT) .....	44
Rim Collapse (RC).....	45
Subdued Topography (ST) .....	45
Examples of shallow-marine craters.....	46
Chesapeake Bay.....	47
Chicxulub .....	48
Lockne .....	48
Mjølfnir .....	49
Wetumpka.....	49
Remote Sensing .....	50
Summary .....	54
METHODS .....	55
Background.....	56
Mars Global Surveyor .....	57
Mars Odyssey .....	59
Data Acquisition .....	60
MOLA data.....	60
MOC and THEMIS data.....	64
Data Analysis.....	67
Data Interpretation.....	69

RESULTS .....	76
Ormö et al.'s candidate crater results .....	78
Results from Set A.....	80
Results from Set B.....	83
Exemplary candidates.....	87
INTERPRETATIONS .....	91
Type I candidates.....	93
Crater D .....	93
Crater 24.....	97
Crater 66.....	101
Type II candidates.....	105
Crater 6.....	105
Crater 17.....	108
Crater 45.....	112
Crater 54.....	116
Crater 55.....	120
Type III candidates .....	124
Crater 58.....	124
Summary.....	128
CONCLUSIONS.....	130
REFERENCES .....	133

## LIST OF FIGURES

Fig. 1. Morphology of a complex crater (b) differs substantially from that of a simple crater (a). Modified from French (1998).....	6
Fig. 2. Different layers present in the target (A-F) as well as the ejecta blanket (G) of a complex crater. Also shown are a terrace (t) and a block of rim material (b) both products of slumping. From Pike (1980). .....	6
Fig. 3. Cross-section of the inverted sombrero morphology observed at Chesapeake Bay impact crater. The section runs from the western rim to the central peak due east. The wide annular trough and the slumped blocks where the rim collapsed are shown. From Horton et al. (2006).....	9
Fig. 4. Mars topographic map as viewed from the equator and central meridian (a). Elevation increases from blue to red. The study area lies mainly within Arabia Terra, (shown in b). Modified from MOLA Topographic Map, GIS I-2782, USGS.....	15
Fig. 5. Regional geological map of the northern plains of Mars, as viewed from the North Pole. Modified from Tanaka et al. (2005). .....	17
Fig. 6. Locations of shorelines proposed by Parker et al. (1989) as viewed from the North Pole. A thick black line indicates Contact 1, whereas Contact 2 is the thinner grey line. The Ismenius Lacus quadrangle, which forms the upper left hand corner of the study area, is shaded. From Parker et al. (1989).....	25
Fig. 7. Locations of two mapped shorelines, here labeled Contact 1 and Contact 2, as viewed from the equator in an equidistant cylindrical projection of the surface. Meridiani shoreline (as proposed by Clifford and Parker, 2001) is also shown. From Ormö et al. (2004).....	27
Fig. 8. Locations of shorelines proposed by Fairén et al. (2003) as viewed from the North Pole. Contact 1 (now referred to as Shoreline 1) is indicated by a solid black line, whereas Contact 2 (now referred to as Shoreline 2) is the thinner grey line. The dashed line north of Arabia Terra is the original location of Contact 1, but has since been modified to run further south (see discussion). From Fairén et al. (2003). .....	28
Fig. 9. Flooding of the northern lowlands (a) up to a maximum depth of 1490 m (filled to level of Contact 2); and (b) up to a maximum depth of 3570 m (filled to level of Contact 1) (Head et al. 2003). .....	30
Fig. 10. Stages (A-H) of formation, excavation, and modification for marine impact	

craters. Note the inverted sombrero morphology of the crater. From Johnson (2007)...	35
Fig. 11. Parameters in depth-diameter calculations include rim-rim diameter and rim height. Also shown here are $d_s$ (depth of crater compared to surrounding topography) and $d_r$ (depth of crater from rim). From Boyce et al. (2005).....	37
Fig. 12. Illustrated difference between a slump (left) and a flow (right). Modified from Geology Web Pages at <a href="http://www.nicholas.duke.edu/eos/geo41/geo41.htm">http://www.nicholas.duke.edu/eos/geo41/geo41.htm</a> (accessed 2007).....	42
Fig. 13. Resurge gullies as observed in the Lockne and Kamensk craters in Eurasia. From Ormö and Muinonen (2000).....	43
Fig. 14. Locations of selected terrestrial analogues for Martian shallow-marine craters – three out of five are located on the American plate, and the remaining two on the Scandinavian plate. ....	46
Fig. 15. Spacecraft that have gone to Mars include Mariner 4, launched 28 November 1964 (a); Viking Orbiter Lander 1 and 2, launched 20 August 1975 and 9 September 1975 respectively (b); Mars Global Surveyor, launched 7 November 1996 (c); and Mars Odyssey (still operating), launched 7 April 2001 (d). All images from NASA (available from <a href="http://mars.jpl.nasa.gov/gallery/spacecraft/index.html">http://mars.jpl.nasa.gov/gallery/spacecraft/index.html</a> ).....	53
Fig. 16. Timeline depicting the stages in Mars exploration by Viking Orbiters 1 and 2 (V1 and V2), Mars Global Surveyor (MGS), and Mars Odyssey (MO). White areas indicate cruise time, and darker areas indicate sensor-operating time.....	56
Fig. 17. Different data products that can be derived from raw MOLA data. MEGDRs are used in a GIS, and are therefore used in this study. ....	61
Fig. 18. Tiling scheme for the 128 pixel/degree MEGDRs from the Planetary Data System (PDS), indicating the two tiles that are used as base maps in this study.....	63
Fig. 19. The study area falls within four of the central quadrangles in the Northern Hemisphere – Mare Acidalium, Oxia Palus, Ismenius Lacus, and Arabia. From Malin Space Science Systems (MSSS). ....	65
Fig. 20. The locations of Craters A, B, C, and D (as indicated by Ormö et al., 2004) in Viking images F529A09 and F072A32, respectively. Images from the Planetary Data System (PDS).....	69
Fig. 21. THEMIS raster image of a Crater B on top of MOLA DEM (a) and georeferenced MOC image draped over THEMIS image (b).....	70
Fig. 22. Subdued topography and no elevated rim (a) (E0600102). Central terrace (b) (V12594005). Large radial gullies (c) (R0500631). Large-scale wet mass movement (d)	

(R1402326). Images from Malin Space Science Systems (MSSS) and PIGWAD. ....	72
Fig. 23. Weighted distribution of the six classes of shallow-marine crater characteristics. Note that wet mass movement (WMM) is split into two sub-categories.....	74
Fig. 24. Locations of potential shallow-marine impact craters in relation to the three shorelines proposed by Parker et al. (1989) as well as Edgett and Parker (1997). North polar projection hill-shade base map is from the USGS and is based on MOLA topographic data. Study area is shown by the gray rectangle.....	77
Fig. 25. Stacked columns with individual contributions to the overall rank for the craters proposed by Ormö et al. (2004).....	79
Fig. 26. Stacked columns with individual contributions to the overall rank for the craters in Set A. ....	82
Fig. 27. Stacked columns with individual contributions to the overall rank for the craters in Set B.....	86
Fig. 28. Breakdown of characteristics present in Crater D and legend with color-coded list of features.....	87
Fig. 29. Breakdown of characteristics present in the exemplary candidates (see legend in Fig. 28).....	88
Fig. 30. Locations of exemplary candidates on MOLA topographic raster image.....	92
Fig. 31. Composite image for Crater D with MOLA base map and MOC wide and narrow-angle images as high-resolution overlays.....	93
Fig. 32. A close-up of Fig. 30 showing MOC narrow angle image overlay in more detail. Radial gullies are indicated by white dashed lines and features labeled A-B are discussed in text. ....	94
Fig. 33. Profile view of Crater D showing varying depth (in km) with variation in latitude (in degrees) from north (left) to south (right). Vertical exaggeration is 21:1. ....	96
Fig. 34. Composite image for Crater 24 with MOLA base map, THEMIS image and MOC narrow-angle images as high-resolution overlays. ....	97
Fig. 35. A close-up of Fig. 34 showing MOC narrow angle image overlay in more detail. Radial gullies are indicated by white dashed lines and features labeled A-E are discussed in text. ....	99
Fig. 36. Profile view of Crater 24 showing varying depth (in km) with variation in latitude (in degrees) from north to south. Vertical exaggeration is 9:1. ....	100

Fig. 37. Composite image for Crater 66 with MOLA base map and THEMIS images as high-resolution overlays.....	101
Fig. 38. A close-up of Fig. 36 showing THEMIS image overlay in detail. Features labeled A-E are discussed in the text. ....	102
Fig. 39. Profile view of Crater 66 showing varying depth (in km) with variation in latitude (in degrees) from north to south. Vertical exaggeration is 8:1. ....	103
Fig. 40. Composite image for Crater 6 with MOLA base map, THEMIS image, and MOC narrow-angle images as high-resolution overlays. ....	105
Fig. 41. Close-up of Fig. 40 showing MOC and THEMIS image overlays in detail. Features labeled A-B are discussed in the text. ....	106
Fig. 42. Profile view of Crater 6 showing varying depth (in km) with variation in latitude (in degrees) from north to south. Vertical exaggeration is 10:1. ....	107
Fig. 43. Composite image for Crater 17 with MOLA base map, THEMIS image, and MOC narrow-angle images as high-resolution overlays. ....	108
Fig. 44. Close-up of Fig. 42 showing MOC image overlay over THEMIS. Features labeled A and B are discussed in the text. ....	110
Fig. 45. Profile view of Crater 17 showing varying depth (in km) with variation in latitude (in degrees) from north to south. Vertical exaggeration is 29:1. ....	111
Fig. 46. Composite image for Crater 45 with MOLA base map and THEMIS images as high-resolution overlays.....	112
Fig. 47. Close-up of Fig. 46 showing THEMIS image overlay. Features labeled A-C are discussed above.....	114
Fig. 48. Profile view of Crater 45 from north to south. Vertical exaggeration is 13:1. ....	115
Fig. 49. Composite image for Crater 54 with MOLA base map THEMIS image as a high-resolution overlay. ....	116
Fig. 50. Close-up of Fig. 49 showing THEMIS image overlay. Features labeled A-D are discussed in the text above.....	118
Fig. 51. Profile view of Crater 54 from north to south. Vertical exaggeration is 6:1... ..	119
Fig. 52. Composite image for Crater 55 with MOLA base map and MOC narrow-angle images as high-resolution overlays.....	120
Fig. 53. Close-up of Fig. 52 showing MOC image overlay. Features labeled A and B are	



mentioned in the text above. ....	122
Fig. 54. Profile view of Crater 55 showing varying depth (in km) with variation in latitude (in degrees) from north to south. Vertical exaggeration is 17:1. ....	123
Fig. 55. Composite image for Crater 58 with MOLA base map and MOC wide and narrow-angle images as high-resolution overlays. ....	124
Fig. 56. Close-up of Fig. 54 showing MOC and THEMIS image overlay on top of MOLA topography. Features labeled A and B are discussed in the text. Radial gullies are indicated with white dashed lines. ....	126
Fig. 57. Profile view of Crater 58 showing varying depth (in km) with variation in latitude (in degrees) from north to south. Vertical exaggeration is 15:1. ....	127
Fig. 58. Spatial distribution of candidate craters shown by type. Type I craters are shown in blue, type II craters shown in green, and type III craters shown in red. ....	128

## LIST OF TABLES

Table 1. Marine impact craters on Earth. Modified from Ormö and Lindström (2000) and Dypvik and Jansa (2003).....	12
Table 2. Geological time-scale for Mars based on cratering chronology. Modified from Hartmann and Neukum (2001). .....	16
Table 3. Main events associated with impacts into aqueous targets (adapted from Artemieva and Shuvalov 2002). .....	36
Table 4. Classification of ejecta morphology according to Barlow’s Catalog of Large Martian Impact Craters and examples from THEMIS images (Barlow 2006a). .....	41
Table 5. Physical properties of selected terrestrial shallow-marine impact craters.....	47
Table 6. Common remote sensing fields in the infrared section of the electromagnetic radiation spectrum and their associated wavelengths. ....	51
Table 7. Instrument specifics in terms of resolution for MOLA, MOC, and THEMIS (Malin et al. 1992; Abshire et al. 2000; Christensen et al 2002; Kirk 2005).....	57
Table 8. Evaluation of Ormö et al.’s (2004) potential shallow-marine crater candidates. ....	78
Table 9. Evaluation of characteristics of small shallow-marine crater candidates. Exemplary ranking candidates are shown in italics. ....	81
Table 10. Evaluation of characteristics of medium shallow-marine crater candidates... ..	81
Table 11. Evaluation of characteristics of large shallow-marine crater candidates.....	82
Table 12. Evaluation of characteristics of small shallow-marine crater candidates. ....	84
Table 13. Evaluation of characteristics of large shallow-marine crater candidates.....	84
Table 14. Evaluation of characteristics of medium shallow-marine crater candidates. Exemplary ranking candidates are shown in italics. ....	85
Table 15. Physical parameters as measured from MOLA data for exemplary candidates. All depths are negative, in other words, below mean surface level (see text for explanation of abbreviations).....	89

Table 16. Depths as measured from MOLA data for exemplary candidates and estimated depths as calculated from depth-diameter relationships in literature (Garvin 2000; Howenstein 2006). Factors of difference (see text) are given for each estimation..... 90

## INTRODUCTION

The study of impact craters began in 1609 when Galileo Galilei turned his telescope to the moon for the first time. His discoveries, documented in *Sidereus Nuncius* in 1610, changed the world's perspective of the universe and became the foundation upon which the science of impact craters was built (Koeberl 2001).

The formation of cosmic impact structures is a major geologic process not only on Earth, but also on the solid surfaces of other planetary bodies throughout the solar system. Impact crater formation is one of the most fundamental processes in the solar system and is thought to be responsible for many important characteristics of the terrestrial planets. Impact events have been responsible for the formation and preservation of numerous ore deposits on Earth, and impacts have been responsible for at least one major extinction in the Earth's history (French 1998). Even the formation of our Moon is commonly considered to have occurred when a large impactor collided with Earth (Hartmann and Davis 1975; Canup and Asphaug 2001). Furthermore, physical evidence of the impact processes, in the shape of nearly circular rimmed depressions (Melosh 1980), can be seen on all solid planetary bodies in our solar system, and craters are still formed throughout the solar system today (Melosh 1989).

Impact craters are the dominant physical features on most, if not all, solid planetary surfaces and are one of the most important physical features from which the surface history and composition of these bodies can be deduced. The study of craters can provide important information about the evolutionary history of planetary bodies in our solar system, and since the impact process has been described and studied in detail, the initial shape of these features can be predicted (Malin et al. 1992; Boyce et al. 2005). The study of impact craters plays a large role in understanding the properties of the target surfaces, their ages, and the physical conditions of these surfaces at the time of impact.

The physical conditions of planetary surfaces can be deduced from impact craters by looking at the morphology of these craters. One type of physical condition that is particularly interesting is surface water cover. A layer of water on the surface influences the shape of the final crater (Ormö et al. 2002), and thus the morphology of craters formed in terrestrial environments differs from that of craters formed in marine environments. This project investigates the morphology of impact craters in an area on Mars suggested to be a shallow continental shelf environment (Parker 1989; Edgett and Parker 1997; Fairén et al. 2003).

A brief discussion on the background of impact cratering introduces this study, followed by a discussion on the objectives and significance of the project.

## **Impact Craters**

### *Distribution of craters*

Scientists assume that comets and asteroids strike all regions of a planetary body at approximately the same rate over a given span of time and thus the crater density of a planetary surface indirectly indicates the relative age of that surface (Hartmann 1977; Hartmann and Neukum 2001). This flux can change over time, but simply stated, regions with higher crater densities tend to be older than regions with lower crater densities. For example, the highly cratered surface of Mercury is expected to be much older than that of the Earth. Furthermore, different planets have different rates of crater formation depending on factors such as distance from the sun and atmospheric density. The presence of an atmosphere on a planetary body shields the surface from some impacts by eliminating smaller impactors before they can strike the surface. Thus, one can assume that Mercury's surface is not only older than that of the Earth, but also Mercury probably had less protection in contrast to Earth. In addition to the factors mentioned above, the size of a planetary body is also a factor in the rate of crater formation due to the influence of the gravity with which it will affect projectiles.

If a planet (or moon) is geologically active or has an atmosphere or hydrosphere, then processes such as volcanism, tectonism, weathering, and erosion can partially or completely erase or degrade craters. The time it takes for a crater to be completely erased from the surface is referred to as the crater retention age and it naturally depends on the original diameter of the crater (Hartmann 1966). Crater degradation may take place on

the surfaces of inactive planetary bodies through the influence of younger impacts and their ejecta, but these processes take place at a much slower rate than geological processes such as regional volcanism or tectonics. Clearly, numerous processes have modified and degraded impact craters on the surface of Mars, hence we can conclude that Mars was either geologically active, or had an atmosphere or hydrosphere, or a combination of these, at some point in the planet's history.

Preserved craters are relatively rare on Earth, because weathering and other geological processes have removed many of them. Currently there are 174 confirmed impact crater structures (Earth Impact Database 2007) and approximately 564 probable and/or possible suspected impact craters (Suspected Earth Impact Sites Database 2007) on Earth. At present, there are more than 42,000 known large crater structures on Mars (Barlow et al. 2003). Due to significantly smaller amounts of atmosphere-surface interaction, the craters on Mars have not eroded as fast as those on Earth. Mars is also much less geologically active at present, and therefore it is intuitive that the crater population on Mars is much larger than that on Earth.

#### *Types of craters*

The formation of different types of impact craters depends on numerous factors, such as the size, velocity, and composition of the impactor as well as the composition of the target material (Melosh 1980; Melosh 1989; Holsapple 1993; Ormö et al. 2002).

The shape of the final crater is directly linked to size and velocity factors. If one increases the size or the speed of a projected object, it is logical to assume that the extent of morphological change (or alteration) is directly proportional to these two factors. The kinetic energy that is released upon impact is responsible for the creation of the crater shape. A simple relationship exists between this energy and the size and velocity of the impactor, and is formulated as follows:  $KE = mv^2$ . The exponential relationship indicates that the velocity of the projectile is much more influential on crater shape than the mere mass of the object.

There are three types of crater morphologies: a) simple craters, b) complex craters, and c) multi-ring basins (Melosh 1989; French 1998). Simple craters are small and bowl-shaped, whereas complex craters are large and flat-floored (see Fig. 1) (French 1998). Complex craters also usually have central peaks that formed during the rebound of the transient crater, while simple craters exhibit no further structural features. Multi-ring basins are large crater structures where the basins can extend for hundreds of kilometers and usually consists of series of concentric rims much like circular mountain ranges (French 1998).

On Mars, simple-to-complex crater transition occurs at diameters of 3-8 km (Pike 1980); where on Earth it is about 4 km for crystalline targets and roughly 2 km for sedimentary targets (French 1998). Craters in this study are mainly complex craters. In this study, most of the complex craters exhibit only a central peak; however, some of the



craters do exhibit peak rings. Most of the complex craters in this study also show signs of structural rim failure in the form of slumped terraces and dislocated blocks of rim material (see Fig. 2).

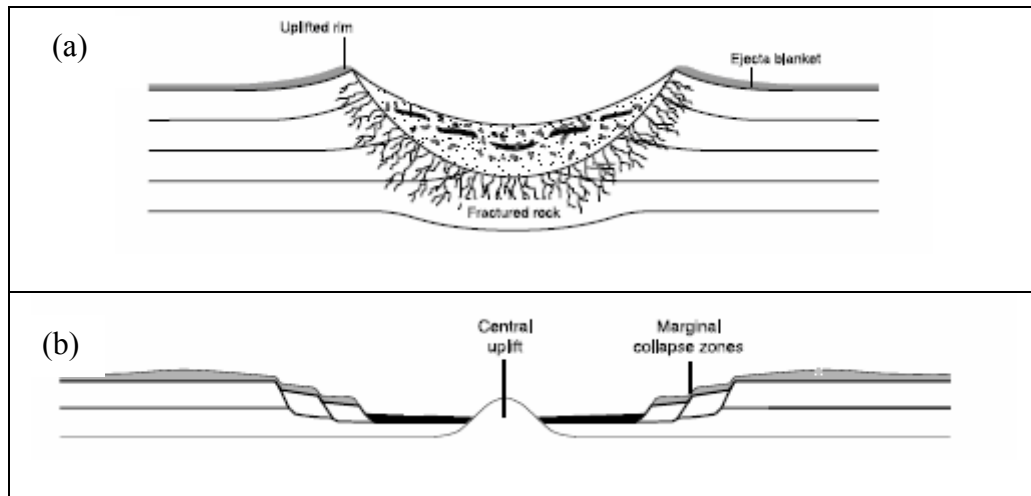


Fig. 1. Morphology of a complex crater (b) differs substantially from that of a simple crater (a). Modified from French (1998).

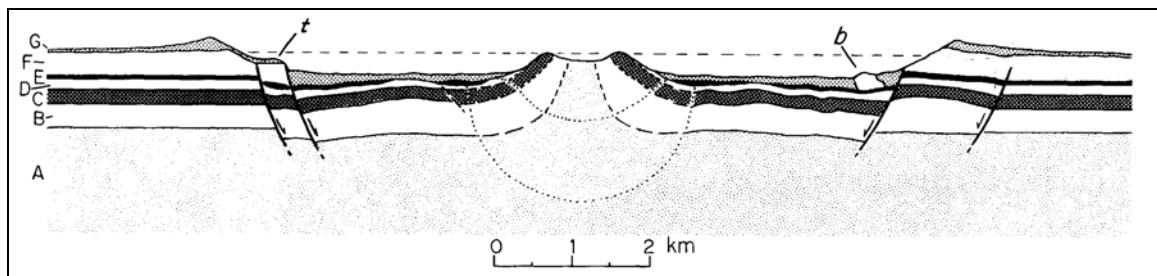


Fig. 2. Different layers present in the target (A-F) as well as the ejecta blanket (G) of a complex crater. Also shown are a terrace (t) and a block of rim material (b) both products of slumping. From Pike (1980).

The composition of the impactor also plays a role in the morphology of the crater, particularly when the composition can be linked to density. Most projectiles are either

comets or asteroids. Both comets and asteroids are small, rocky objects; however, comets also contain significant amounts of volatile ices. Comets are mostly less dense than asteroids, but they are often originally much larger and travel at higher velocities (Melosh 1989).

The influence of the target material composition is a wide and popular field in impact studies and it may even be more important in shape determination than the properties of the projectile (Melosh 1989). For impacts into solid targets such as crystalline bedrock, the crater shape will be uncomplicated and straightforward. For impacts into soft targets, such as unconsolidated sands and water, the crater shape will be much more complicated, and often larger. Impacts on land are often into crystalline bedrock, unless the environment is sedimentary. Impacts in water are more complicated due to the various layers that are present in the target material (Ormö et al. 2002). If the water overlays a region of unconsolidated sediment, which in turn overlays crystalline bedrock, then this tri-layer composition of the target makes the morphology of the resulting crater much more intricate, often resulting in an “inverted sombrero” morphology (Kenkmann 2005; discussed in more detail below).

Beyond the influence of the target composition (further discussed below), other factors that contribute to the morphology of craters include the extent of atmospheric interference, the effects of modification, and the obliqueness of impact. Although these factors are significant, they are of less importance in this specific study. It is assumed

that the craters in this study formed under roughly the same atmospheric conditions and that they have been modified for equivalent amounts of time by similar factors. Oblique impacts are much more common than vertical impacts, yet, most oblique impacts leave approximately concentric crater forms much like vertical impacts do. In the case of marine impacts, a projectile entering the water at an oblique angle would experience more traveling time within the water column than a projectile at a vertical angle, thus lowering the chances of seafloor crater formation (Artemieva and Shuvalov 2002). The crater population in this study is limited to circular impact craters, but no calculations on water column depth were done and thus no conclusions were drawn on the difference in morphology between impacts at vertical and oblique angles.

As mentioned before, the influence of the target material composition is very important. Sub-aerial craters (craters formed on land) usually exhibit an uncomplicated structure; whereas sub-aqueous craters (craters formed in water) usually have more complicated, and often larger, structures (Ormö and Lindström 2000).

Observations of Earth-based marine impacts show that the water column greatly influences the shape, size, and lithology of the resulting crater fill (Ormö et al. 2002; 2004). This gives impacts into marine environments a completely different nature from impacts into dry, sub-aerial targets. Marine-target environments generally exhibit two-fold rheology: a weak, volatile-rich upper layer, and a hard, crystalline lower layer. Owing to the difference in the strength of the two layers, the crater shape that is often

created is that of an inverted sombrero (Kenkmann 2005). This inverted sombrero shape is an outer ring with a large, flat annular trough surrounding a central peak or peak ring, as shown in Fig. 3. Furthermore, the two-fold rheology is also responsible for creating planes on which slump blocks can easily slide down, resulting in a larger crater with a wider annular trough (Collins and Wünneman 2005).

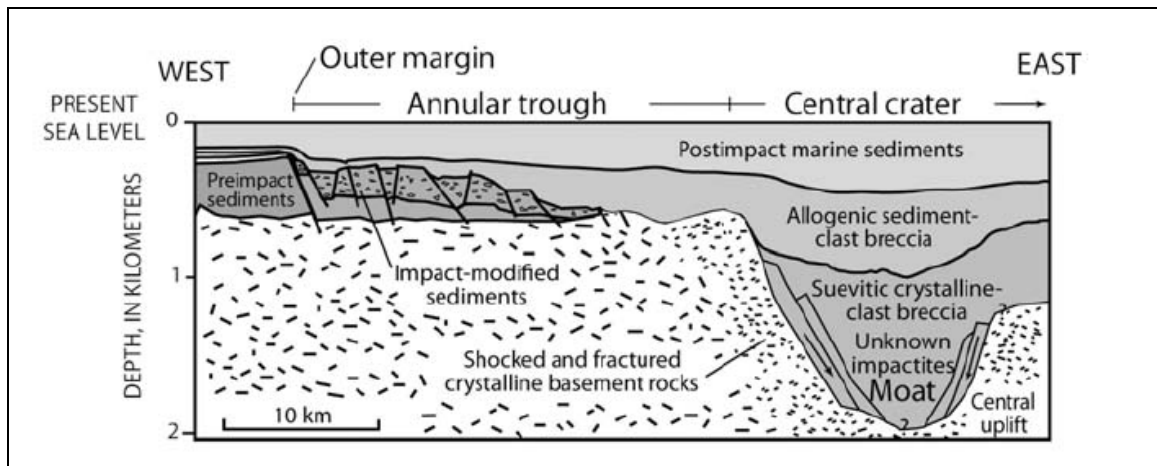


Fig. 3. Cross-section of the inverted sombrero morphology observed at Chesapeake Bay impact crater. The section runs from the western rim to the central peak due east. The wide annular trough and the slumped blocks where the rim collapsed are shown. From Horton et al. (2006).

More than 70% of the Earth's surface is covered by water, and has been for a long time, therefore it is expected that most cosmic impacts on Earth would have occurred at sea. However, only 25 out of 564 suspected impact craters on Earth (roughly 5%) are considered to be marine impact craters (Dypvik and Jansa 2003; Dypvik et al. 2004; Suspected Earth Impact Sites Database 2007). Furthermore, only one of these marine impacts, Eltanin, in the Southern Ocean, occurred in a deep marine setting (Gersonde et al. 1997).

It is important to understand why there are so few marine impact craters on Earth so that we can search in the right areas for marine impact craters on Mars. Some reasons why there are only a few marine impact craters on Earth include a) reduced force of impact; b) plate-tectonics; and c) limited exploration (Artemieva and Shuvalov 2002; Gersonde et al. 2002). These reasons may also be applied to explain why no marine impact craters have been identified on Mars.

Firstly, the strength of the protecting water column weakens the kinetic energy of the impact, and therefore the chance of forming a crater on the ocean floor is smaller. Seafloor craters form only when the impactor interacts with the sub-sea bedrock, so great ocean depths preclude crater formation beyond the water column and it is thus more likely to find distinctively marine crater shapes in shallow water than in deep water. If the ratio ( $h/D$ ) of water depth ( $h$ ) to crater diameter ( $D$ ) is larger than 0.4, there is no formation of a seafloor crater and if the  $h/D$  ratio is larger than 4, there is no formation of any impact-related features (Artemieva and Shuvalov 2002). Projectile size is also a factor to be considered: if the diameter of the projectile is less than the target water-depth, some or all of the crater shape is formed in the water (Ormö et al. 2006). Due to numerous modification processes that take place immediately following the contact and excavation stages of crater formation, the transient crater does not last very long (French 1998). In marine impact craters, this effect is magnified due to the violent return of displaced water that rushes back and re-deposits the sediments (Wünneman and Lange

2002), modifying the crater rim and floor almost instantaneously. Seafloor-craters are therefore rare on Earth, and possibly also on Mars, because of the protection of the surface by the water layer.

Secondly, plate tectonics usually dictates that denser oceanic plates subduct beneath lighter continental plates. Continental plates are therefore typically much older than oceanic plates. This dynamic movement of the lithosphere periodically eradicates crater forms on the ocean floor as the oceanic plate subducts beneath a continental plate. Marine impact craters are therefore not that common on Earth because on a large part of the planet's surface, the evidence of these craters is continuously removed. This might also be the case on Mars where large igneous events resurfaced the planet during its earlier history, removing evidence of impact craters.

Lastly, the ocean floor is relatively unexplored when compared to the continental crust. Not only is it easier for geologists to explore features on land, but it is also easier to observe terrestrial features from satellites in orbit around Earth. Furthermore, craters on the seafloor may not only be buried by water but also by sediments and are therefore harder to recognize than craters on land. Therefore, it is not unexpected to have found evidence of so few marine impacts. Even though Mars does not currently have an ocean that obscures crater forms from satellite imagery, it is true that the vast amounts of satellite imagery is yet to be fully analyzed and explored due to the large volume.

Even though few marine impact craters are identified on Earth, it should be noted that exceptional preservation is required to confirm marine origin. Thus, most confirmed marine impacts are well-preserved examples. When seafloor craters are formed, their post-modification shapes are usually better preserved in aqueous environments than similar craters in dry, land environments. This is true because of rapid sediment burial (Ormö and Lindström 2000). The sediment burial preserves the shape of the crater (Dypvik et al. 2004) similar to a layer of sediments preserving the shape of a fossil skeleton. To study marine impact craters on Mars, it is important to refer back to terrestrial examples. Table 1 lists the locations, diameters, and ages of 17 confirmed marine impact craters on Earth.

Table 1. Marine impact craters on Earth. Modified from Ormö and Lindström (2000) and Dypvik and Jansa (2003).

Crater	Locality	Diameter (km)	Age (Ma)
Avak	Alaska, USA	12	> 95
Chesapeake Bay	Virginia, USA	85	35.5 +/- 0.3
Chixulub	Yucutan, Mexico	~180	64.98 +/- 0.05
Eltanin	South Pacific	?	2 to 15
Gusev	Donets, Russia	3	49.0 +/- 0.2
Granby	Linköping, Sweden	3	470
Kaluga	Kaluga, Russia	15	380 +/- 5
Kamensk	Donets, Russia	25	49.0 +/- 0.2
Kara	Kara Sea, Russia	65	70.3 +/- 0.3
Kärdla	Hiumaa, Estonia	4	455
Karikkoselkä	Läsi-Suomi, Finland	1.3	440 to 445
Lockne	Östersund, Sweden	13.5	> 455
Mjølñir	Barents Sea, Norway	40	142 +/- 2.6
Montagnais	Nova Scotia, Canada	45	50.5 +/- 0.76
Neugrund	Gulf of Finland, Estonia	20	535
Ust Kara	Kara Sea, Russia	25	70.3 +/- 2.2
Wetumpka	Alabama, USA	7.6	81.0 +/- 1.5

## **Objectives**

This study aims to answer the question of evidence of marine impact craters on the surface of Mars. Although it is believed that these structures should exist, and some structures have been identified as potential shallow-marine impact craters (Ormö et al. 2004), as yet there is still no catalogue of potential candidates, and large areas of continental shelf environment lies unexplored.

This project aims to investigate imagery and topographic data collected from the Mars Global Surveyor and Mars Odyssey missions to study the general topography and morphology of impact craters on selected parts of Mars's surface. The main goal is to map and describe impact structures on a part of Mars described by some as a shallow continental shelf area (Parker 1989; Edgett and Parker 1997; Fairén et al. 2003; Ormö et al. 2004). The use of remote-sensing techniques is essential in the detailed study of impact structures on planetary surfaces. Use of different datasets obtained from the Mars Global Surveyor and Mars Odyssey spacecraft allows us to gain insight into the topography and morphology of selected areas on Mars, at higher resolutions than possible with previous datasets such as that of the Viking and Mariner spacecraft. These data are used to identify and rank potential marine impact crater candidates in an area where there is evidence of a historical shallow-marine environment on Mars.

All candidate craters in the study area are rated in an effort to quantify the evidence of marine origin. The criteria for the quantification system are mainly collected



from literature on terrestrial marine impact craters and include characteristics such as evidence of wet mass movement, radial gullies, resurge deposits, central terraces, collapsed rims, and subdued topography. Exemplary candidates are discussed in detail and data (remotely sensed and field-based) from shallow-marine impact structures on Earth are used to compare characteristics of these craters with those of shallow-marine impact craters on Mars (e.g., Von Dalwigk et al. 2001; Dypvik and Jansa 2003; Horton et al. 2006; King et al. 2006; Ormö et al. 2006).

The selected area of study on Mars falls largely within northwestern Arabia Terra (NWAT) with small sections in Acidalia Planitia and Chryse Planitia (Fig. 4). The study area lies roughly right above the equator on the central meridian line and is bounded by the 20° N and 40° N latitude lines as well as the 340° E and 20° E longitude lines. Arabia Terra is a large, flat region straddling the distinct geologic boundary, commonly referred to as the crustal dichotomy, which roughly separates the northern and southern hemispheres. The average elevation of the study area is around 1-2 km below mean surface level. Assuming that a large sea once covered the northern lowlands early in its history (Parker 1989; Edgett and Parker 1997; Fairén et al. 2003), water would have covered all areas north of the dichotomy, thus creating a shallow-water, continental shelf environment of varying width all along the dichotomy. On Earth, a continental shelf is an ideal setting for the preservation of shallow-marine impact craters in the seafloor since a seafloor crater is expected to form and rapid sedimentation should keep further erosional processes from destroying it. Similarly, NWAT, which arguably was once part

of a continental shelf, makes a suitable study area for shallow-marine impact craters.

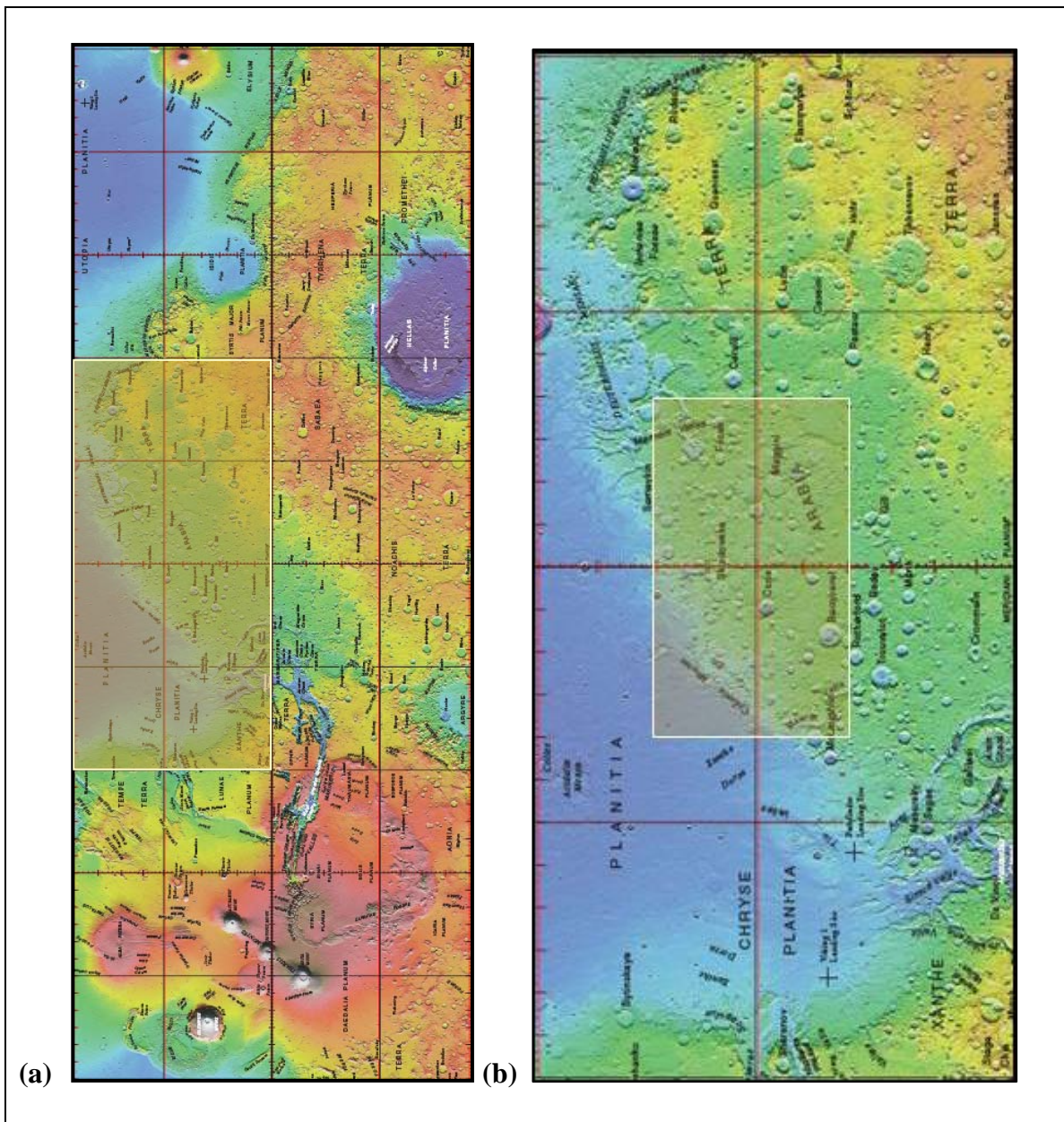


Fig. 4. Mars topographic map as viewed from the equator and central meridian (a). Elevation increases from blue to red. The study area lies mainly within Arabia Terra, (shown in b). Modified from MOLA Topographic Map, GIS I-2782, USGS.

Based on cratering chronology, the geological evolution of Mars is divided into three epochs: Noachian (N), Hesperian (H), and Amazonian (A) (see Table 2).

Table 2. Geological time-scale for Mars based on cratering chronology. Modified from Hartmann and Neukum (2001).

Age	Epoch	Characteristics
2.9 Ga – date	Amazonian	Little geological activity
3.7 Ga – 2.9 Ga	Hesperian	Intense volcanic activity
4.5 Ga – 3.7 Ga	Noachian	Heavy cratering

The study area is largely Noachian in age. Some small parts of the study area are of Hesperian and Amazonian age, but these are less than 20% of the total surface exposure. The study area includes two major geological units, Noachis Terra of Noachian age (shown in orange) and Vastitas Borealis of Amazonian age (shown in green) (see Fig. 5).

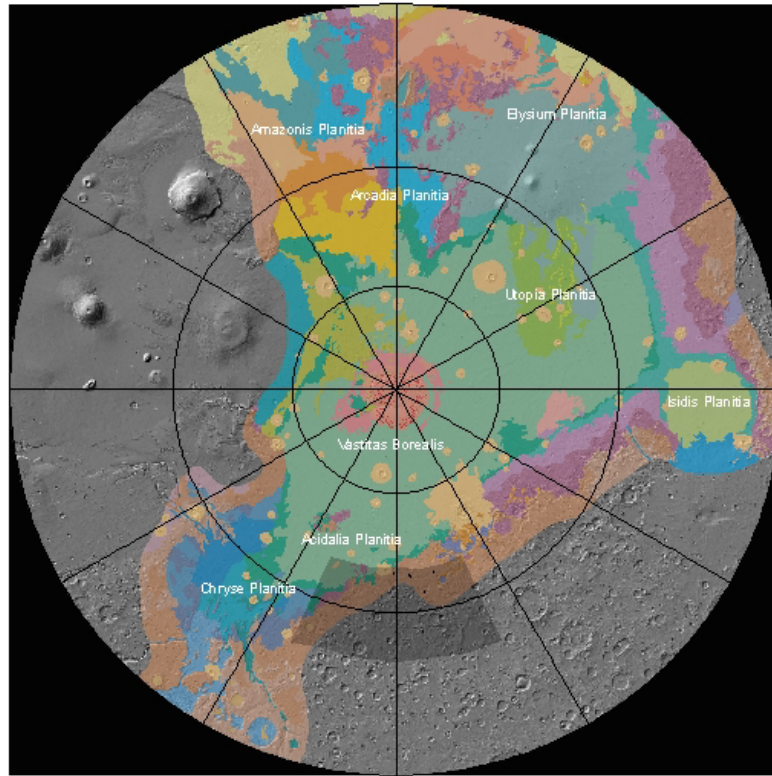


Fig. 5. Regional geological map of the northern plains of Mars, as viewed from the North Pole. Modified from Tanaka et al. (2005).

This study focuses on craters within a size range of 10 to 100 kilometers in diameter. The spatial resolution of the topographic data determined the lower limit, whereas convenience is mainly responsible for the upper limit. However, it should be noted that most of the Earth analogues for shallow-marine impact craters, fall within this range (refer back to Table 1).

## **Significance**

In unison with Goal 3, Sub-goal 3-C of NASA's Strategic Plan (NASA 2006), this project seeks to contribute to the scientific knowledge about the origin and history of the solar system by investigating the environmental history of Mars. The existence and extent of oceans on the surface of Mars is a highly debated question that is yet to be answered. Evidence of shallow-marine impact craters on Mars will aid in understanding the morphological evolution of the planet and its former oceans, and could potentially support the theory of the occurrence of one or more large oceans on the surface of Mars during its early history. Research on shallow-marine impact craters on Mars is still in an early stage and a catalog of potential shallow-marine impact craters is a useful addition to the Martian crater catalogs that are already available. The results of this type of study are useful in helping develop a general classification and characterization of potential marine craters.

## **LITERATURE REVIEW**

To give a proper overview of the published literature in the field of shallow-marine impact craters, this chapter is subdivided into several sections, the first of which is a brief discussion on the evidence for water on Mars. A second section follows, more focused on the arguments for the existence of an ocean(s) on Mars. The third section explores the different physical properties of shallow-marine craters and focuses specifically on the characteristics for shallow-marine impact craters, and the fourth section discusses some examples of shallow-marine impact craters on Earth. Lastly, a short background of remote sensing is given, and the methods employed in this study are introduced.

## **Water on Mars**

Water has played, and is still playing, a large role in Mars' geological evolution. Until recently, proving the presence of water on Mars has been an elusive task, regardless of the fact that numerous scientists have expected it for decades. Remote sensing combined with ground-based rover observations and laboratory-based Martian meteorite analysis make it possible to support the presence of water and to analyze the influence it has had on the geology of this planet (Squyres 1989; Baker 2001).

At present, Mars has surficial and near-surface water (Solomon et al. 2005; McSween 2006). Water in a liquid form is not stable on the surface due to low temperatures and pressures, but occurs frozen at the poles and below the surface. According to Solomon et al. (2005), there is evidence for interaction of liquid water with the Martian surface particularly during the Noachian epoch. The Noachian is the period during which heavy bombardment took place on the surface of the planet. It is during this period that Mars is thought to have been warm and wet. Heavy resurfacing due to volcanic activity characterized the Hesperian, and the Amazonian is generally believed to have been geologically inactive.

McSween (2006) lists the following three observations as indicators of water on the surface: a) the geomorphology (Baker 2006); b) the presence of altered as well as evaporite minerals; c) and the composition of Martian meteorites. Geomorphology is remotely studied by means of high-resolution visual imagery of the surface, and more

recently, also by shallow, ground penetrating radar. The surface mineral deposits are also remotely studied, mainly through spectrometers on both rovers and orbital spacecraft. Martian meteorites are the only true samples we have from this planet, and are thus the only objects that can be analyzed in the laboratory.

Geomorphologic indicators of water include channels, valleys, alluvial fans, and sediments (Solomon et al. 2005; Baker 2006). Even though scientists have observed such structures on Mars's surface for decades, it is only recently that imagery became advanced enough to show the details of these water-related features. Some of the recent images show small gullies running through crater rims, and these have been interpreted as evidence for recent melting of near-surface ground ice, also referred to as seepage (Malin and Edgett 2000; Solomon et al. 2005; Baker 2006). Further evidence of subsurface ice can be found in the presence of a) grooved textures on channel and crater walls, b) unusual crater ejecta shapes caused by fluidization of ice, and c) glacial landforms (Christensen 2006). Indicators of flowing water are found throughout the surface of the planet, but valleys and channels are more prevalent in the mid-latitude regions. This distribution indicates that water might have once flowed from the higher southern latitudes to the lower northern latitudes, forming an ocean in the northern plains.

In addition to an abundance of igneous minerals, the Martian surface shows evidence of chemically altered minerals as well as evaporitic sedimentary deposits (Wyatt and McSween 2006). The robotic Mars Exploration Rovers (MERs) have



discovered much about the nature of the surface of the planet. Spirit rover landed on 4 January 2004 in Gusev crater and found drenched, altered volcanic ash at nearby Columbia Hills. Opportunity rover landed on 25 January 2004 in Eagle crater and found rippled evaporite sediments in the area. The discovery of sulfate minerals indicates that the basaltic crust may have been intensely weathered by water, and the presence of hematite supports the theory that water once flowed across the surface at Meridiani Planum (Squyres et al. 2004). Besides the mineralogy, the cross-stratification observed in rock outcrops implies that the area was affected by transport of sediment, either under aqueous or aerial conditions. According to Squyres et al. (2004; 2006a; 2006b), the size (wavelengths of a few centimeters) and the geometry of these ripples, suggest the former. The trough cross-bedding found in Eagle crater as well as in Endurance and Erebus craters nearby, displays festoon or concave-upward geometry that on Earth is seen only in aqueous environments (Herkenhoff et al. 2004; Squyres et al. 2006a; 2006b).

Further support for a warmer and wetter Mars in the past is provided by the results of the spectrometers onboard the Mars Odyssey and Mars Express spacecraft. THEMIS, a thermal emission spectrograph onboard Mars Odyssey, found evidence of hematite at Meridiani Terra long before the Opportunity rover did. More recently, OMEGA, a reflectance spectrometer onboard Mars Express, found evidence of multiple ancient sedimentary deposits that formed in an aqueous environment (Paige 2005). Reflectance spectrometers can gather data from fine-grained deposits that would normally give a very weak emission signal, which is why this instrument has identified

more aqueous sedimentary deposits than THEMIS or other thermal spectrometers.

Of the more than 24,000 meteorites found to date, only 36 are known to be Martian in origin (Leshin and Vicenzi 2006). Three classes of Martian meteorites exist (shergottites, nakhlites, and chassignites, which are known collectively as SNCs) based on mineralogical similarities to type meteorites that fell in India, Egypt, and France, respectively (Lodders 1998). Martian meteorites have isotope ratios that are all very similar to one another, yet vary greatly from isotope ratios of asteroids, comets, and terrestrial rocks. Even though the SNC meteorites are igneous in origin, they contain traces of water-precipitated minerals such as carbonates and sulfates (Gooding 1992; Leshin and Vicenzi 2006). Furthermore, Gooding (1992) concluded that the SNC secondary mineral precipitated from saline liquid water. These aqueous precipitates indicate that water was present on Mars at least at the time that the meteorites formed, and maybe even beyond that.

The evidence for water on Mars is unequivocal. Aqueous activity was, and maybe still is, common on Mars. The question is no longer if water was present on the surface, but how much and for how long (Baker 2001; Malin and Edgett 2003).

## **Oceans on Mars**

Oceans on Mars have been proposed by several authors (Parker et al. 1989; Edgett and Parker 1997; Fairén et al. 2003) and two main oceans have been suggested; one large ocean of Noachian age (at least ~4 Ga; Clifford and Parker 2001) and a smaller Hesperian ocean (of ~2-3 Ga; Clifford and Parker 2001). Since then, a few smaller seas and lakes have also been proposed, but these are much younger and smaller and therefore do not play a large role in this study.

### *Large Noachian ocean and smaller Hesperian ocean*

Using Viking data, Parker et al. (1989) interpreted the dichotomy as the remnant of a shoreline of an ocean or lake. In fact, Parker et al. (1989) delineated two potential shorelines, and called them Contact 1 and Contact 2 (see Fig. 6). Contact 1 lies nearly along the boundary between the upland and lowland surfaces on Mars, which falls along the crustal dichotomy. Contact 1 encloses the northern lowlands, runs through Arabia Terra and exhibits two types of boundaries; a gradational, transitional boundary and a sharper, fretted boundary (Parker 1989). Contact 2 lies between Contact 1 and the rest of the northern plains, in other words, it encloses a slightly smaller part of the northern lowlands. Both of these contacts are drawn in Fig. 6. Based on the relationship between these two shorelines, it seems that the ocean contained by Contact 1 was not only much larger and expansive than the ocean contained by Contact 2, but also much older and thus its shoreline is less well preserved.

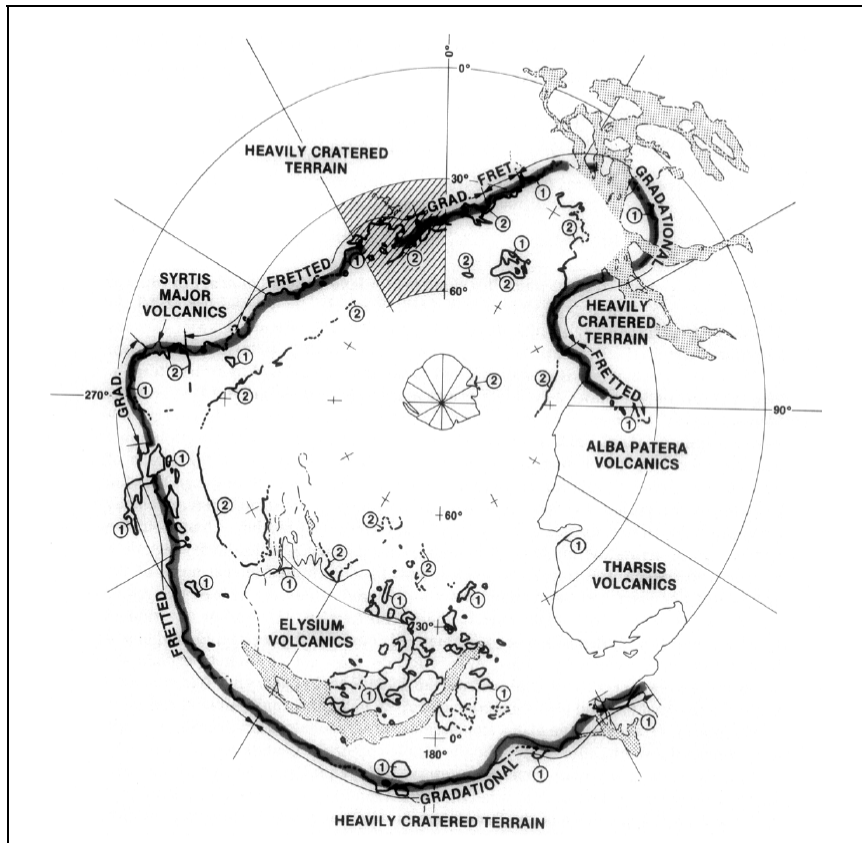


Fig. 6. Locations of shorelines proposed by Parker et al. (1989) as viewed from the North Pole. A thick black line indicates Contact 1, whereas Contact 2 is the thinner grey line. The Ismenius Lacus quadrangle, which forms the upper left hand corner of the study area, is shaded. From Parker et al. (1989).

Edgett and Parker (1997) proposed the existence of a large ocean in the vicinity of Arabia Terra during Mars' early history based on three factors: a) the existence of an interpreted shore-like contact between the southern highlands and the northern lowlands; b) the occurrence of polygonal evaporite structures; and c) the presence of sand deposits. The difference in elevation and roughness around the crustal dichotomy can easily be interpreted as evidence for an ancient shoreline. Thus, the potential of the dichotomy to represent a shoreline is by now fairly accepted. Large (3-8 km across) polygonal structures in Sinus Meridiani (just south of Arabia Terra) could indicate that water was

present on the surface here and that the water has since evaporated (Edgett and Parker 1997). Layered sand deposits are found in and around craters in Arabia Terra. The sand deposits do not drape over the topography the way eolian features are expected to do, but rather seem to lap up against ridges and crater rims as if emplaced by lacustrine processes. These findings are in accord with the proposed Noachian shoreline that runs through Arabia Terra, also referred to as Contact 1.

Furthermore, Edgett and Parker (1997) also mention that large valley networks in Arabia Terra are almost entirely absent, and suggest that this is because Arabia Terra was under water at the time the valley networks formed. The formation of the major valley networks on Mars have been dated as Noachian (Carr 1995; Hynek and Phillips 2003), which corresponds with the Noachian shoreline proposed by others (Parker 1989; Fairén et al. 2003).

More recently, the existence of a northern ocean or *Oceanus Borealis*, within the shorelines suggested by Parker (1989) was suggested because the dichotomy not only resembles a shoreline, but the outflow channels and valley networks terminate at the boundary much like rivers terminate in deltas; the low density of craters in the northern plains is due to the water cover of a large sea; and the spectrographic signatures of carbonates and sulfates indicate evaporite deposits (Fairén et al. 2003). Some of these arguments have been stated before, for example, Helfer (1990), argued that oceans in the northern plains are to be expected based on the low crater density observed in this region.

Smith et al. (2001) stated that MOLA data, for regions with large channels, support sustained flow and multiple flooding events as well as potential existence of an early ocean. Most importantly, Fairén et al. (2003) highlighted the existence of another shoreline suggested by Clifford and Parker (2001). Clifford and Parker suggested that the Noachian shoreline, Contact 1, may have a slightly different location than first proposed. The location of Contact 1 has been modified to accommodate for the large elevation differences across the boundary, to include more of the valley networks that end abruptly south of Arabia Terra, and to coincide with the crustal thickness dichotomy (Fairén et al. 2003). Contact 1 is also referred to as the Arabia shoreline, and Contact 2 as the Deuteronilus shoreline (Clifford and Parker 2001). Both these shorelines, as well as the Meridiani shoreline, which later formed part of Fairén et al.'s (2003) Shoreline 1, are shown in Fig. 7.

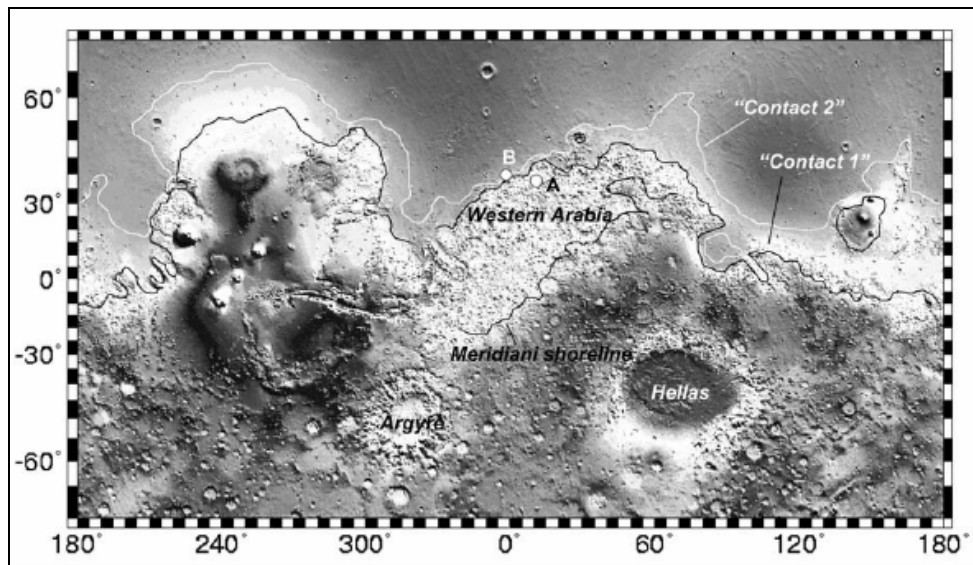


Fig. 7. Locations of two mapped shorelines, here labeled Contact 1 and Contact 2, as viewed from the equator in an equidistant cylindrical projection of the surface. Meridiani shoreline (as proposed by Clifford and Parker, 2001) is also shown. From Ormö et al. (2004).

The three shorelines discussed by Fairén et al. (2003) are drawn from a north polar perspective in Fig. 8. One can see from this figure that the original ocean, encompassed by either the Meridiani or Arabia shorelines, was much more extensive than the more recent ocean encompassed by the Deuteronilus shoreline.

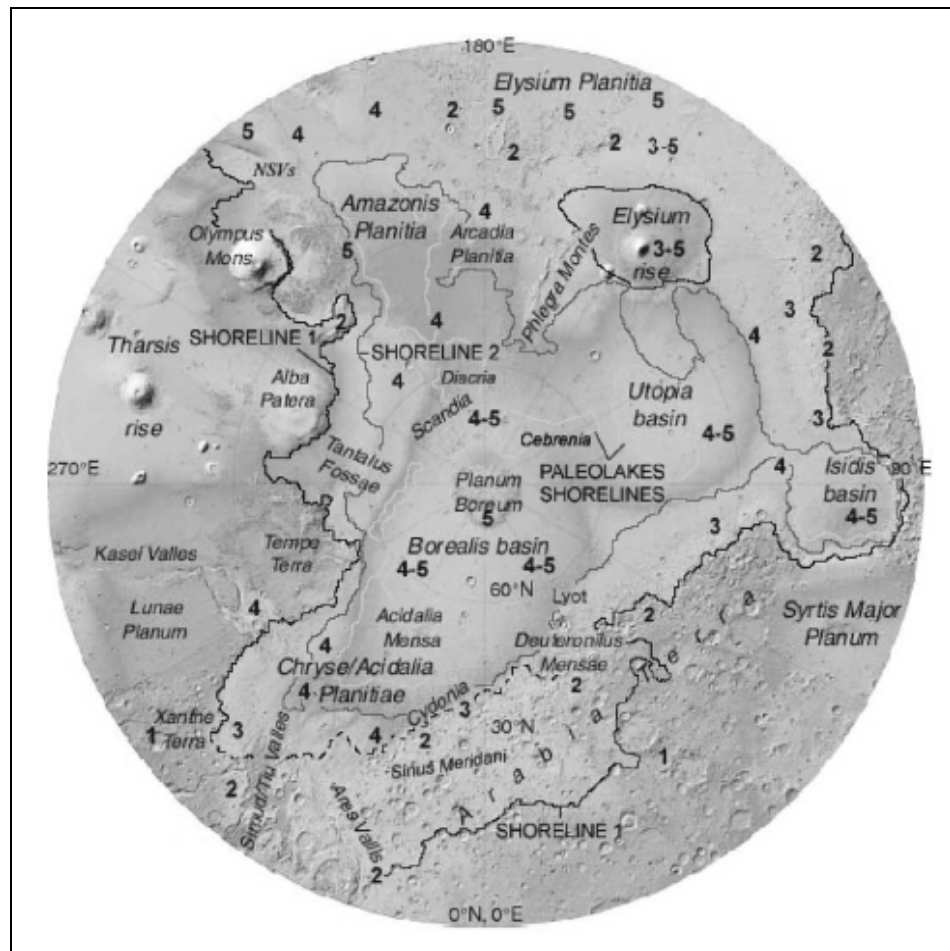


Fig. 8. Locations of shorelines proposed by Fairén et al. (2003) as viewed from the North Pole. Contact 1 (now referred to as Shoreline 1) is indicated by a solid black line, whereas Contact 2 (now referred to as Shoreline 2) is the thinner grey line. The dashed line north of Arabia Terra is the original location of Contact 1, but has since been modified to run further south (see discussion). From Fairén et al. (2003).

Thick sedimentary layers cover Arabia Terra as well as most of the northern lowlands. Sedimentary deposits could indicate that a large ocean once existed in the northern hemisphere (Edgett and Parker 1997; Edgett and Malin 2002; Venechuk et al. 2005; Baker 2006). The main ~100 m thick sedimentary layer is commonly referred to as the Vastitas Borealis Formation (VBF) and is found across the smooth northern plains (Smith et al. 1998; Carr and Head 2003). Numerous origins for this sedimentary layer have been suggested, including paleopolar, volcanoclastic, eolian, and sub-aqueous sedimentary, however, Mars Orbiter Camera (MOC) images have not clearly identified one of these theories as the true origin (Edgett and Malin 2002). Boyce et al. (2005) made a study of the depth-diameter ratios of a large population of impact craters in the northern lowlands and showed that the VBF is draped over most of the lowlands giving it a smooth appearance. The VBF could only have formed as sub-aqueous sedimentation beneath a large body of water, thus, it is highly likely that an ocean with an average depth of ~430 m could have once existed in the northern lowlands (Boyce et al. 2005). Based on their conclusions, an ocean existed in the northern lowlands during Late Hesperian (approximately 3,5 to 1,8 Ga ago). This would correspond with the second, smaller, and younger ocean, and shoreline Contact 2.

Mars Orbiter Laser Altimeter (MOLA) data further provide evidence for an ocean on Mars (Head et al. 1999; Ivanov and Head 2001). According to Head et al. (1999), the current high-resolution altimetry data of the northern lowlands of Mars affirm the hypothesis that elevations around Contact 2 are close to an equipotential line and that it



indicates the level shoreline of a large standing body of water somewhere during the Hesperian epoch. In addition, Head and Ivanov (2001) also found that the Hesperian-age outflow channels all enter the northern plains at similar elevations and that the morphology of these channels change rapidly from sub-aerial to sub-marine at the base level.

If water filled the northern lowlands up to the Meridiani shoreline, the equivalent global depth would be 1510 m (Carr and Head 2003). Similarly, if water filled the lowlands up to the Arabia shoreline, the global depth would be 599 m and for the Deuteronilus shoreline, it would be 130 m (Carr and Head 2003). The average height of the Arabia shoreline is -1680 m, which would yield an ocean with maximum depth of 3570 m over the North Polar basin (Head et al. 2003). Similarly, the average height of the Deuteronilus shoreline is -3760 m, which would yield an ocean with maximum depth of 1490 m over the North Polar Basin (see Fig. 9) (Head et al. 2003).

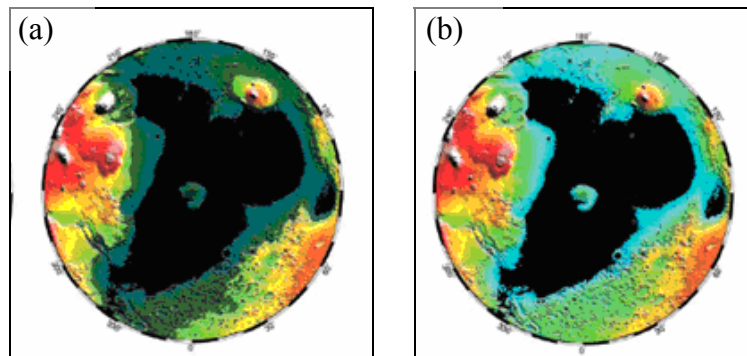


Fig. 9. Flooding of the northern lowlands (a) up to a maximum depth of 1490 m (filled to level of Contact 2); and (b) up to a maximum depth of 3570 m (filled to level of Contact 1) (Head et al. 2003).

### *Smaller local lakes*

As discussed in the previous section on water on Mars, the results from the Mars Exploration Rover (MER) explorations indicate that Meridiani Planum has been periodically flooded (Squyres et al. 2004). However, the timing of these flooding episodes is hard to assess. According to Squyres et al. (2004), cratering rates suggest that the rocks in this area could be of Noachian age, or at least a few billion years old. However, it seems more likely that these small, localized seas were of Amazonian age. Since Meridiani Planum was likely once a large, shallow playa lake, it is easy to deduce that there may have been numerous small seas on Mars' surface during its history.

### *Evidence for oceans on Mars*

Since the shorelines of three different large water masses have been proposed, numerous critical evaluations of these shorelines have been done. Malin and Edgett (1999), as well as Carr and Head (2003), evaluated relations along the crustal dichotomy on Mars with the use of high-resolution imagery from Mars Orbiter Camera (MOC) and Thermal Emission Imaging System (THEMIS). The morphologic evidence for a large standing body of water is equivocal in some places, and no visual evidence was found for a shoreline along the crustal dichotomy (Malin and Edgett 1999; Carr and Head 2003; Chapman 2003; Ghatan and Zimbleman 2006). Most recently, Ghatan and Zimbleman (2006) studied 735 MOC and 447 THEMIS images and found only four images with potential candidates for coastal ridges such as spits and barrier islands. Ghatan and Zimbleman (2006) reason that either a) there was no northern ocean, b) factors such as

low wave energy and low sediment input were responsible for no formation of ridges, or c) large amounts of erosion caused destruction of ridges. Malin and Edgett (1999) mention that it may be hard to find evidence of coastlines from remotely sensed data alone and that even coastlines on Earth are hard to discern from orbital or airborne data. In addition, even though orbital cameras photograph the surface intensely, there may still not be enough data for producing conclusions. It may even be that coastal features that are common on Earth, are not well developed on Mars (Chapman 2003), and therefore we cannot assume that no evidence of coastal features mean there was no coast.

Additionally, there are significant variations in elevation along the Noachian shoreline, Contact 1. Sea level, by definition, should be more or less level; therefore, changes in elevation do not support the existence of a sea level. Contact 1 was first defined by Parker (1989) with a difference in elevation in places was as much as 11 km. The modified Contact 1, or Shoreline 1 (Fairén et al. 2003), decreases this elevation difference to approximately 3 km.

Until recently, the difference in elevation was large enough to cast doubt on an ancient, Noachian ocean encompassed by the Arabia shoreline. However, Perron et al. (2007) suggested a global mechanism - polar wander - for altering elevations along the dichotomy while retaining its original shape. Polar wander is the wobbling of a planet's axis and it is responsible for many climatic variations. Schultz and Lutz (1988) suggested that polar wander has played a role in Mars's geological history, but not until

Perron et al. (2007) modeled true polar wander in their recent study, did it become apparent how influential this wandering has been in shaping the surface of Mars.

Polar motion changes a planet's geographic surfaces, including the sea level (Perron et al. 2007). For each shoreline, there is a paleopole that, when altered, will deform the shape of the shoreline accordingly. Perron et al. (2007) shows that the deformation associated with true polar wander can account for the trends of variation in the shoreline elevations. True polar wander on Mars may have been induced by the formation of the massive volcanic province, Tharsis (Zuber, 2007).

Perron et al.'s (2003) analysis removes the main argument against oceans on Mars. Because it seems that oceans existed on Mars for at least some time in the Martian history, the surface should display numerous crater forms that fit the Earth-based description of a shallow-marine impact. The Martian surface could have up to 1,400 marine impact craters, based on the length of time that oceans existed on the planet and the size of the possible ocean(s) (Ormö et al. 2004). Their study was based on the minimum and maximum ages of duration for two large bodies of water in the northern lowlands, in combination with the cratering rates for the planet during those times. Thus, some previously submerged regions on the surface of Mars are potentially excellent areas of study for shallow-marine impact craters.

## **Physical properties and characteristics of shallow-marine impact craters**

In order to discuss the physical properties and characteristics of shallow-marine impact craters, a brief discussion on the stages of formation of marine target craters is necessary. The three main stages (contact/compression, excavation, modification) of crater formation are the same for both terrestrial and marine craters (Melosh 1989); however, the details of these stages differ slightly. In the contact/compression stage, the projectile enters the water column, subsequently the unconsolidated sediment layers, and finally the crystalline basement. During the excavation stage, a transient crater is formed, often largely within the water column. Lastly, during the modification stage, numerous physical changes occur within the crater, many related to water resurge, and some of these processes continue until the crater is completely erased from the surface. Fig. 10 illustrates these different stages and shows the expected inverted sombrero morphology.

According to Artemieva and Shuvalov (2002), when a projectile enters a water target there are numerous events that occur in the water column and on the seafloor. The main events are listed in Table 3 below. These events, couple with the stages of formation, are used to formulate a list of characteristics that are expected to be present in shallow-marine craters.

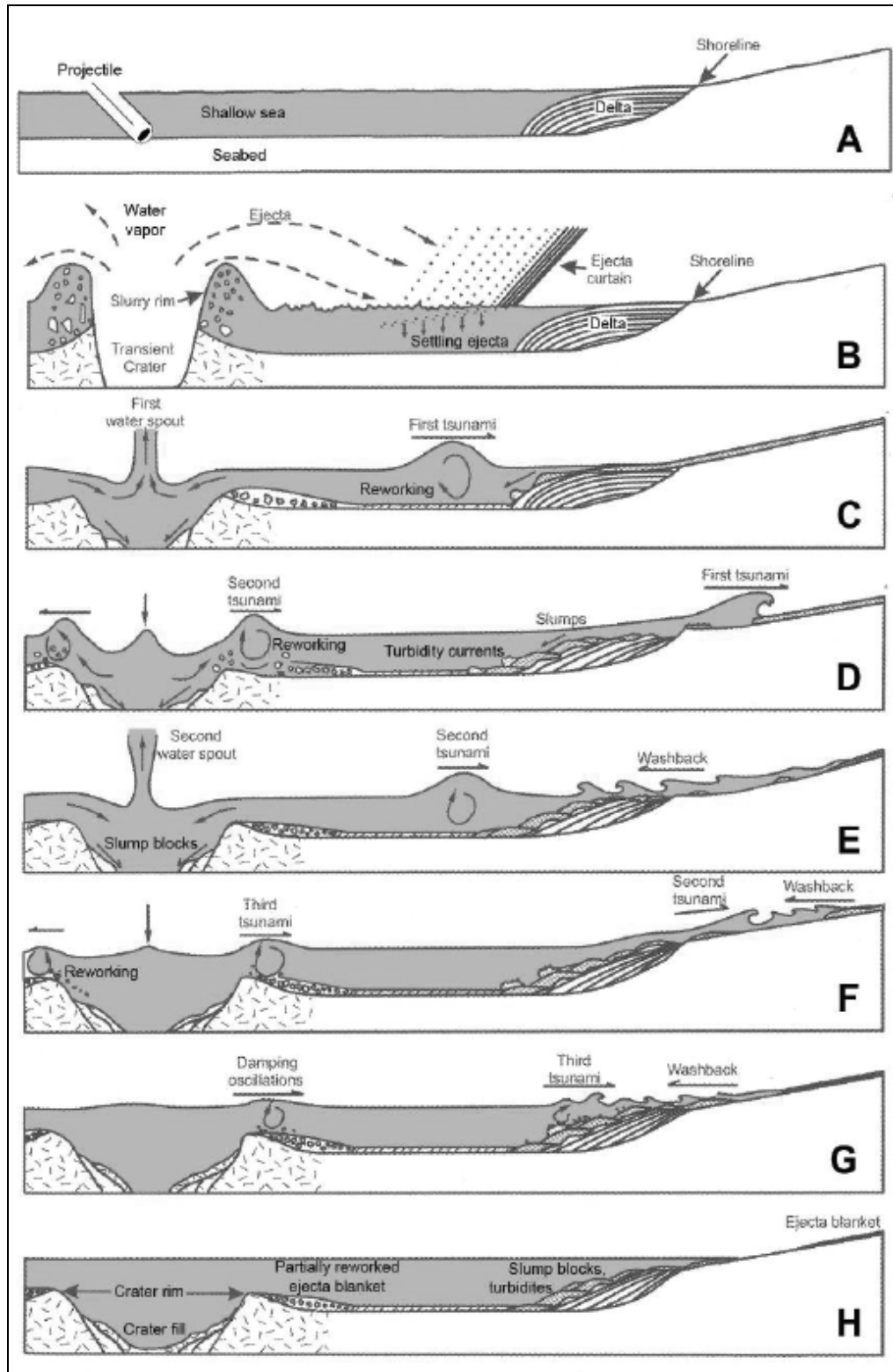


Fig. 10. Stages (A-H) of formation, excavation, and modification for marine impact craters. Note the inverted sombrero morphology of the crater. From Johnson (2007).

Table 3. Main events associated with impacts into aqueous targets (adapted from Artemieva and Shuvalov 2002).

Event	Effects	Time
Contact Stage	Strong shock-wave	<1 second
Excavation Flow	Surge formation Possible craterform	1-10 seconds
Crater Collapse	Tsunamis Craterform modification Impact debris fall-back	Minutes to hours

Several physical parameters are used to describe impact craters such as the depth to diameter ratios, the slope of the crater rim, and the shape and extent of the ejecta deposits. Furthermore, several indicative characteristics can be associated with shallow-marine impact craters on Earth, and these include features indicative of wet mass movement (Dypvik et al. 2004), radial gullies (Von Dalwigk and Ormö 2001), resurge deposits, central terraces, collapsed rims, and subdued topography. These features, if present, could be visible on images and could therefore potentially be used as key characteristics in the identification of Martian shallow-marine impact craters. Ormö et al. (2004) recognized some possible shallow-marine craters with the use of low-resolution Viking imagery based on expected morphological characteristics. All these parameters are discussed in more detail below.

### *Depth-diameter ratios*

Rim diameter and crater depth are two of the most important morphologic elements of an impact crater, both on Earth as well as Mars (Smith et al. 2001; Boyce et al. 2005). The ratio between depth and diameter is often a reliable indicator of the type of crater (i.e., the environment in which it was formed) and the extent of crater modification (Garvin et al. 2000; Aharonson et al. 2001; Boyce et al. 2005). Diameter may not change much during crater modification and can be used as a good estimate of original crater size, but in contrast, surface processes significantly influence crater depth over time (Boyce et al. 2005). Fig. 11 shows the two depths that can be measured; one from the rim to the center of the crater ( $d_r$ ), and one from the average surrounding topography to the center of the crater ( $d_s$ ). The difference between these two depths ( $d_r$  and  $d_s$ ) is the rim height, which is commonly about 4% or less of the crater diameter (Ormö and Lindström 2000).

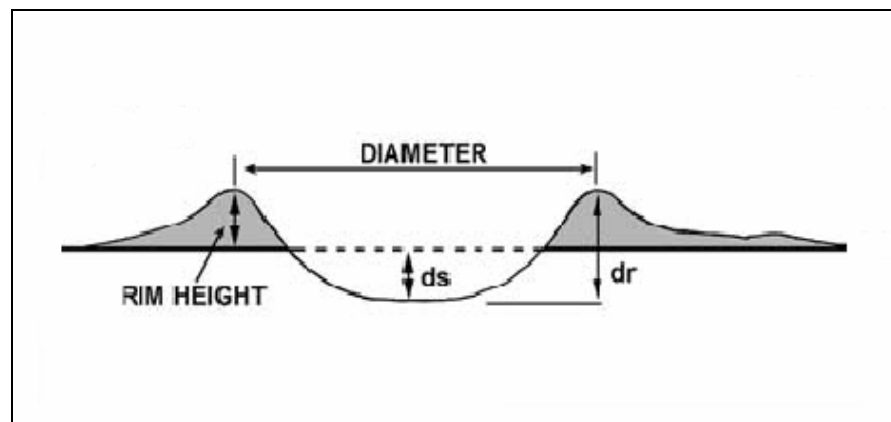


Fig. 11. Parameters in depth-diameter calculations include rim-rim diameter and rim height. Also shown here are  $d_s$  (depth of crater compared to surrounding topography) and  $d_r$  (depth of crater from rim). From Boyce et al. (2005).



Common depth-diameter ratios for simple, terrestrial craters range from one third to one fifth, depending on the nature of the target material (Ormö and Lindström 2000). More particularly,  $d = 0.29D^{0.93}$  for simple terrestrial craters, and  $d = 0.15D^{0.43}$  for complex terrestrial craters (Grieve 1987) where  $d$  is the depth of the crater from the rim, and  $D$  is the rim-to-rim diameter, both in kilometers. Notice that complex craters are shallower than simple craters.

Studies of depth-diameter ratios for lunar impact craters (diameters <250 km) have been done by Pike (1977) who found the relationship to be  $d = 0.23D^{0.94}$  for small craters and  $d = 0.75D^{0.30}$  for larger craters. Howenstein (2006), made a study of the depth-diameter ratios for large Martian craters (diameters of 20 to 2000 km), and found the overall depth-diameter ratio to be  $d = 0.61D^{0.33}$ . Garvin et al. (2000) found depth-diameter relationships for polar and non-polar craters to be  $d = 0.03D^{1.04}$  and  $d = 0.19D^{0.55}$  respectively. For fresh, complex craters on Mars, this relationship has been defined as  $d = 0.33D^{0.53}$  (Smith et al. 2001). More specifically, craters in Arabia Terra have a  $d/D$  ratio ranging from 0.07 to 0.09 (Barlow 1993). Depth-diameter ratios for Martian craters seem to decrease with an increase in latitude due to an increase in sub-surface volatiles and ices (Barlow 1993).

Modeling experiments suggest that marine craters should be wider than craters formed on land under similar conditions (Gault and Sonnett 1982). According to Dypvik and Jansa (2003), marine craters are characterized by larger diameters because of radial

enlargement. Some processes have been suggested to be responsible for the widening of the crater, of which the most common are rim failure due to resurge or erosion by water currents or due to sediment instability. Boyce et al. (2005) concluded that the low depth-diameter ratios suggest infilling by sedimentary deposits, thus supporting the theory of a large ocean depositing what has been described as the Vastitas Borealis Formation (VBF).

### *Slopes*

The slopes of crater rims are indicative of the style and duration of the subsequent modification processes (Garvin et al. 2000; Aharonson et al. 2001). Crater slopes can be modified during impact by resurge activity (Ormö and Lindström 2000) or after impact by thermal creep, a process wherein the difference in temperatures cause particles to slide down a slope (Sharp 1968).


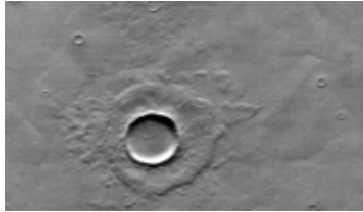

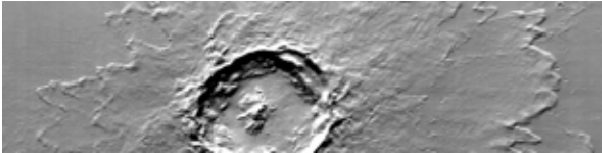

Kreslavsky and Head (2006) used MOLA data to measure the steepness of crater slopes in the northern plains and found that some craters are very shallow. Shallow craters could indicate that sediment infilling has taken place. The steepest crater wall slopes in the population studied by Kreslavsky and Head (2006) are at angles of 30°, but the majority of the 130 craters that were studied have more gently sloping crater walls. This is in line with observations of marine craters on Earth because modification processes in unconsolidated sediments often yield larger, more subdued craters.

### *Ejecta deposits*

Further distinctive attributes of shallow-marine impact craters include the extent, shape and thickness of the ejecta deposits that are blown out of the crater upon impact, as well as the volume of the crater depression. Studies have shown that crater and ejecta morphology depend greatly on sediment strength, which is directly linked to water content (Wohletz and Sheridan 1983). The presence of water in the target material leads to the formation of water vapor, which in turn accelerates and increases the formation of an ejecta layer, resulting in wider ejecta blankets for marine target craters than for land target craters (Melosh 1989; Dypvik 2004; Schaefer et al. 2006). Schaefer et al. (2006) modeled impacts into wet and dry sandstone and found that ejecta velocities from the wet sandstone were up to 50% higher than for the dry sandstone.

Barlow (2006a) classified ejecta morphologies based on appearance in her Catalog of Large Martian Impact Craters. Table 4 lists the different morphologies and some examples of each. The ejecta morphologies important in this study are the rampart craters. Rampart craters are fluidized craters with lobate ejecta morphologies (Wohletz and Sheridan 1983) and form as a result of impacts into volatile rich environments or fluid-rich substrates containing water or ice, usually the latter (Mouginis-Mark 1987).

Table 4. Classification of ejecta morphology according to Barlow's Catalog of Large Martian Impact Craters and examples from THEMIS images (Barlow 2006a).

Name	Description	Example Image
SL	Single lobe rampart	
DL	Double lobe rampart	
ML	Multiple lobe rampart	
Di	Diverse morphology	
Pn	Pancake ejecta	

### *Wet Mass Movement (WMM)*

Mass movement can occur at various rates, but most important in this study is the rapid movement of unconsolidated sediment. Two types of mass movement are particularly important: slides, where the movement occurs in a well-defined plane; and flows, where the movement is more fluid in behavior (see Fig. 12). A slump is a type of slide where material moves downward as a parcel or unit, often with a backward rotation on a curved displacement surface (Kennett 1982). Listric or normal faults form as the result of this displacement. A debris flow is a type of flow where particles chaotically move downslope in a saturated sediment slurry while supported by cohesion strength (Kennett 1982).

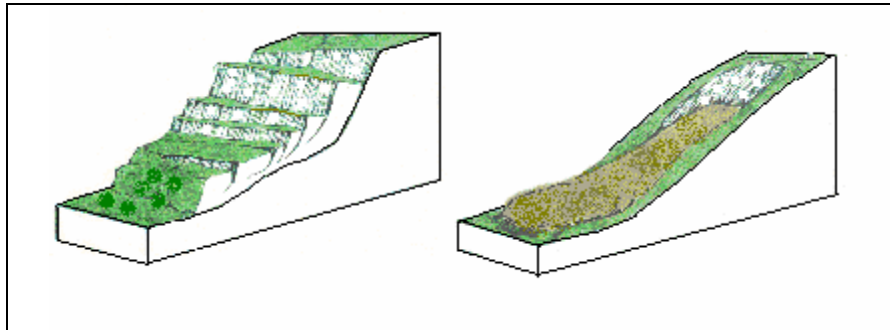


Fig. 12. Illustrated difference between a slump (left) and a flow (right). Modified from Geology Web Pages at <http://www.nicholas.duke.edu/eos/geo41/geo41.htm> (accessed 2007).

Slumps, or block collapse of rim material into the crater are indicative of weak or unconsolidated target material (Dypvik and Jansa 2003). Slump blocks are present in both the Mjølner and Chesapeake Bay crater structures, but not at Lockne (Ormö and Lindström 2000). Flows, or tongues of rounded deposits, have been observed in both

Chicxulub (Kring 2005) and Lockne (Von Dalwigk 2001) craters. Flows are different from slumps in that they are continuous and often rounded in shape.

### *Radial Gullies (RG)*

Radial channels carved by sediment-loaded waters induced by violent resurge are common in marine target craters (Ormö and Muinonen 2000; Von Dalwigk and Ormö 2001). Resurge gullies have been observed in both the Lockne (Lindström et al. 1996) and Kamensk (Ormö and Lindström 2000) craters (see Fig. 13). Even though resurge gullies are distinctive of marine impact craters, they tend to occur only in deeper water where the water depth exceeds the projectile diameter (Ormö et al. 2002). The water depth at the time of impact for Lockne has been estimated at 1000 m (Ormö et al. 2002) and for Kamensk at 100 to 200 m (Ormö and Lindström 2000). Thus, one can assume that shallow water depth limits the potential for the formation of radial gullies.

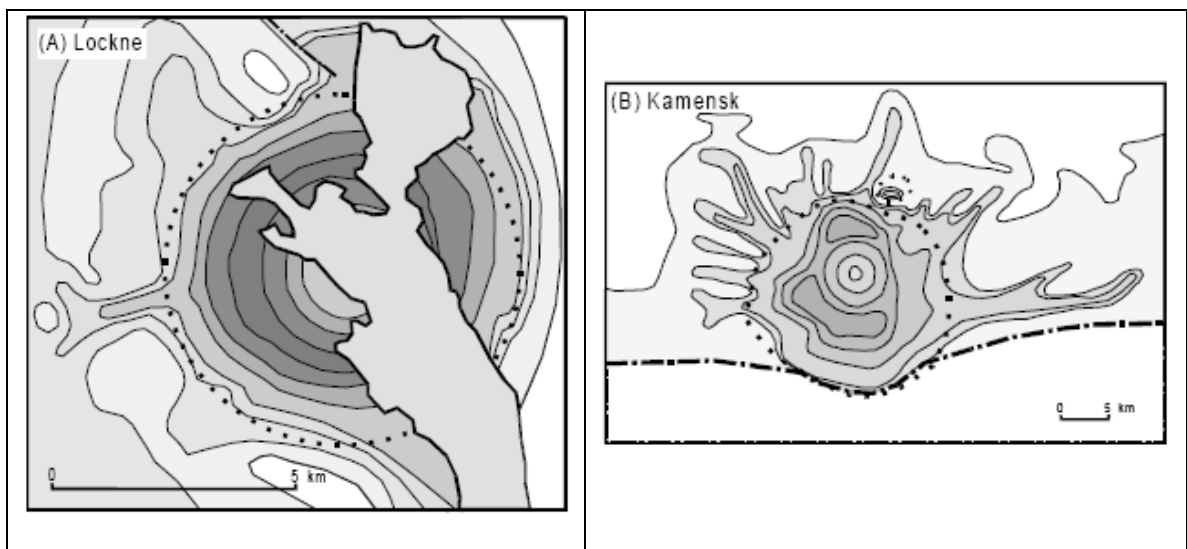


Fig. 13. Resurge gullies as observed in the Lockne and Kamensk craters in Eurasia. From Ormö and Muinonen (2000).

### *Resurge Deposits (RD)*

Resurge deposits may form inside or outside of the crater, depending on the depth of the target water, the strength of the crater material, and the location of the crater.

Intra-crater terrain is the evidence of resurge in the form of avalanches, slides, and slumps of mixed blocks inside the crater (Dypvik and Jansa 2003). Extra-crater terrain is the evidence of resurge in the form of resurge sediments and mixed blocks outside the crater (Dypvik and Jansa 2003). As discussed by King et al. (2006), the “extrastructure terrain” observed at Wetumpka is likely a product of collapse of the rim in response to resurge flow.

Resurge deposits on earth have been confirmed through drilling (von Dalwigk and Ormö 2001) and from fieldwork (King et al. 2006) in combination with subsequent sedimentological description.

### *Central Terrace (CT)*

A central peak terrace or a peak ring terrace is a large structure in the center of the crater, sometimes associated with equally flattened concentric rings (Dypvik and Jansa 2003). Development of flat-topped central uplifts has been predicted by some studies (Gault and Sonett 1982) and could be an indication of marine origin and that the structure has been buried under water for some time.

### *Rim Collapse (RC)*

Crater rims are usually tough features formed from crystalline bedrock. When craters form in sedimentary environments, the rims are not as pronounced or as strong. Often no remnant of rim is visible due to large amounts of inward slumping (Dypvik and Jansa 2003). This is sometimes also referred to as structural rim failure. Structural rim failure may be due to resurge activity or due to instability of the rim (King et al. 2006).

### *Subdued Topography (ST)*

Craters that exhibit subdued topography have little to no elevation of the rim above the surrounding topography. Subdued topography is indicative of the amount of erosion that has taken place since formation, and thus the amount of time that has passed. As erosion is often induced by water, it could also indicate that large amounts of water were present on the surface for an extended period of time (Ormö and Lindström 2000). Lack of an elevated rim is considered by Dypvik and Jansa (2003) to be one of the most distinctive features of marine impacts.

Note that none of the characteristics listed above can be used with certainty to imply marine origin. Other processes may be responsible for generating similar features in different locations; for example, complex craters on Earth often show signs of slumping without having formed in marine environments. However, if more than two of these characteristics are observed, it is likely that marine origin can be implied.



## Examples of shallow-marine craters

The study of terrestrial impact craters in shallow-marine environments helps to understand the formation and properties of these craters on the surface of Mars. Good terrestrial analogues formed in a continental shelf environment and now show a well-preserved structure and features that are described in detail. Some analogues are particularly useful in this study, and they include the larger Chesapeake Bay and Chicxulub craters, the medium Lockne and Mjølner craters, as well as the smaller Wetumpka crater (Fig. 14). Table 5 lists the locations and sizes of five terrestrial marine impact craters, as well as the estimated water depth upon impact for each of the events.



Fig. 14. Locations of selected terrestrial analogues for Martian shallow-marine craters – three out of five are located on the American plate, and the remaining two on the Scandinavian plate.

Table 5. Physical properties of selected terrestrial shallow-marine impact craters.

Crater	Location	Diameter (km)	Water Depth (m)
Chesapeake Bay	Virginia, USA	85	≤340 m
Chicxulub	Yucutan, Mexico	180	< 50
Lockne	Östersund, Sweden	13.5	> 200
Mjølnir	Barents Sea, Norway	40	300-500
Wetumpka	Alabama, USA	7.6	30-100

### *Chesapeake Bay*

The Chesapeake Bay impact structure is a ~85 km diameter crater that occurred about 35 million years ago into the shallow Atlantic Coastal Plain with an estimated water depth of ≤340 m (Poag 1997; Poag et al. 2004; Horton et al. 2006). The structure, currently buried beneath 150-400 m of post-impact sediments (Horton et al. 2006), is very well preserved but not visible from the surface. At the time of impact, the target consisted of crystalline basement overlain by 600-1000 m of unconsolidated sedimentary rocks and 200-500 m of saline water (Poag et al. 2004).

Collins and Wünneman (2005) modeled the Chesapeake Bay impact event and concluded that the main factor responsible for the morphology of the crater is the variation in strength of the layers present in the target. Without this variation in strength amongst the layers, it is likely that the diameter of the Chesapeake structure would have been around 40 km (Collins and Wünneman 2005). This is roughly half the size of the actual 85 km that has been determined through seismic profiling.

Chesapeake Bay crater exhibits an inverted sombrero morphology with an outer zone or annular trough and an inner zone or moat (Poag 1997; Horton et al. 2006). The rim has been subject to large-scale collapse and slumping resulting in crater-wall failure (Poag 1997; Horton et al. 2006). Numerous extensional collapse structures are observed in the seismic profiles, and these structures result in radial enlargement of the crater (Poag 1997; Horton et al. 2006).

### *Chicxulub*

The Chicxulub crater, with a diameter of approximately 180 km, is the largest crater that formed in a marine environment on Earth. Chicxulub occurred about 65 million years ago into a shallow sea with water depths of no more than 100 m (Pierazzo and Melosh 1999). The crater is well-preserved beneath a layer of sediments and not visible at the surface. Surge deposits are particularly well-preserved and include deposition of massive sands, debris flows, and collapse of the central peak into a peak ring (Dypvik et al. 2004; Kring 2005).

### *Lockne*

The Lockne crater is a ~13 km diameter impact structure that occurred about 455 million years ago (Ormö and Miyamoto 2002; Sturkell et al. 1998) in Sweden. Water depth at the time of impact was at least 200 m (Von Dalwigk 2001). Lockne crater contains very good examples of resurge gullies that have been associated with large-scale resurge flows (Von Dalwigk 2001). Four gullies as well as a few debris flow units have

been described and the rim has been classified as breached in more than one location (Von Dalwigk 2001).

### *Mjølnir*

The 40 km diameter Mjølnir crater in the Barents Sea (off the coast of Norway) formed about 140 million years ago (Tsikalas 1998). The estimated diameter of the asteroid is 1-3 km and the depth of the water roughly 300-500 m (Shuvalov and Trubestkaya 2002). The Mjølnir crater is not exposed at the surface, but instead is located on the seafloor and presently covered by ~350 m of water and 50-400 m of sediments (Dypvik and Jansa 2003). The structure was discovered from geophysical data, much like most of the shallow-marine craters. The Mjølnir crater rim is characterized by terraces that are bordered by faults and possible gullies (Dypvik and Jansa 2003). This crater also exhibits the classic inverted sombrero morphology with an inner zone of 8 km and an outer zone of 12 km (Dypvik and Jansa 2003). Rotated fault blocks are found in the annular trough (Ormö and Lindström 2000).

### *Wetumpka*

Wetumpka impact crater formed roughly 80 million years ago in a shallow sea of depths 30-100 m. The crater is 7.6 km in diameter and is the smallest of the five analogs discussed in this study. The remnants of the Wetumpka impact crater are not completely covered by sediments. The Wetumpka crater exhibits signs of numerous intra- and extra-crater resurge deposits as well as a structurally disturbed rim (King et al. 2002; 2006).

## **Remote Sensing**

Remote sensing is a crucial tool in studying the surfaces of objects, particularly in planetary science. In broad terms, remote sensing is the studying of a surface with electromagnetic radiation sensors that are at a distance from the studying site. Planetary exploration occurs almost entirely remotely, even with the exception of human space travel, remote sensing is still involved. (Ramsey and Christensen 1998; Carr and Garvin 2001)

Remote sensing can either occur passively by means of recording reflected light from surfaces or actively through sending and receiving signals. Common examples of passive remote sensing include photography such as the images taken by Mars Orbital Camera (MOC) and Thermal Emission Imaging System (THEMIS) as well as spectrography such as the spectra gathered by THEMIS. Examples of active remote sensing include RADAR (radio detection and ranging) or LIDAR (light detection and ranging), where time of flight of signals is measured. Data captured by Mars Orbiter Laser Altimeter (MOLA) are included here (Neumann 2001).

The different branches of passive remote sensing can be classified based on wavelength. Wavelength ( $\lambda$ ) and frequency ( $\nu$ ) are related through the velocity of light in a vacuum ( $c$ ), which is constant, by the following equation:  $c = \lambda \nu$ . Remote sensing commonly makes use of photography, which falls in the visual part of the light spectrum. Other common wavelengths are ultraviolet and infrared (Table 6).

Table 6. Common remote sensing fields in the infrared section of the electromagnetic radiation spectrum and their associated wavelengths.

<b>Remote Sensing Field</b>	<b>Wavelength</b>
Near-infrared (NIR)	0.7-1.4 $\mu\text{m}$
Mid-infrared (MIR)	1.4-3.0 $\mu\text{m}$
Far-infrared (FIR)	3-1000 $\mu\text{m}$

Thermal infrared (TIR) is a popular branch of remote sensing that falls within the far-infrared region (Ramsey and Christensen 1998). Martian surface minerals can broadly be classified by comparing the high-resolution thermal infrared spectra of surface minerals on Mars to thermal infrared spectra of common rock-forming minerals found on Earth (Christensen et al. 2000). To aid this process, Christensen et al. (2000) published a preliminary database (available at <http://rruff.geo.arizona.edu/doclib/hom/>) containing thermal emission spectra of common terrestrial rock-forming minerals. Thermal emission spectra of rock-forming minerals are obtained from Earth-orbiting satellites such as the Thermal Infrared Multispectral Scanner (TIMS) and the Advanced Spaceborne Thermal Emission and Reflection radiometer (ASTER), as well as the series of Earth Observing System (EOS) satellites, which all have similar spectral resolutions to those in orbit around Mars (Wright 2003; Christensen et al. 2000; 2004).

Active remote sensing involves sending a signal to a surface and measuring the time it takes the signal to be reflected back to the sensor. This is how altimetry data for the generation of topographic maps are gathered (Neumann 2001). Knowing the radius of the planet, the exact height of the sensor at the time, and the angle of the laser pulse,

the topographic height of the surface is determined through geometric principles (Abshire et al. 2000; Neumann 2001).

Planetary exploration of Mars by means of spacecraft started in 1964 with the launch of Mariner 4 (Kirk 2005). This spacecraft carried a camera that took about 20 close-up images of the planet. Mariner 6, 7, and 9 followed shortly and carried onboard narrow and wide angle cameras as well as ultraviolet and infrared spectrometers. The Viking orbiters and landers followed in 1975 and completely mapped the surface of Mars for the first time from orbit (Kirk 2005). Only in 1996 did another spacecraft successfully go to Mars. This time it was Mars Global Surveyor, carrying onboard the MOC and MOLA instruments (Smith et al. 2001). Mars Odyssey is currently in orbit around Mars and it carries a variety of remote sensing instruments, including a gamma ray spectrometer, a radiation spectrometer, and a multi-wavelength thermal spectrometer that can measure in both visual and infrared wavelengths (THEMIS). Fig. 15 shows four of the spacecraft deployed in the remote study of the surface of Mars, one of which is still operational today. Other current operational Mars orbiters include the Mars Reconnaissance Orbiter (NASA) and Mars Express (ESA) (Carr and Garvin 2001; Kirk 2005).

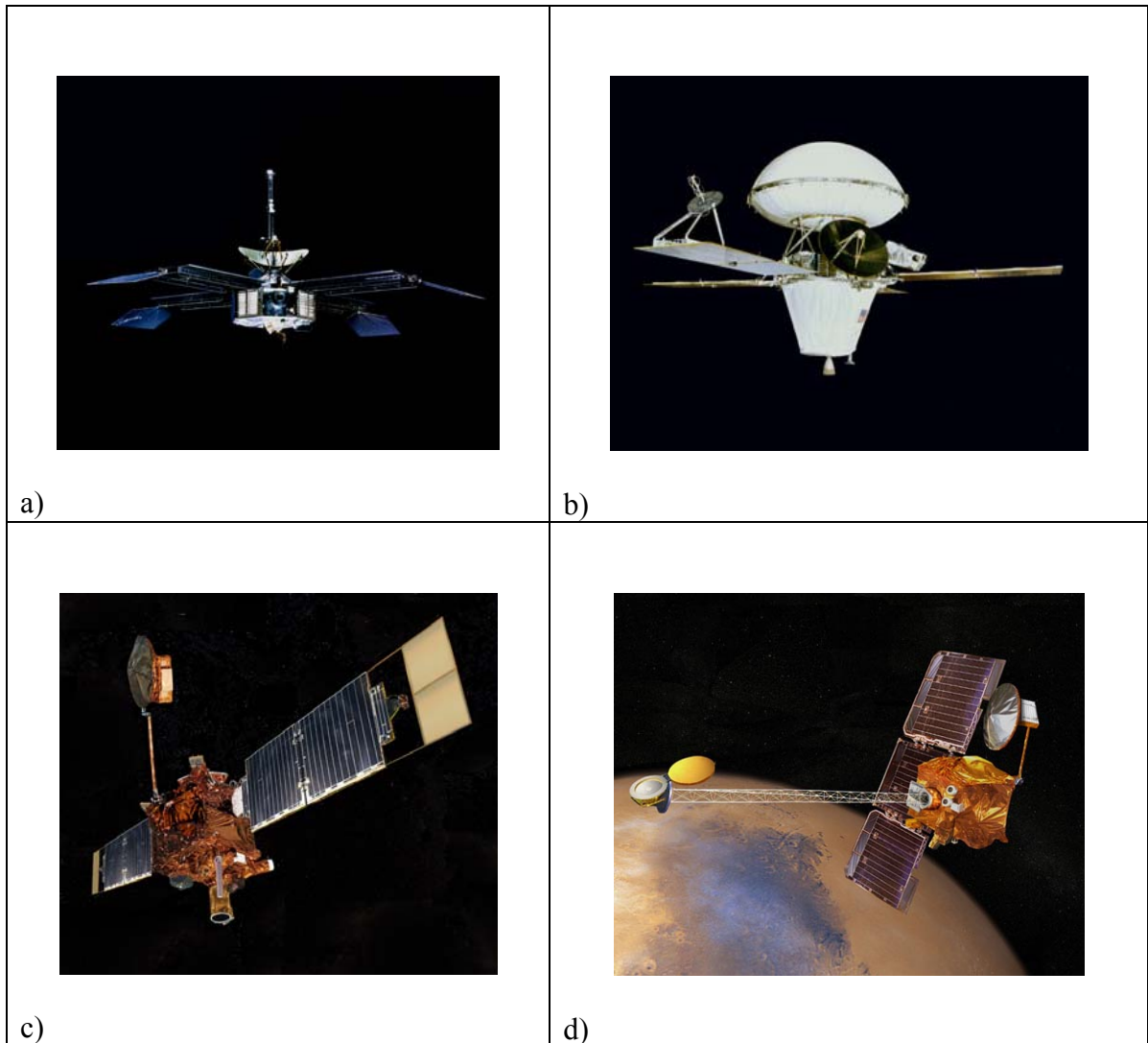


Fig. 15. Spacecraft that have gone to Mars include Mariner 4, launched 28 November 1964 (a); Viking Orbiter Lander 1 and 2, launched 20 August 1975 and 9 September 1975 respectively (b); Mars Global Surveyor, launched 7 November 1996 (c); and Mars Odyssey (still operating), launched 7 April 2001 (d). All images from NASA (available from <http://mars.jpl.nasa.gov/gallery/spacecraft/index.html>).

Based on data gathered through remote sensing, scientists have been able to draw conclusions about the morphology, mineralogy, and topography of Mars (e.g., Christensen et al. 2000; Aharonson 2001; Christensen et al. 2004; Boyce et al. 2005; Kirk 2005).



## **Summary**

This section discussed the many aspects of the study of shallow-marine impacts on Mars. First of all it is important to consider the evidence for water on the surface of Mars, and then to assume that the proposed shorelines of ancient oceans did indeed exist. Shallow-marine impact craters have distinct physical properties and characteristic features, some of which can be measured and/or seen from data captured by orbital sensors. Terrestrial analogs are few, yet hold important clues to the expected morphologies for shallow-marine impact craters. Remote sensing is a crucial tool in the study of planetary surfaces, particularly that of Mars, where humans are yet to set foot. The study of shallow-marine impact craters on planetary surfaces - a new branch of planetary geology - is just beginning to contribute to geoscience, and many facets of this topic are yet to be exposed.

## METHODS

This study employs datasets gathered by three different instruments. They are the a) Mars Orbiter Laser Altimeter (MOLA) and b) Mars Orbital Camera (MOC), which are onboard the Mars Global Surveyor (MGS) spacecraft, and c) Thermal Emission Imaging System (THEMIS) onboard the Mars Odyssey spacecraft. The spatial resolutions of these datasets are substantially better than that of the Viking images, which were previously used in geomorphological studies of this nature (Kirk 2005). After discussing the background of the missions involved in this study, the methods employed are discussed in three parts: data acquisition, data analysis, and data interpretation. The data acquisition section describes where the data are obtained from as well as the manners in which the data are acquired and processed. This section also explains how the shallow-marine impact crater candidates were chosen. The data analysis section deals with the quantitative investigation, particularly in terms of the physical parameters of the candidate craters. The data interpretation section categorizes the crater candidates by evaluating the marine characteristics through the use of a standardized ranking system.

## Background

Three of the most productive missions that have been sent to Mars are the Viking orbiters (V1 and V2), Mars Global Surveyor (MGS), and Mars Odyssey (MO). A timeline of events associated with these missions is outlined in Fig. 16. A variety of highly successful imaging sensors has been incorporated into these missions, including Mars Orbiter Laser Altimeter (MOLA), Mars Orbiter Camera (MOC), and Thermal Emission Imaging System (THEMIS); however, THEMIS is the only sensor of the three that currently is still operating.

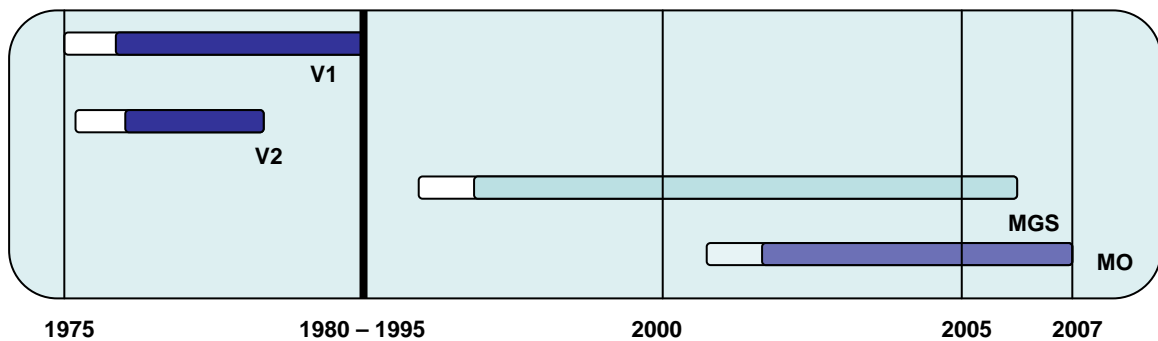


Fig. 16. Timeline depicting the stages in Mars exploration by Viking Orbiters 1 and 2 (V1 and V2), Mars Global Surveyor (MGS), and Mars Odyssey (MO). White areas indicate cruise time, and darker areas indicate sensor-operating time.

The main improvement of the MOLA, MOC, and THEMIS sensors over Viking imagery is in the category of spatial resolution (Table 7). Viking imaging sensors mapped the entire surface of planet in 150-300 m/pixel resolutions and only a few selected areas at lower resolutions (Kirk 2005). MOC images are generally at 2-10 m/pixel resolutions when taken with the narrow angle camera (Malin et al. 1992). THEMIS images are not quite as high-resolution, but still generally have resolutions of

around 20 m/pixel. MOLA resolution is of an entirely different kind and cannot be directly compared to that of MOC or THEMIS because MOLA data are topographic while MOC and THEMIS data are visual images. Topographic data by definition does not have a spectral resolution, which is why this information is not listed for MOLA in Table 7. MOC has the best radiometric resolution and is thus provides the most sensitive sensor, followed by MOLA and then by THEMIS. All three sensors have low temporal (related to frequency of image capture) resolutions because none of them were designed to capture surface change.

Table 7. Instrument specifics in terms of resolution for MOLA, MOC, and THEMIS (Malin et al. 1992; Abshire et al. 2000; Christensen et al 2002; Kirk 2005).

	<b>MOLA</b>	<b>MOC</b>	<b>THEMIS</b>
<b>Full Name</b>	Mars Orbiter Laser Altimeter	Mars Orbiter Camera	Thermal Emission Imaging System
<b>Maximum Visual Spatial Resolution</b>	130 m	1.4 m	18 m
<b>Spectral Resolution</b>	-	3 visual	5 visual 9 infrared
<b>Radiometric Resolution</b>	16 bit	32 bit	8 bit
<b>Temporal Resolution</b>	Low	Low	Low

### *Mars Global Surveyor*

NASA launched Mars Global Surveyor (MGS) on November 7, 1996, which went into orbit around Mars in September the following year (Smith et al. 2001). MGS carries the Mars Orbiter Laser Altimeter (MOLA) and the Mars Orbiter Camera (MOC), as well as two other scientific instruments (Abshire et al. 2000; Smith et al. 2001).

The main objective of the MOLA investigation was to generate an accurate global topographic map of Mars with sufficient resolution to produce elevation data that can be useful in studies of planetary geology at a large scale (Abshire et al. 2000; Smith et al. 2001). Shortly after MGS went into orbit, MOLA started transmitting altimetric data. The MOLA spatial resolution is approximately 130 m/pixel and horizontal resolution approximately 930 m/pixel (Smith et al. 2001). The vertical accuracy is approximately 1-2 m (Roark et al. 2004; Howenstein 2006). Signal strength, pulse width, detector noise, and background level are all factors that affect the accuracy of the signal (Abshire et al. 2000). Prior to MOLA, topographic measurements were based on photogrammetric analyses of Viking stereo image pairs, with horizontal errors as large as a few kilometers (Smith et al. 1998; Abshire et al. 2000; Kirk 2005).

The main objective of the MOC investigation is to obtain high-resolution imagery of the surface with which more in-depth studies of areomorphological features can be done (Malin et al. 1992). MOC has two wide-angle cameras, one in the blue part of the visual spectrum and one in the red, with 280 m/pixel spatial resolution and a narrow-angle camera with a maximum spatial resolution of 1.4 m/pixel.

Mars Global Surveyor is not operating anymore. MOLA sent its last signal in 2000 and MOC in 2006, yet the data that these instruments collected (MOC alone collected more than 212,000 images; Malin Space Science Systems MOC database at <http://www.msss.com/>) have not been fully analyzed and interpreted

### *Mars Odyssey*

Mars Odyssey, launched by NASA on April 7, 2001, arrived at Mars in October of that same year and is still operational. Odyssey carries onboard with it the Thermal Emission Imaging System (THEMIS) as well as two other scientific instruments. THEMIS has five visual bands with a spatial resolution of 18 m/pixel and nine infrared bands with a spatial resolution of about 100 m/pixel. The main objective of THEMIS is to compile a mineralogical map of the surface of Mars based on thermal infrared spectroscopy (Christensen et al. 2000), but a large amount of visual imagery data are also being gathered to fill the gap between the high-resolution MOC data and the lower resolution Viking data. More than 78,000 visual images have been taken to date with THEMIS, with a further 70,000 images taken in the infrared band of the spectrum (Arizona State University THEMIS database at <http://themis-data.asu.edu/>).

## **Data Acquisition**

The datasets are available either through an interactive website called Planetary Interactive GIS on-the-Web Analyzable Database (PIGWAD), which is maintained by the astrogeology team of the USGS, or through the Planetary Data System (PDS), which is maintained by NASA (Hare and Tanaka 2000; Hare and Tanaka 2001; Hare et al. 2003). The Malin Space Science Systems (MSSS) host MOC images in an online database, and often the MSSS database is easier to access than the PDS database due to a simpler, interactive map interface. Arizona State University (ASU) host THEMIS images in a similar online database and the images are also accessible through an interactive map interface.

### *MOLA data*

MOLA data are collected in vector format as binary points. The datasets contain thousands of vector points recorded for each individual track. Altimetric data from MOLA can be manipulated to yield profiles, and can also be used to calculate slope and elevation statistics (Aharonson et al. 2001).

MOLA data as captured in the original format cannot be used directly in a Geographic Information System (GIS). The data have to be processed and this requires several steps as shown in Fig. 17 (Smith et al., 2001). The raw data are stored as Aggregated Experiment Data Records (AEDRs), a Level 0 binary file product in a vector format, which are produced directly from downlink telemetry (Smith et al. 2001). Level

1 processing applies orbit calibration factors to the AEDRs to produce Precision Experiment Data Records (PEDRs). The output format is again a binary point vector. The PEDRs are subsequently converted to a raster format that is called Experiment Gridded Data Records (EGDRs) (Smith et al. 2001). EGDRs are stored in two forms, Initial EGDRs and Mission EGDRs. MEGDRs are topographic maps generated from Level 2 ASCII text files, and can be used to generate GIS shapefiles (Hare and Tanaka 2000).

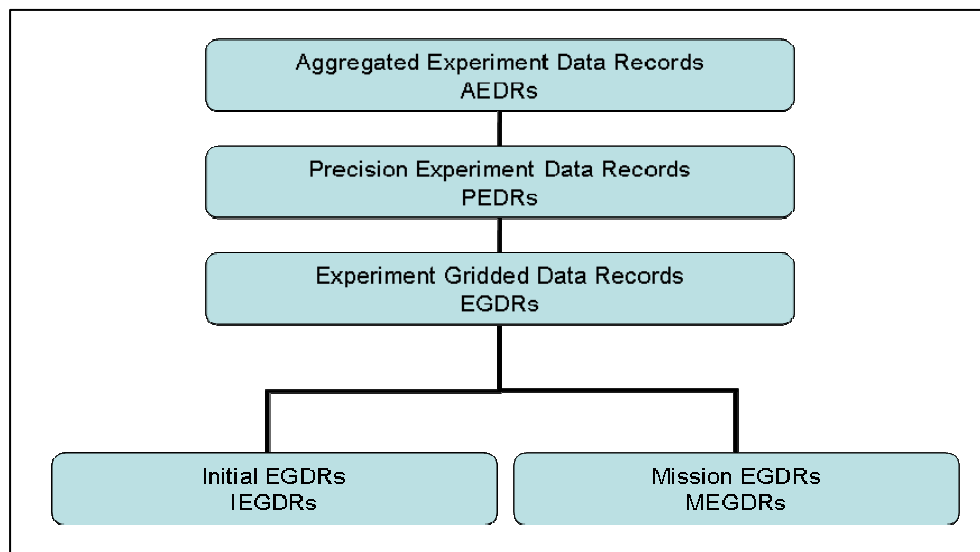


Fig. 17. Different data products that can be derived from raw MOLA data. MEGDRs are used in a GIS, and are therefore used in this study.

To interpret MOLA data as altimetric profiles, precision orbit information is merged with the data to locate each spot on the planet and determine its radius at that spot. Unlike the Earth, Mars does not have a standard sea level, but rather a reference datum representing a mean surface elevation. This reference datum is referred to as the areoid (comparable to the Earth's geoid). The radius minus the areoid is the elevation.



MEGDRs usually consist of at least three, sometimes four, objects: a) a planetary radius as measured by the MOLA instrument, b) an areoid model, c) a topographic map computed as the difference between the radius and the areoid, and d) a count of the number of MOLA hits per map unit.

The elevation data used in this study are MEGDRs, released through the PDS on May 7, 2003, and are at 128 m/pixel resolution. All the global maps are in simple cylindrical projection using a planetocentric, east-positive longitude coordinate system assigned by the International Astronomical Union in 2000 (Kirk 2005). The 128 m/pixel MEGDRs are stored as 16 image tiles, based on coordinates (Fig. 18). The location of the study area lies well within two of these tiles that cover the area between 0 and 44 degrees north, and between 270 and 90 degrees east. For this study, the topographic northern hemisphere tiles for areas bounded by 0°-44° N and 0°-90° E (megt44n000hb.img) and by 0°-44° N and 270°-0° E (megt44n270hb.img) are downloaded as Imagine image files. Along with their respective label files (also downloaded from the PDS), the gridded records are imported into ArcGIS as base maps.

The vast amount of MOLA data products make it necessary to specify exactly which particular files are used and why. File names for the global image maps use the format of MEGp<sub>xx</sub>n<sub>yyyy</sub>rv.IMG. Table i in the Appendix lists the symbols used in the file path and their respective definitions. Topography files, as opposed to count files, are all that are needed in this study because they are sufficient for drawing profiles in the

software program GRIDVIEW – a scientific visualization tool developed by NASA’s Goddard Space Flight Center specifically for use with gridded MOLA data (Roark et al. 2004).

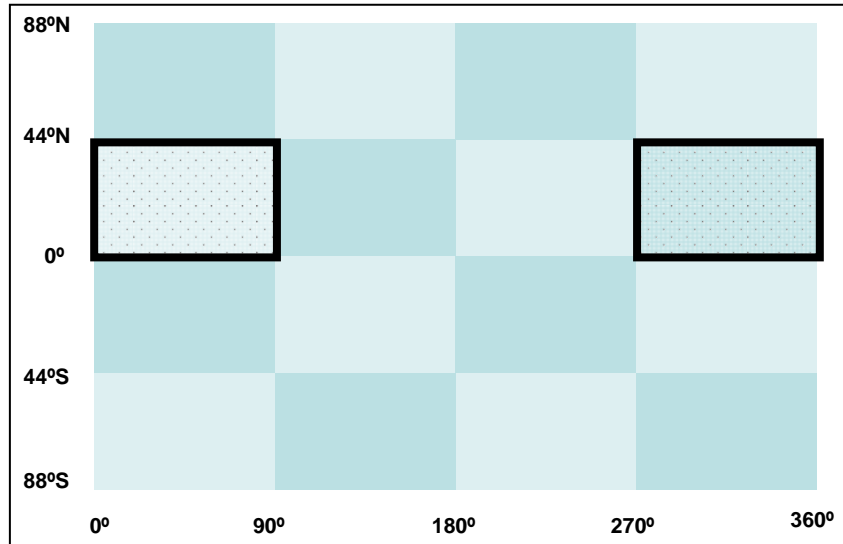


Fig. 18. Tiling scheme for the 128 pixel/degree MEGDRs from the Planetary Data System (PDS), indicating the two tiles that are used as base maps in this study.

A raster MOLA product from the USGS is also used as a base map for mapping the location of the study area and the candidate craters. This raster file is a hillshade alteration of original topographic data for the north pole and not a gridded data product like the topography files mentioned above.

The coordinate system of the MOLA base map is an equidistant cylindrical projection with central meridian at 180° and a datum called GCS\_Mars\_2000\_sphere, downloaded from PIGWAD.

### *MOC and THEMIS data*

MOC and THEMIS datasets are collected in raster format from PIGWAD, MSSS, and ASU. There are a few limitations to the visual data, including limited coverage of the northern plains due to cloud cover. In addition, some errors in the transmitted telemetry stream cause gaps in images, and even though some images can be corrected, a few cannot, leaving parts of these images useless (Caplinger et al. 1999).

The Malin Space Science Systems (MSSS) website holds most of the MOC images at [http://www.msss.com/moc\\_gallery/](http://www.msss.com/moc_gallery/). On this website, each biannual group of orbits has a global map of Mars that is divided into 30 quadrangle sections (Fig. 19), and sections can be entered by clicking on it. Each section then has an enlarged picture on which there are hyperlinks pinned to each image in the location in which it was taken. Images within the study area are captured by opening these hyperlinks and downloading the data. Composite images and images with technical problems are excluded from the dataset, and all images have center coordinates that fall strictly within the study area. Furthermore, a few of the last images taken by MOC are not included in this study as these were never uploaded to the MSSS website. Considering that these images were taken in the last three months of a nine-year study, not too much emphasis is placed on trying to locate these images.

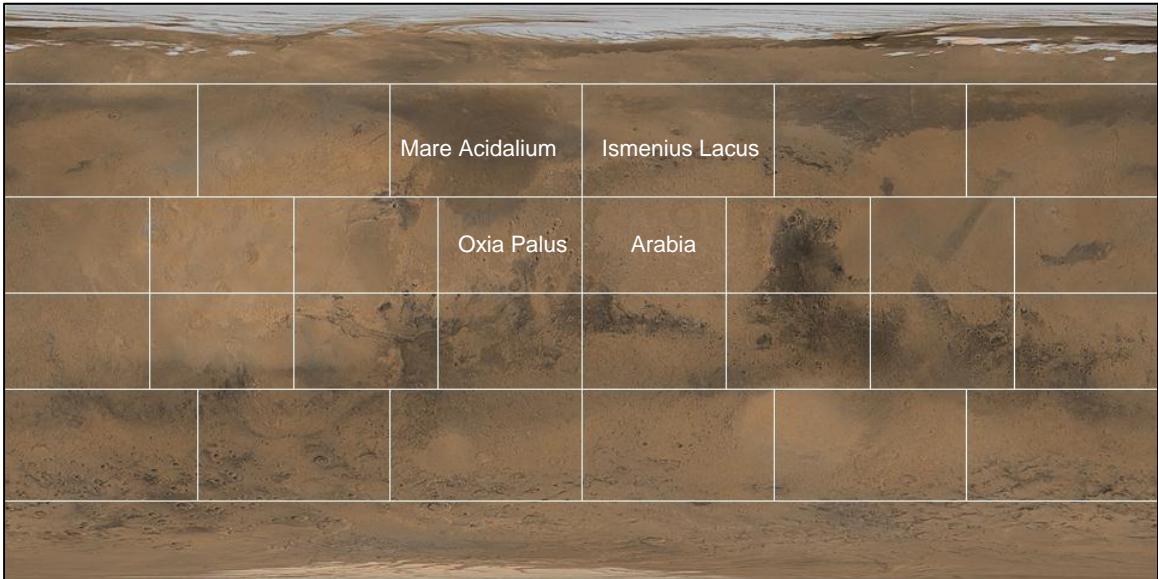


Fig. 19. The study area falls within four of the central quadrangles in the Northern Hemisphere – Mare Acidalium, Oxia Palus, Ismenius Lacus, and Arabia. From Malin Space Science Systems (MSSS).

The downloaded images are all processed and map-projected. As the images are downloaded, the image identification number and center coordinates are entered into a database. The database is used to organize the data collection, to simplify the process of going back for THEMIS data, and to get a visual idea of the quantity of images in the various areas. From the Arabia Terra region, the 868 available images are screened for shallow-marine crater characteristics. Firstly, 85 useful images are identified. These images show interesting features that could potentially be marine in origin. Secondly, potential shallow-marine crater sites are documented in the database from the population of useful images, based on the presence of shallow-marine crater characteristics such as evidence for wet mass movement and resurge deposits, as discussed in the previous chapter. For all the useful images, the original raw data are also downloaded in

.imq (different from the .img Imagine image files) file format so that the images could be processed as described below.

Raw MOC data are stored as compressed Standard Data Products, or .imq files. Raw data need to be decompressed, corrected, and projected for use in a GIS. A common software application, Integrated Software for Imagers and Spectrometers (ISIS), is used to areo-correct the imported planetary datasets (Hare et al. 2003). The compressed .imq files are downloaded and radiometrically calibrated to give Level 1 image files. Subsequently, these files are converted to map-projected Level 2 image files, which are used as layers in a GIS. ISIS runs in the command line from a UNIX based operating system. Once ISIS is installed, a few basic commands will spatially register the file to a specified coordinate system and projection (Table ii in Appendix).

THEMIS images are hosted by ASU and can be accessed directly through an interactive map on their Mars Odyssey website, or through PIGWAD. For all the potential candidates, THEMIS visual images are also downloaded. The resolution of THEMIS images is a little lower than that for MOC images, but the THEMIS images cover a larger area. Thus, the THEMIS images are used to place MOC images in context of location (e.g., de Villiers et al. 2006). To complete the image database, a second search is done in PIGWAD to ensure that all available MOC and THEMIS imagery for each candidate site has been acquired.

## **Data Analysis**

GIS is particularly useful for this project due to its ability to overlay multiple datasets such as MOC, MOLA, or THEMIS imagery or even a geological map and other graphical datasets tied to a geodetic framework.

The topographic maps, or digital elevation models (DEMs) produced with MOLA are used as base maps upon which high-resolution images can be overlain. Vector features such as shorelines and crater locations are digitized as new layers directly from the base map or from the high-resolution images. The images are spatially aligned with the basemap through a process called georeferencing. This process involves picking ground control points on the base map and on the image and manually aligning the new image with the base map.

Using ArcGIS, the crater features are digitized and the crater depths and diameters are calculated, providing the necessary comparative data on some of the physical properties of Martian craters. Layers are created in ArcCatalog where spatial properties are also defined for each layer, after which the layers are imported to ArcMap. Once the coordinate system has been correctly defined and the map projection correctly assigned, then the diameters of craters are directly measured with the measure tool. Depths of craters are calculated by querying the point values inside and outside the crater. Crater depths were measured at four locations both inside (depth of crater, or dc) and outside (height of surroundings, or ds) the crater, as well as at four location on the rim

(height of the rim, or dr). The average of the four locations, generally located north, east, south, and west of the crater, are used. The depth of the crater is calculated by subtracting the height of the crater floor (dc) from the height of the rim (dr).

With the use of GRIDVIEW, profiles of exceptional candidates are drawn and included in the results. To draw a profile in GRIDVIEW, a gridded Imagine (.img) image file such as a MEGDR is uploaded and the coordinates and resolution defined. The image can be enlarged to view a particular area and the color stretch can be maximized to enhance topographical differences. Once the profile is drawn, the point data are exported as a text file that is subsequently imported into a spreadsheet where the profile is re-drawn and simplified for clarity.

## Data Interpretation

Once the database of MOC images and their physical properties is compiled, a list of shallow marine crater characteristics was constructed by which the craters would be evaluated. The characteristics were chosen based on those reported in literature for marine craters on Earth and from four Martian candidate craters identified by Ormö et al. (2004). Ormö et al. (2004) identified four shallow-marine impact craters within Arabia Terra, from Viking images. Three of the four candidates are located together at site 1 near 39°N and 349°W and the remaining candidate is located at site 2 which is at approximately 39°N and 001°W (Fig. 20).

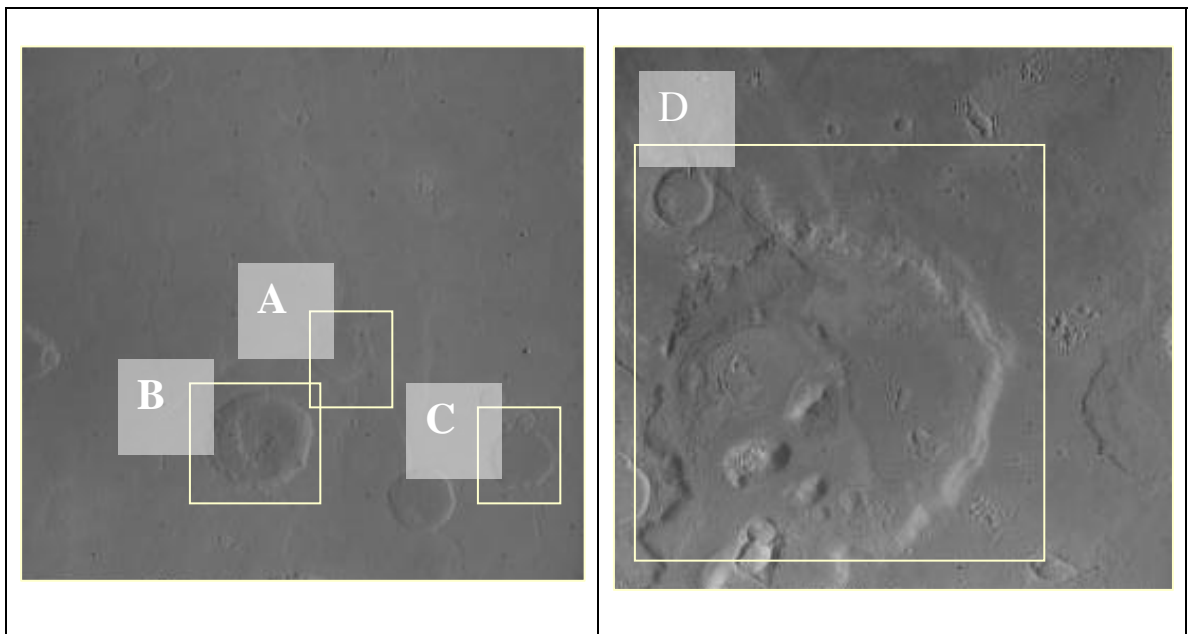


Fig. 20. The locations of Craters A, B, C, and D (as indicated by Ormö et al., 2004) in Viking images F529A09 and F072A32, respectively. Images from the Planetary Data System (PDS).



The candidate sites were analyzed in more detail with the use of high-resolution MOC and THEMIS imagery. For site 1 in the eastern section of the study area, a series of MOC and THEMIS images is available for Crater B, but not much is available for either Crater A or Crater C. For site 2 in the center of the study area, a total of 15 MOC images are available, but no THEMIS data. Fig. 21 shows the overlay of imagery that was done for Crater B.

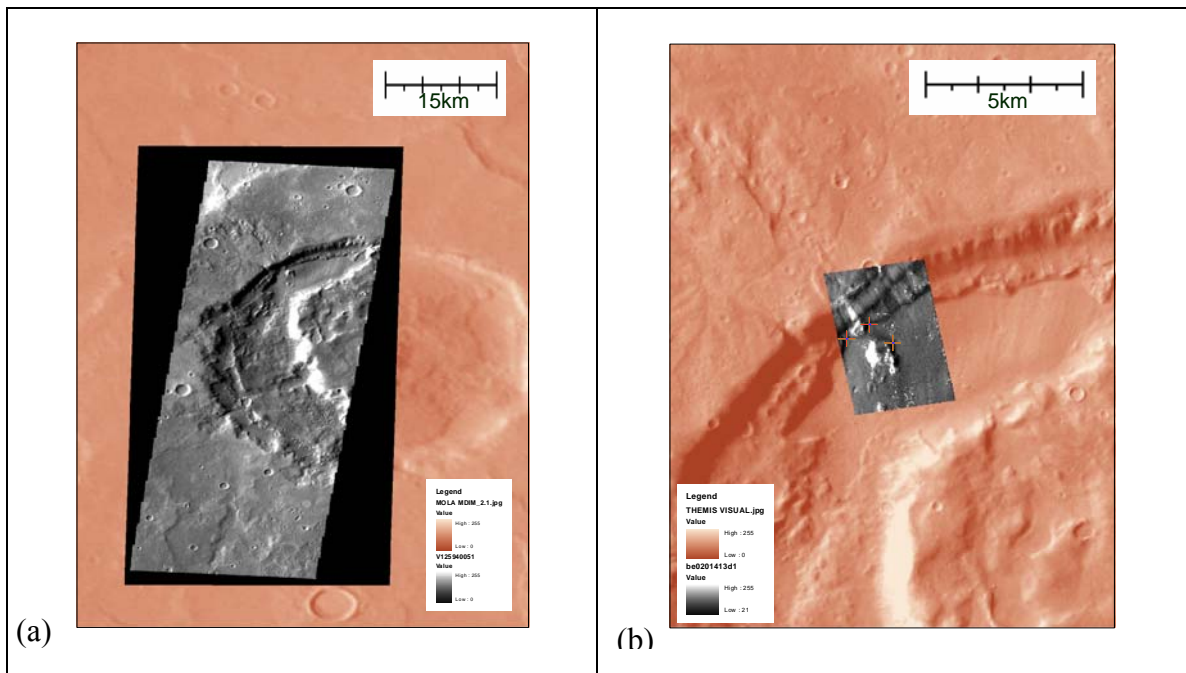


Fig. 21. THEMIS raster image of a Crater B on top of MOLA DEM (a) and georeferenced MOC image draped over THEMIS image (b).

The following characteristics are observed: a) evidence of wet mass movement; b) radial gullies entering the crater from one or more location on the crater rim; c) resurge deposits; d) central terraces; e) collapsed rims; and f) subdued topography (Fig. 22). Wet mass movement occurs when saturated sediment is mobilized, either in a brittle or ductile manner (Dypvik and Jansa 2003). Radial gullies are common in deeper continental

environments where the water resurge breaches the crater rim (Ormö and Muinonen 2000; Von Dalwigk and Ormö 2001). Resurge deposits are sometimes difficult to discern from satellite imagery, but include blocks of rim material inside or outside the crater (Dypvik and Jansa 2003). Central terraces indicate long-standing water, potentially spanning from right after formation until the end of the oceanic phase (Gault and Sonett 1982; Dypvik and Jansa 2003). Collapsed rims are usually associated with wet mass movement and resurge (Dypvik and Jansa 2003), but are different in the sense that wet mass movement can occur without a breach in the rim. Rim collapse is usually associated with radial gullies, however, it is also observed without the presence of identifiable gullies. Finally, subdued topography does not only indicate that water may have persisted on the surface for an extended period of time, but it is also the result of weathering and therefore relates to the age of the crater population under examination. If an ocean once existed in the northern lowlands on Mars, it occurred during the late Noachian, very early in Mars's history (Parker 1989; Fairén et al. 2003), leaving plenty of time for the craters to become degraded and the surrounding topography to become subdued.

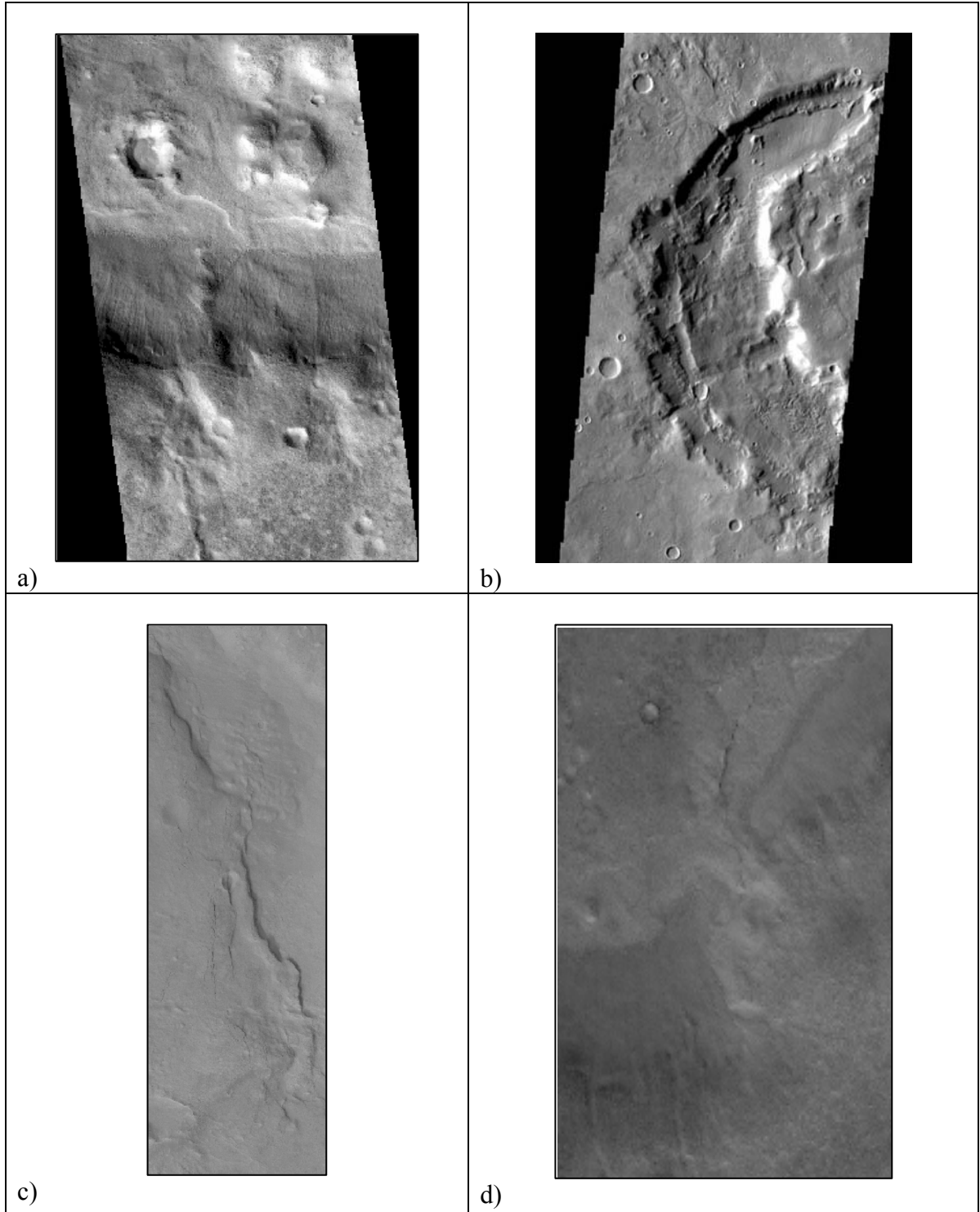


Fig. 22. Subdued topography and no elevated rim (a) (E0600102). Central terrace (b) (V12594005). Large radial gullies (c) (R0500631). Large-scale wet mass movement (d) (R1402326). Images from Malin Space Science Systems (MSSS) and PIGWAD.

The features identified in the craters proposed by Ormö et al. (2004) form the basis of the quantification system in this study. Features reported in literature for terrestrial analogs supplement these characteristics. Therefore, following from the observed features listed above, the six categories in the candidate database are wet mass movement; radial gullies; resurge deposits; central terraces; rim collapse; and subdued topography.

The six categories are weighted to ensure that more important characteristics carry more value. Wet mass movement is likely the most important characteristic, however, it should be noted that there are numerous ways of forming wet mass movement features and that these features do not only occur in shallow-marine environments. Resurge gullies are likely the most indicative characteristic, however, these features are more likely to form in deeper water (von Dalwigk and Ormö 2001) and are thus not expected to be common in Arabia Terra.

Within the quantification system, wet mass movement comprises 40% of the total. This includes 20% for evidence of slumping (small or large scale) and 20% for evidence of debris flows (small or large scale). Radial gullies contribute a further 20%, where one gully is 10%, and two or more gullies is 20%. Resurge deposits, central terraces, rim collapse, and subdued topography each contribute 10% to the overall rating. Fig. 23 shows the distribution of weight for each of the characteristics. These values

were chosen to reflect relative importance of various characteristic features. Wet mass movement is an important, relatively indicative factor, and as such comprises 40% of the score. Radial gullies, though not as common in shallow water as in deeper water, is also indicative and therefore comprises a further 20% of the score. Resurge deposits are more difficult to discern from orbital imagery, resulting in the factor only comprising of 10% of the score. Rim collapse, central terrace, and subdued topography are all factors that are less indicative of marine origin, and thus make up 10% each of the total score.

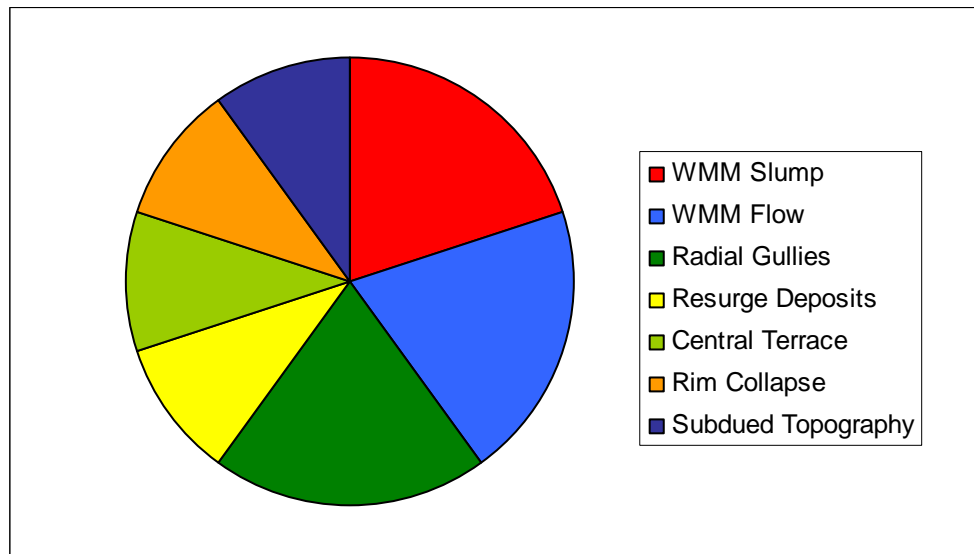


Fig. 23. Weighted distribution of the six classes of shallow-marine crater characteristics. Note that wet mass movement (WMM) is split into two sub-categories.

With this system it is possible to crudely quantify the features observed and to rate each crater based on properties associated with marine craters on Earth. Each candidate crater is assigned a total score and these values can be used to rank and classify types of shallow-marine crater candidates.

The database of shallow-marine crater candidates is included in this thesis in electronic format along with all the images that are discussed on a CD. In addition to the database, all images used in this thesis along with all figures are included on the attached CD. Interpretation of the results includes a discussion on the physical properties and characteristics of some exemplary candidates.

## RESULTS

The results of the analysis of crater characteristics are discussed in detail, because the crater characteristics are the parameters used in the quantification system. The quantification system was designed to rank potential crater candidate sites and to assign total scores indicating degrees of certainty of marine origin to these craters. As mentioned before, it should be noted that none of the crater characteristics can be used with certainty to apply marine origin, and as such, the total score assigned to a crater is only an estimation of the potential for that crater to have been formed in a shallow-marine environment. The candidate sites were analyzed in more detail with the use of high-resolution MOC and THEMIS imagery. Three sets of analyses were done: a) a pilot analysis to act as reference for subsequent sets; b) an initial analysis based on available MOC imagery for the study area; and c) a second analysis based on MOLA topography. The pilot analysis was done on the potential craters proposed by Ormö et al. (2004). The initial analysis is referred to as Set A and the second analysis as Set B. The three analyses are discussed separately, but all candidate craters are shown in Fig. 24. The analysis of physical parameters were not the primary aim of this study, but do contribute some value and are therefore briefly discussed at the end of this section.

All of the crater candidate sites fall north of (within) the Meridiani shoreline (shown in red on Fig. 24) proposed by Edgett and Parker (1997), and only a few fall north of (within) the Arabia shoreline (original Contact 2 – shown in yellow). The Deuteronilus shoreline (Parker 1989; Edgett and Parker 1997; Fairén et al. 2003) is likely the result of a smaller, more recent ocean and is indicated in blue in the figure. The location of this shoreline is largely outside the study area and is therefore not of further relevance in this study. The study area is indicated by the gray rectangle and can be seen to encompass a large part of the Arabia Terra continental shelf.

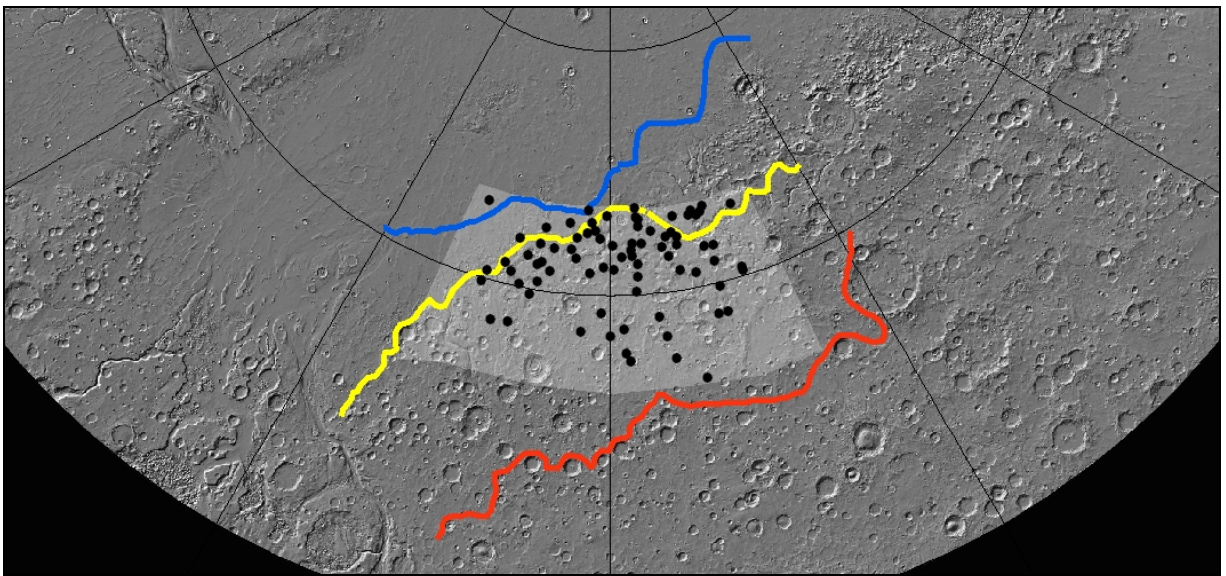


Fig. 24. Locations of potential shallow-marine impact craters in relation to the three shorelines proposed by Parker et al. (1989) as well as Edgett and Parker (1997). North polar projection hill-shade base map is from the USGS and is based on MOLA topographic data. Study area is shown by the gray rectangle.



## Ormö et al.'s candidate crater results

The four craters proposed by Ormö et al. (2004) as potential shallow marine impact craters were rated in the quantification system and the results are shown in Table 8. The total value is a number ranging from 0.0 to 1.0, reflecting the percentage confidence that a particular crater is of marine-origin. All four of the craters attained total scores of 0.5 or greater, yet only Crater D has a total score higher than 0.7.

Table 8. Evaluation of Ormö et al.'s (2004) potential shallow-marine crater candidates.

Candidate	Characteristics of Ormö et al. Candidate Craters						TOTAL	
	WMM		RG	RD	CT	RC		ST
	20% (Slump)	20% (Flow)	20%	10%	10%	10%		10%
A	0.5	0	1	0	0	1	1	0.50
B	1	0	0.5	0	1	1	1	0.60
C	0.5	0	1	0	0	1	1	0.50
D	1	0.5	1	0	1	1	1	0.80

*WMM – Wet Mass Movement; RG – Radial Gullies; RG – Resurge Deposits; CT – Central Terrace; RC – Rim Collapse; ST – Subdued Topography*

To visually interpret these results, a stacked histogram is plotted with all the variables shown as individual blocks (Fig. 25). Total scores range from 0.5-0.8 as even these prime examples do not exhibit all possible characteristics on the list. From Fig. 25 it is clear that Crater D is the most likely of the marine impact crater candidates proposed by Ormo et. al (2004) to be a shallow-marine impact crater. A total score of 0.8 is assigned to Crater D. Five of the six categories have features present in Crater D, and both slumps and flows are observed in the Wet Mass Movement category. Resurge deposits are not evident from the imagery, and this is likely due to the difficulty in observing such a feature from orbital imagery. Crater D is discussed in the next chapter.

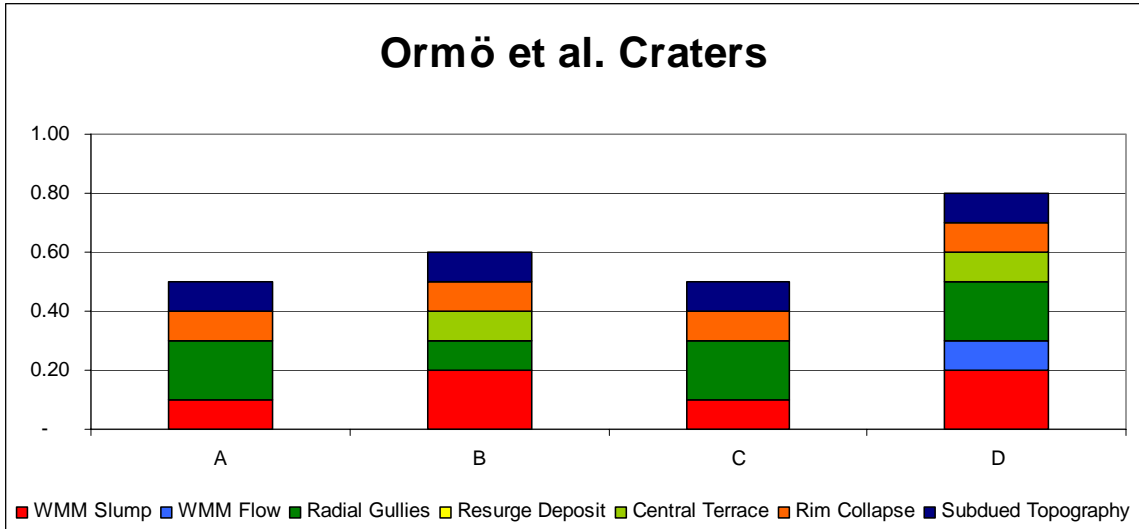


Fig. 25. Stacked columns with individual contributions to the overall rank for the craters proposed by Ormö et al. (2004).

## **Results from Set A**

In the database of MOC images in Arabia Terra there are 868 images that were taken during the period September 1997 to September 2005. From these images, 86 are classified as useful, and 65 of these images are potential candidates for marine targets (see Table iii in the Appendix). After carefully analyzing these images, a residual of 51 proved to have some significance to this study. Some of the 51 images are of the same crater, and thus there are a final 40 candidate craters which are identified from the imagery. THEMIS images were subsequently downloaded for the 40 candidate sites. The view of the candidate site was expanded with the use of lower resolution context images provided by Malin Space Science Systems as well as available THEMIS images. This proved to be useful particularly in larger craters where only parts of the structure are visible in any one image.

Fifteen of the candidate craters were found to be too small (diameters <10 km) to fall within the population for this study and were thus discarded. The 25 remaining craters were divided into three groups based on size. These divisions were created because the size of the crater could affect the morphology of the crater (Dypvik and Jansa 2003), and as such an effective assessment of craters can only be done if similar craters are compared with each other. Small craters have diameters of 10-30 km, medium craters have diameters from 30-50 km, and large craters have diameters 50-100 km. The 25 shallow-marine crater candidates were rated for shallow-marine origin and the craters and their ratings are listed in Tables 9, 10 and 11.

Table 9. Evaluation of characteristics of small shallow-marine crater candidates. Exemplary ranking candidates are shown in italics.

Candidate	Characteristics of Small Candidate Craters							TOTAL
	WMM		RG	RD	CT	RC	ST	
	20% (Slump)	20% (Flow)	20%	10%	10%	10%	10%	
1	0.5	1	0.5	0	0.5	1	0.5	0.60
2	1	1	0	1	0	1	0.5	0.65
3	1	1	0	0	0.5	1	1	0.65
5	1	0.5	0	0	0	0	1	0.40
6	<i>1</i>	<i>0</i>	<i>1</i>	<i>0.5</i>	<i>0.5</i>	<i>1</i>	<i>1</i>	<i>0.70</i>
7	1	0	0	1	0	1	0.5	0.45
9	1	0	0	1	1	0	1	0.50
14	0	0.5	0	0	1	0	1	0.30
15	1	0	0.5	0	1	1	1	0.60
16	1	0	0	1	0	1	1	0.50
17	<i>1</i>	<i>0</i>	<i>0.5</i>	<i>1</i>	<i>1</i>	<i>1</i>	<i>1</i>	<i>0.70</i>
18	1	0.5	0	1	0.5	0.5	1	0.60
19	1	0.5	0	1	0.5	0	1	0.55
24	<i>1</i>	<i>1</i>	<i>1</i>	<i>1</i>	<i>1</i>	<i>1</i>	<i>0.5</i>	<i>0.95</i>
27	1	0.5	0	0	0	0	1	0.40
30	0.5	0	0	0	1	0	1	0.30
32	1	0	0	1	0	0	1	0.40
37	0.5	0	0.5	0	0	0	1	0.30
38	1	0	0	0.5	1	1	1	0.55
40	1	0.5	0	1	0	1	1	0.60

WMM – Wet Mass Movement; RG – Radial Gullies; RG – Resurge Deposits; CT – Central Terrace; RC – Rim Collapse; ST – Subdued Topography

Table 10. Evaluation of characteristics of medium shallow-marine crater candidates.

Candidate	Characteristics of Medium Candidate Craters							TOTAL
	WMM		RG	RD	CT	RC	ST	
	20% (Slump)	20% (Flow)	20%	10%	10%	10%	10%	
Medium								
8	1	0	0	1	1	0	1	0.50
12	1	0	0	0	1	0	1	0.40
25	1	0	0.5	1	1	0	0.5	0.55
35	0.5	0	0	0	1	0	1	0.30

WMM – Wet Mass Movement; RG – Radial Gullies; RG – Resurge Deposits; CT – Central Terrace; RC – Rim Collapse; ST – Subdued Topography

Table 11. Evaluation of characteristics of large shallow-marine crater candidates.

Candidate	Characteristics of Large Candidate Craters							TOTAL
	WMM		RG	RD	CT	RC	ST	
	20% (Slump)	20% (Flow)	20%	10%	10%	10%	10%	
26	0.5	0.5	0	1	0	1	1	0.50

*WMM – Wet Mass Movement; RG – Radial Gullies; RG – Resurge Deposits; CT – Central Terrace; RC – Rim Collapse; ST – Subdued Topography*

In Fig. 26, ratings of all the craters from Set A, the craters are organized based on size. The first twenty craters are small (D = 10-30 km), the next four are medium (D = 30-50 km), and the last one is large (D = 50-100 km). It is evident from the data that the population is skewed to the smaller sizes. This occurrence is addressed in the next section. Scores range from 0.2-0.95 with an average of 0.52. The three highest ranked craters are Crater 6, Crater 17, and Crater 24, and all are small. These three craters, as well as the associated ArcGIS overlays and GRIDVIEW profiles, are discussed in the next chapter.

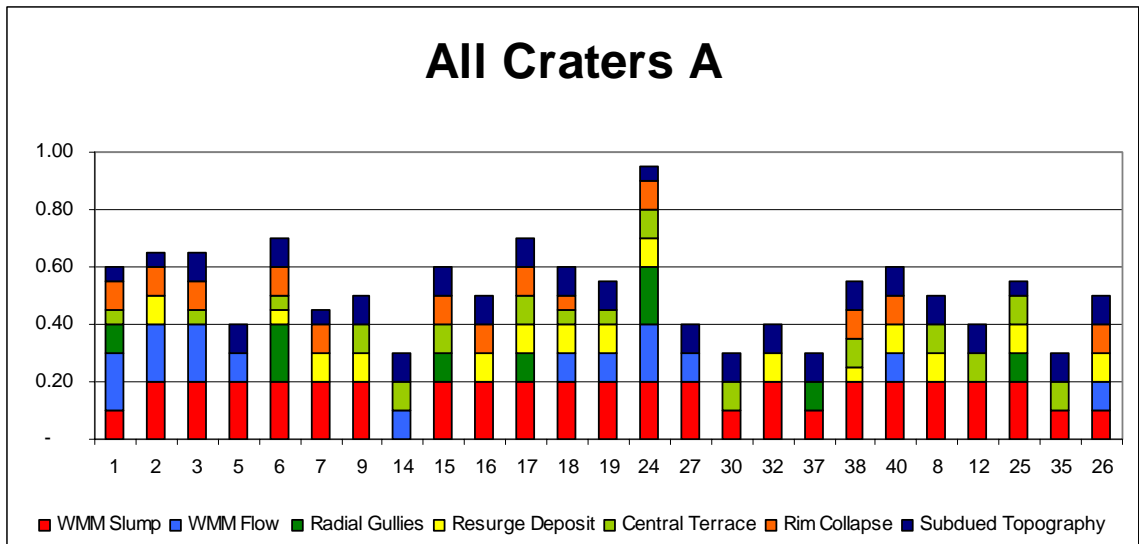


Fig. 26. Stacked columns with individual contributions to the overall rank for the craters in Set A.

## **Results from Set B**

Due to the high resolution of the MOC imagery and smaller field of view (FOV), much of the larger picture and context of the images as they are situated within the craters were lost. The candidates within the initial database are all relatively small, mostly ranging from 10-30 km in diameter. To expand this population, a second search was completed, this time only by looking at the MOLA base map, which has a larger FOV. From the second search, 48 additional potential candidates were identified. Candidate craters from Set B are larger in size and more similar to the potential candidates identified by Ormö et al. (2004).

High-resolution data (both MOC and THEMIS) were downloaded for the new potential sites (165 images in total). Originally, 54 new potential sites were identified, but 4 of these exceed the population size and 2 are highly modified in the recent past, to the point where shallow-marine features could not be clearly distinguished. Recent modification is evident from minimal erosion resulting in sharper surface features. The candidates in the second set were judged by the same system of quantification as those in the first and were again classified based on size. The results are listed in Tables 12, 13 and 14. From Set B there are four small craters ( $D = 10-30$  km), twenty-nine medium craters ( $D = 30-50$  km), and fifteen large craters ( $D = 50-100$  km).

Table 12. Evaluation of characteristics of small shallow-marine crater candidates.

Candidate	Characteristics of Small Candidate Craters							TOTAL
	WMM		RG	RD	CT	RC	ST	
	20% (Slump)	20% (Flow)	20%	10%	10%	10%	10%	
42	0.5	1	0	0	0	1	1	0.5
43	0	0	1	0	0	0	1	0.3
44	0.5	0	0	1	0	1	1	0.4
77	1	0.5	0	0	0	1	1	0.5

WMM – Wet Mass Movement; RG – Radial Gullies; RG – Resurge Deposits; CT – Central Terrace; RC – Rim Collapse; ST – Subdued Topography

Table 13. Evaluation of characteristics of large shallow-marine crater candidates. Exemplary ranking candidates are shown in italics.

Candidate	Characteristics of Large Candidate Craters							TOTAL
	WMM		RG	RD	CT	RC	ST	
	20% (Slump)	20% (Flow)	20%	10%	10%	10%	10%	
47	1	0.5	0	0	1	1	1	0.6
48	0	0.5	0	1	1	1	1	0.5
49	1	0	0	0	0	1	1	0.4
58	<i>0.5</i>	<i>1</i>	<i>0.5</i>	<i>1</i>	<i>1</i>	<i>1</i>	<i>0.5</i>	<i>0.75</i>
60	1	0	0	0	0.5	0	0.5	0.3
64	1	0	1	0	0.5	0	1	0.55
65	1	1	0	0	0	0	1	0.5
69	1	1	0	0	1	0	1	0.6
70	0.5	0.5	0	0	0	0	1	0.3
73	0	0	0	0	0	0	1	0.1
75	1	0	0	0	0.5	0.5	1	0.4
79	0	0	0	0	0	0	1	0.1
81	0.5	0.5	0	0.5	0	0.5	1	0.4
85	0.5	0.5	0	0	0	0.5	1	0.35
92	0	0	0	0	0	1	1	0.2

WMM – Wet Mass Movement; RG – Radial Gullies; RG – Resurge Deposits; CT – Central Terrace; RC – Rim Collapse; ST – Subdued Topography

The largest group of craters in set B is the medium craters. This is expected since the Ormö et al. (2004) craters, that were also medium in size, were the examples after which the search was modeled.

Table 14. Evaluation of characteristics of medium shallow-marine crater candidates. Exemplary ranking candidates are shown in italics.

Candidate	Characteristics of Medium Candidate Craters							TOTAL
	WMM		RG	RD	CT	RC	ST	
	20%	20%	20%	10%	10%	10%	10%	
	(Slump)	(Flow)						
41	0.5	0.5	0	1	1	0.5	1	0.55
45	<i>0.5</i>	<i>1</i>	<i>0</i>	<i>1</i>	<i>1</i>	<i>1</i>	<i>1</i>	<i>0.7</i>
46	1	0	0	0.5	0.5	0	1	0.4
50	1	0	0	0	1	0	1	0.4
51	0.5	1	0	1	1	0	1	0.6
52	1	1	0	1	0.5	0	1	0.65
53	1	0	0	0	0.5	1	1	0.45
54	<i>1</i>	<i>1</i>	<i>0</i>	<i>1</i>	<i>0</i>	<i>1</i>	<i>1</i>	<i>0.7</i>
55	<i>0.5</i>	<i>1</i>	<i>1</i>	<i>0</i>	<i>0</i>	<i>1</i>	<i>1</i>	<i>0.7</i>
56	1	0	0.5	0.5	0.5	1	0.5	0.55
57	1	0	0	0	0	0	1	0.3
61	0	0.5	0.5	0.5	0	1	1	0.45
62	0	0	0	0	0	1	1	0.2
66	<i>1</i>	<i>1</i>	<i>0</i>	<i>1</i>	<i>0</i>	<i>1</i>	<i>1</i>	<i>0.7</i>
68	1	0	0	0	0	1	1	0.4
72	0	0	0	0	0	1	1	0.2
78	0	0	0	0	1	0	1	0.2
80	0	0	0	0	1	0	1	0.2
82	0	0	0	0.5	0	0	1	0.15
83	0	0	0	0.5	0.5	0	1	0.2
84	0	0.5	0	1	0.5	1	1	0.45
86	0	0	0	0.5	0.5	1	1	0.3
87	0	0.5	0.5	1	0.5	1	1	0.55
88	1	0.5	0.5	0	0.5	1	1	0.65
89	0	0	0	0.5	0	0	0.5	0.1
90	0.5	0.5	0.5	1	0	1	1	0.6
91	0	0	0	1	0	1	1	0.3
93	1	0.5	0		1	0	1	0.5
94	0	0	1	0	0	1	1	0.4

*WMM – Wet Mass Movement; RG – Radial Gullies; RG – Resurge Deposits; CT – Central Terrace; RC – Rim Collapse; ST – Subdued Topography*

The global scale of the MOLA imagery and the large sizes of the craters make judging the second set of potential candidates challenging. Therefore, here as before, problems were encountered due to scale. The global scale of the imagery means that the resolution is too low to judge individual features such as slumps and flows. In addition,



the larger the craters, the smaller parts of the crater is covered by a single image. This is a problem because entire features cannot be seen and the context of features is lost. The available imagery does not sufficiently cover the potential sites to assign total scores with certainty, and therefore the average total scores are lower for the second set than for the first. Fig. 27 shows the ratings of all the craters in Set B. Total scores range from 0.1-0.75 with an average of 0.42. The highest ranked crater is Crater 58, with four craters (Crater 45, 54, 55, and 66) following closely. Crater 58 is large, but the other four top-rated craters are all medium in size. Crater 66 falls within both Arabia and Meridiani shorelines, thus the probability that it formed in a marine environment is much higher than for any of the other top-rated candidates in this set. Craters 45, 54, and 55 are all within close proximity of the Arabia shoreline. These three craters are grouped together as typical shallow-marine impact craters. These shallow-marine craters, as well as Craters 58 and 66, are discussed in the next chapter.

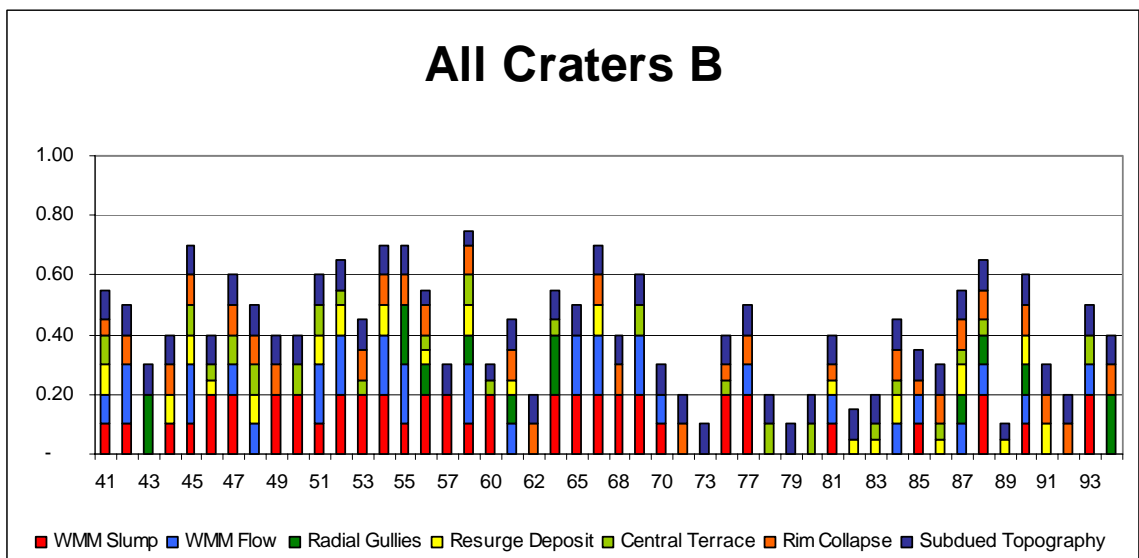


Fig. 27. Stacked columns with individual contributions to the overall rank for the craters in Set B.

## Exemplary candidates

From the 77 craters in the database, nine are chosen for further discussion based on ranking. Craters D, 6, 17, 24, 45, 54, 55, 58, and 66 (see electronic appendix for full database) have total scores of 0.7 or higher, and are the highest-ranking examples in this study. All of these craters exhibit signs of slumping, rim collapse and subdued topography. Furthermore, 77% of these show signs of debris flows and resurge deposits, and 66% have radial gullies and/or central terraces. These data are shown in Figures 28 and 29, where pie charts for each of the craters are drawn. Wet mass movement is divided into two categories: slump (WMM-S) and flow (WMM-F). The sizes of the exemplary candidates range from 20 to 60 km in diameter, with most of the craters falling in the medium (30-50 km diameter) range. Profiles of these craters are included in the next chapter.

Fig. 28. Breakdown of characteristics present in Crater D and legend with color-coded list of features.

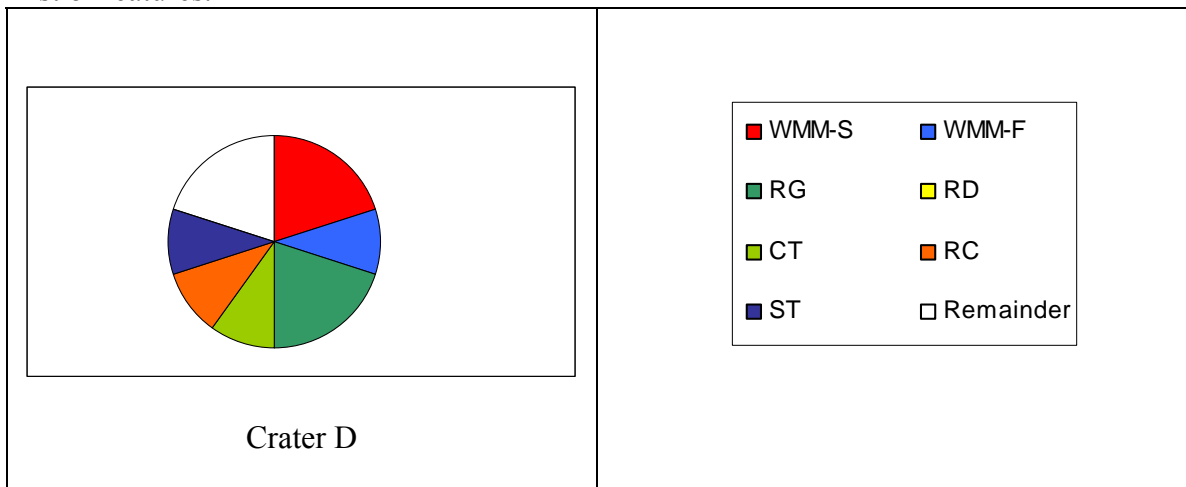
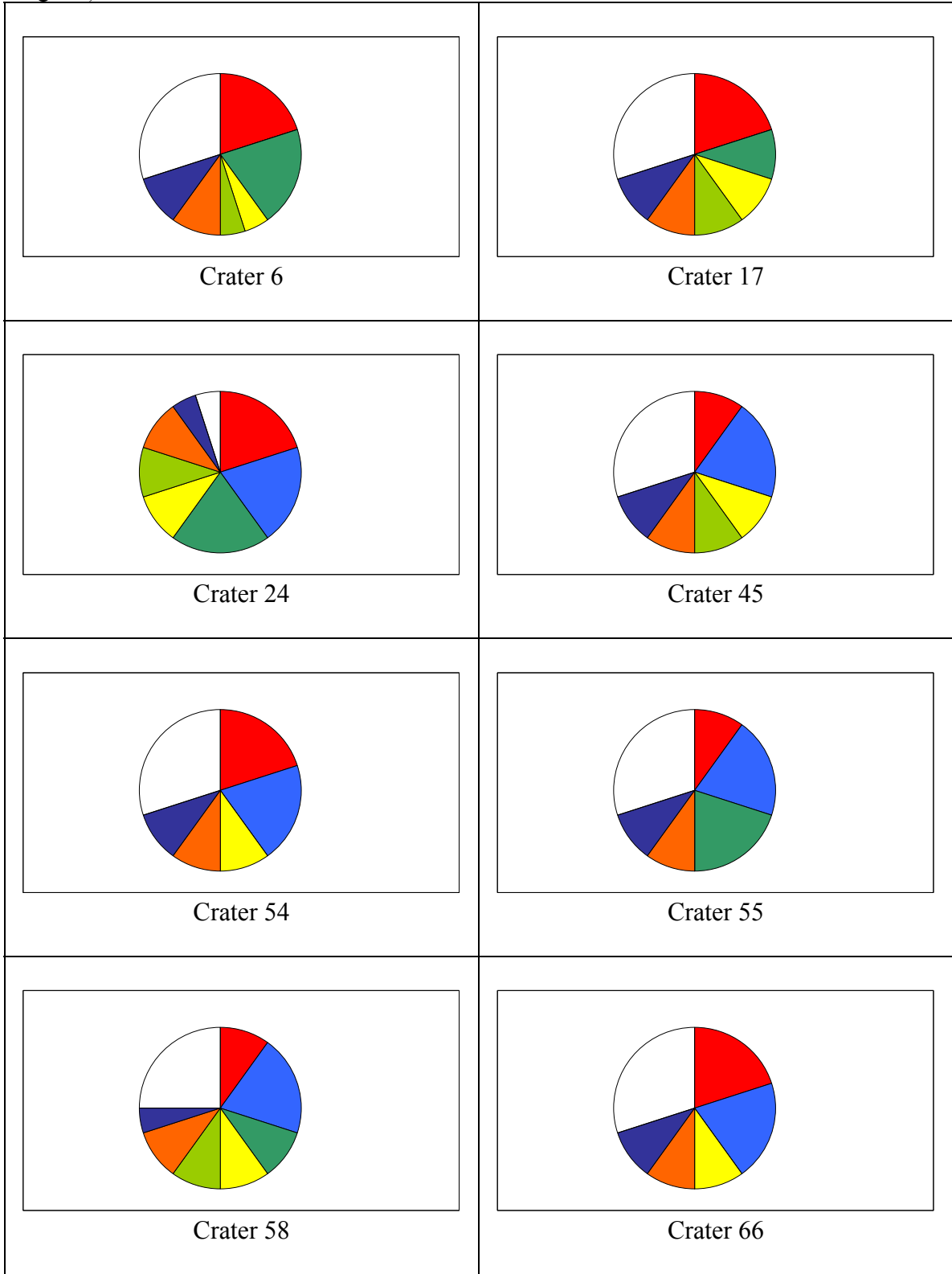


Fig. 29. Breakdown of characteristics present in the exemplary candidates (see legend in Fig. 28).



Physical parameters that were analyzed in this study include diameters, depths, and aspect ratios or depth-diameter relationships. The accuracy with which these parameters are measured depends directly on the resolution of the MOLA data. Depths were measured by subtracting the average height of the crater floor ( $d_c$ ) from the average height of the crater rim ( $d_r$ ). Heights of the surrounding topography ( $d_s$ ) were also measured, and when compared to the rim heights, it seems that there may be some limitations to the use of this parameter. Rim heights are expected to be elevated or at least at the same height as the surrounding topography, yet, in four of the nine crater sites, this is not the case. This could be the result of local variations in topography and an error in the data and/or method is not necessarily implied. Further investigation is needed to accurately assess the depths of the craters in this study. Table 15 lists the depths, diameters, and depth-diameter ratios ( $d/D$  ratios) as measured and calculated for the exemplary candidates. Note that the  $d/D$  ratios range from approximately 0.01 to 0.03, which is much lower than the ratios of 0.07 to 0.09 measured for all craters in Arabia Terra by Barlow (1993).

Table 15. Physical parameters as measured from MOLA data for exemplary candidates. All depths are negative, in other words, below mean surface level (see text for explanation of abbreviations).

Crater	$d_s$ (m)	$d_r$ (m)	$d_c$ (m)	Depth (m)	Diameter (km)	Depth/Diameter ratio
D	3493	3599	3746	147	37	<b>0.0040</b>
6	2217	2325	2874	549	26	<b>0.0211</b>
17	2039	2022	2394	372	23	<b>0.0162</b>
24	3769	3698	4375	677	21	<b>0.0322</b>
45	2242	2152	2783	631	32	<b>0.0197</b>
54	3003	3468	4135	667	36	<b>0.0185</b>
55	3142	3411	4155	744	36	<b>0.0207</b>
58	2098	1902	3051	1148	60	<b>0.0191</b>
66	3362	3642	4387	745	32	<b>0.0233</b>

Using the depth-diameter relationships defined by Howenstein (2006) and Garvin et al. (2000), one can estimate the depth by substituting the diameter. For the relationship defined by Howenstein (2006),  $d = 0.61D^{0.33}$ , the estimated depths (A; see Table 16) are much higher than the depths estimated (B; see Table 16) with  $d = 0.19D^{0.55}$ , as defined by Garvin et al. (2000) for non-polar craters. Estimated depths for the exemplary candidates are listed in Table 16. Garvin et al.'s (2000) relationship (B) more closely predicts the depths measured in this study. The factors with which the estimated depths differ from the measured depths are also listed in Table 16. Crater D stands out as potentially anomalous with nearly an order of magnitude difference between the measured value and the estimated value. The rest of the depths vary consistently with a factor around two, possibly explained by faster rates of infilling for craters in shallow-marine environments.

Table 16. Depths as measured from MOLA data for exemplary candidates and estimated depths as calculated from depth-diameter relationships in literature (Garvin 2000; Howenstein 2006). Factors of difference (see text) are given for each estimation.

Crater	Depth (m)	Estimated depth A (m)	Factor	Estimated depth B (m)	Factor
D	147	2008	12	1384	9
6	549	1788	3	1140	2
17	372	1717	5	1066	3
24	677	1666	3	1014	2
45	631	1914	3	1278	2
54	667	1990	3	1364	2
55	744	1990	2	1364	2
58	1148	2356	2	1806	2
66	745	1914	2	1278	2

The results of this study are included in the format of spreadsheets on a CD-ROM that accompanies this thesis. All images and figures are also included.

## INTERPRETATIONS

My shallow-marine impact crater candidate database contains the four craters identified by Ormö et al. (2004), 25 craters identified in Set A, and 48 craters identified in Set B. From this database, a few exemplary candidates were chosen and their locations relative to the proposed shorelines are shown in Fig. 30. In this figure, the blue line represents the location of the Deuteronilus shoreline, and the yellow line represents the location of the Arabia shoreline. The Meridiani shoreline runs further southeast and all craters fall within its boundaries. The low depth-diameter ( $d/D$ ) ratios of the exemplary candidates could be an indication of age. Older craters have rims that have been more eroded and crater shapes that are shallower due to sediment infilling (Reiss et al. 2006). The  $d/D$  ratios (refer back to table 15 in Results) for the exemplary candidates are lower than expected, yet this can be interpreted as a result of the old age (Noachian) of the craters in the population of potential candidates. Furthermore, resurge deposits and post-impact sedimentation from the water column would fill the crater faster than craters on land, and could therefore be responsible for the low crater depths. Estimated depths vary greatly from the measured depths (refer back to Table 16 in Results), possibly due to the difference in crater populations. Garvin et al. (2000) considered all non-polar craters and Howenstein (2006) considered all large craters. The exemplary candidates would therefore be shallower than average craters on the surface.

The exemplary candidates are divided into three classes based on total scores and locations. Type I includes well-developed, mostly medium-sized examples; type II includes typical small and medium examples; and type III includes other large potential candidates.

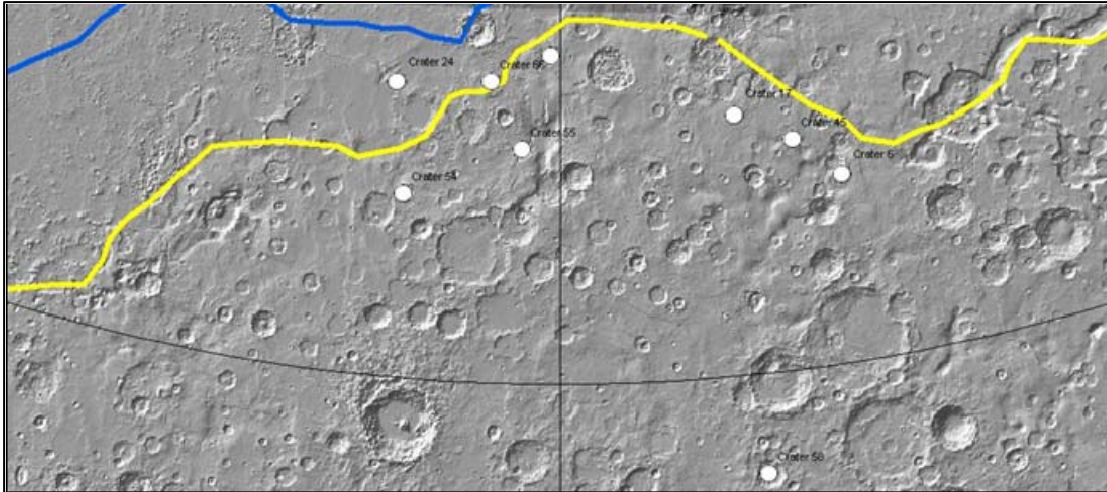


Fig. 30. Locations of exemplary candidates on MOLA topographic raster image.

## Type I candidates

### *Crater D*

Ormö et al. (2004) originally identified Crater D as a potential marine crater, based on certain morphological features observed by looking at Viking imagery. Crater D is located at roughly 39.00°N and 001.00°W and well within the Meridiani shoreline as defined by Edgett and Parker (1997) and Fairén et al. (2003).

This candidate is more closely evaluated with the use of several MOC images. The MOC images are draped over the MOLA base map in ArcGIS to create a layered, composite, context images with high-resolution details (Fig. 31).

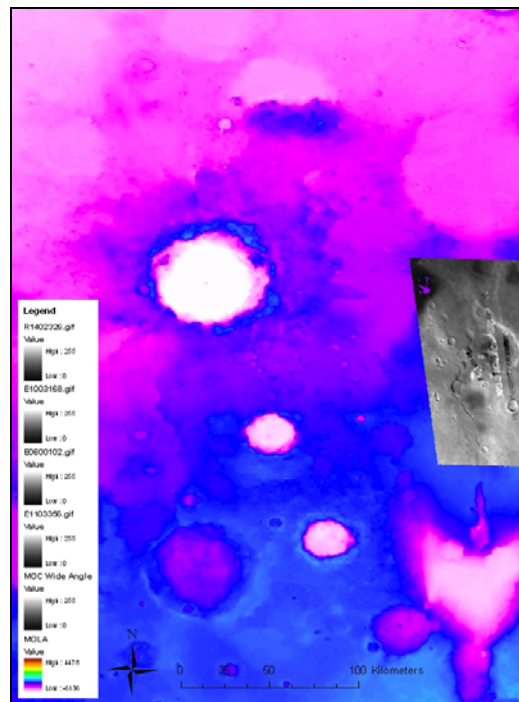


Fig. 31. Composite image for Crater D with MOLA base map and MOC wide and narrow-angle images as high-resolution overlays.



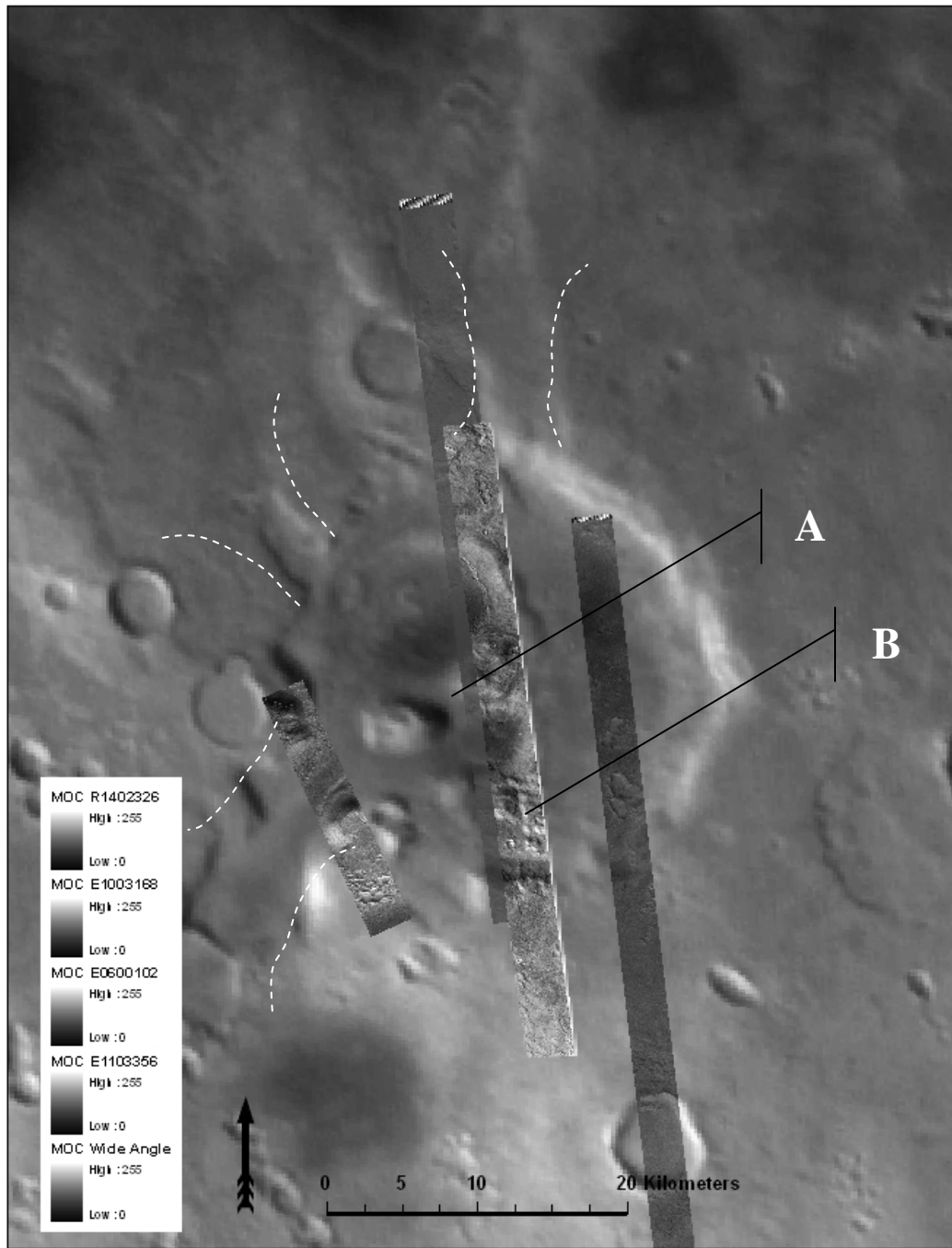


Fig. 32. A close-up of Fig. 30 showing MOC narrow angle image overlay in more detail. Radial gullies are indicated by white dashed lines and features labeled A-B are discussed in text.

Of the potential marine craters suggested by Ormö et al. (2004), Crater D has the highest total score of 0.8. In Fig. 32, the radial gullies are the most remarkable features of this candidate crater (indicated by white dashed lines). One large gully enters the crater from the southwest and is likely responsible for the large resurge deposit (A) located in the southwestern section of the crater. Features of wet mass movement are also evident in both the form of slumping of the crater wall as well as the flow of some debris flows, particularly in the southern part of the rim (B).

Crater D is roughly 37 km in diameter and hence falls in the medium class (30-50 km diameter). The depths between the surrounding topography and the bottom of the crater floor vary greatly, but average around 200 m. A north-south profile of Crater D is shown in Fig. 33. The  $d/D$  ratio was calculated to be 0.004. Even though low values are expected for marine craters on Mars, this value could be anomalously low considering that the average  $d/D$  ratio for the exemplary candidates is 0.02. As mentioned earlier in this chapter, low  $d/D$  ratios are indicative of old age and large amounts of sedimentation. Impacts into marine environments should exhibit more sediment infilling than impacts on land. Resurge and tsunami deposits could contribute largely to this rapid infilling; beyond regular fast rates of burial.

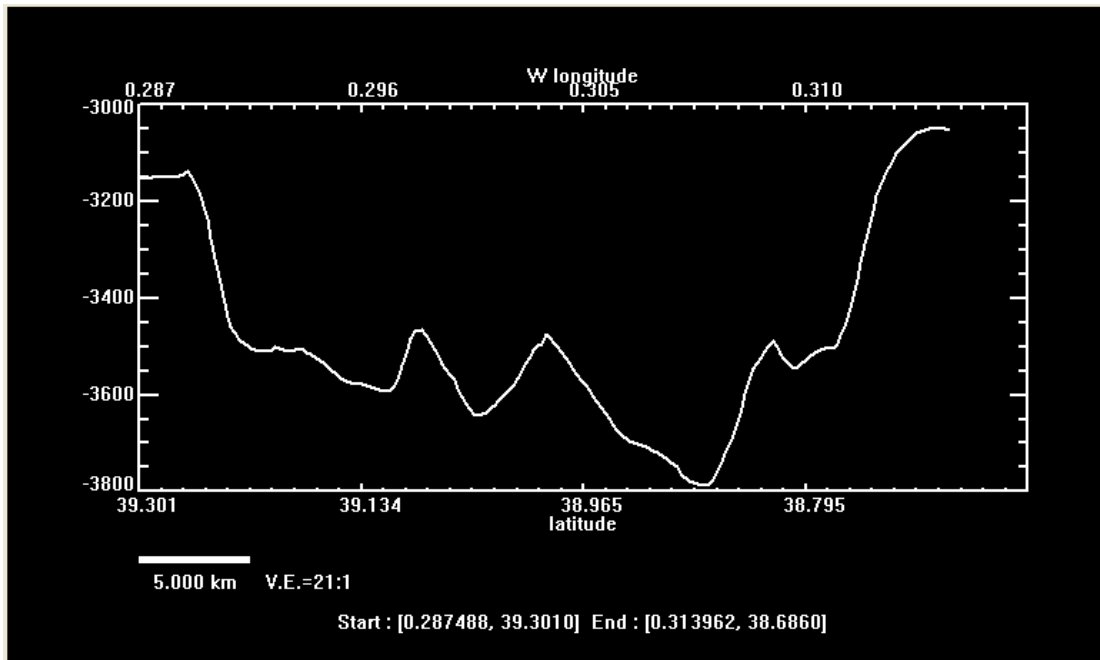


Fig. 33. Profile view of Crater D showing varying depth (in km) with variation in latitude (in degrees) from north (left) to south (right). Vertical exaggeration is 21:1.

From the profile shown in Fig. 33 one can see the terraced central uplift and what seems to be a central ring. The subdued topography of the crater walls is clear on the northern rim. Also visible in the southern half of the profile is a terraced resurge unit, likely to have been deposited by a large gully entering from the southwest.

## Crater 24

Crater 24 is located at roughly 38.39°N and 006.02°W, and well within both the Arabia and Meridiani shorelines. MOC images are draped over THEMIS images, which in turn are overlaid on top of the MOLA base map to create a layered, composite, context images with high-resolution details (Fig. 34).

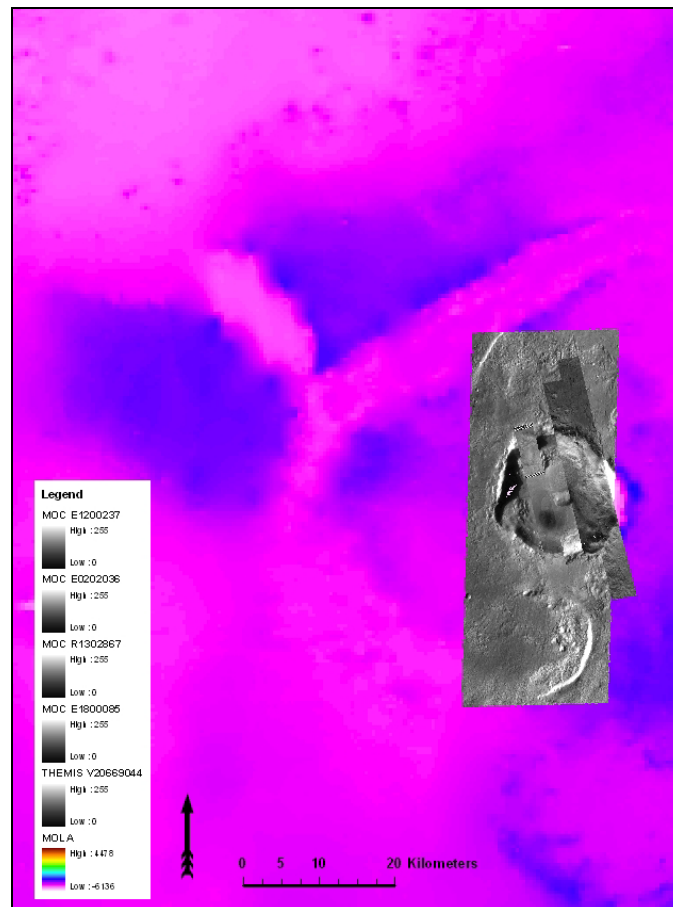


Fig. 34. Composite image for Crater 24 with MOLA base map, THEMIS image and MOC narrow-angle images as high-resolution overlays.

Crater 24 has a total score of 0.95 – the highest ranking of all craters in the database. This crater exhibits all the characteristics for a shallow-marine candidate, except that the topography is not as subdued as expected. This casts some doubt on the age of this crater. Thus, even though the confidence rating is high, it is arguable that this crater did in fact form during the Noachian. However, in terms of morphology, this candidate exhibits some good examples of the characteristics that are thought to be present in shallow-marine impact craters (see Fig. 35). Deposits that have a possible resurge origin are the most remarkable features of this candidate crater (A). Gullies seem to enter the crater from the northwest as well as the north northeast (shown in white dashed lines) and are likely responsible for the large resurge deposits located in the both these areas. Large amounts of slumping can be seen around the crater rim (B), and in some places the rim has started to collapse (D). Debris flows dominate the eastern half of the crater (E). Some of the flows, particularly in the south southeast, are much younger than the crater itself and are the result of subsequent draining into the crater. Large valleys can be seen in the south southeast and these should not be confused with the flows related to the impact such as those further north. A central terrace is present in this crater (C), but large amounts of post-impact sediments seem to cover most of the intra-crater terrain.

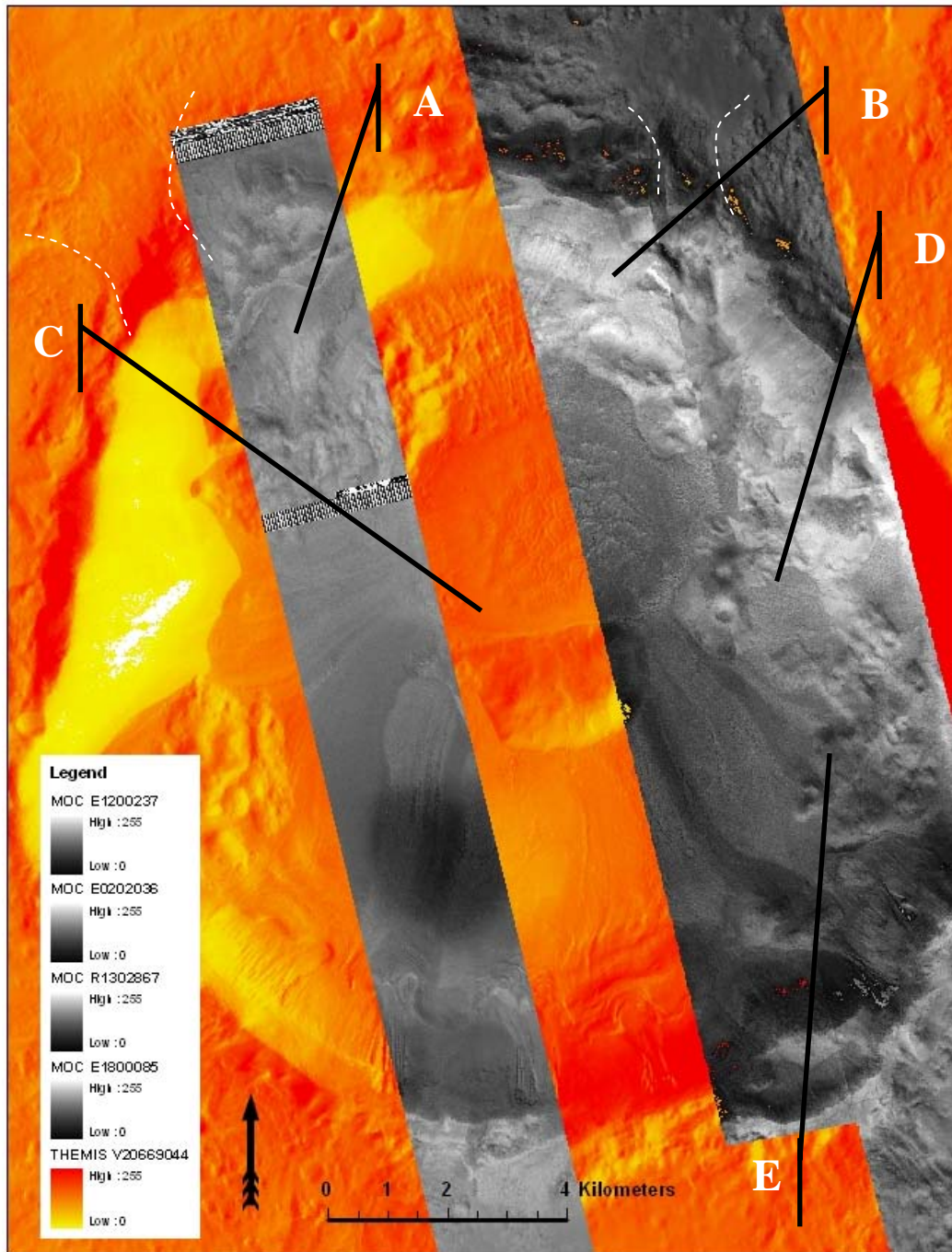


Fig. 35. A close-up of Fig. 34 showing MOC narrow angle image overlay in more detail. Radial gullies are indicated by white dashed lines and features labeled A-E are discussed in text.

Crater 24 is roughly 21 km in diameter (the smallest of the exemplary candidates) and hence falls in the small class (10-30 km diameter). A north-south profile of Crater 24 is shown in Fig. 36. From the profile shown in Fig. 36 one can see that this crater is fairly deep and that the rim is still somewhat elevated above the surrounding areas. A thick sedimentary unit is visible in the southern half of the profile, and though it is possibly a resurge unit resulting from the gully to the south southwest, it is impossible to exclude post-impact sedimentation from younger drainage systems. This resurge unit may be responsible for the low  $d/D$  ratio (0.03) calculated for this crater. Regardless of the fact the  $d/D$  ratio is low compared to that of other craters on Mars, it is still the highest  $d/D$  ratio measured in this study, indicating that this crater may be younger than the other exemplary craters.

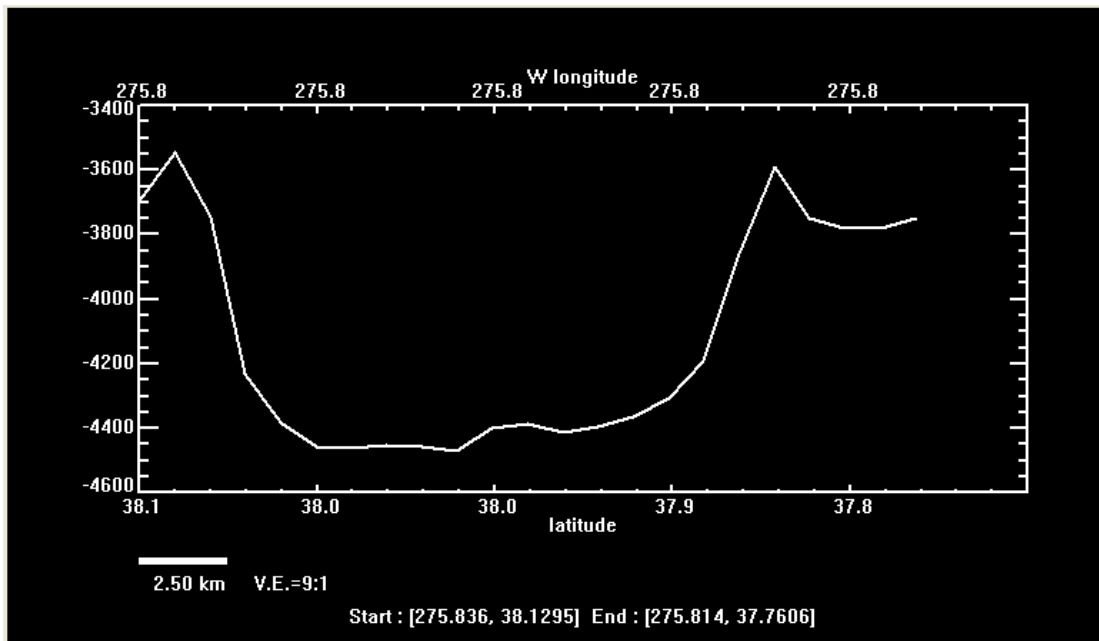


Fig. 36. Profile view of Crater 24 showing varying depth (in km) with variation in latitude (in degrees) from north to south. Vertical exaggeration is 9:1.

### *Crater 66*

Crater 66 is located at roughly 38.21°N and 002.48°W, and lies within both Arabia and Meridiani shorelines. THEMIS images are draped over the MOLA base map to create a layered image with high-resolution details (Fig. 37).

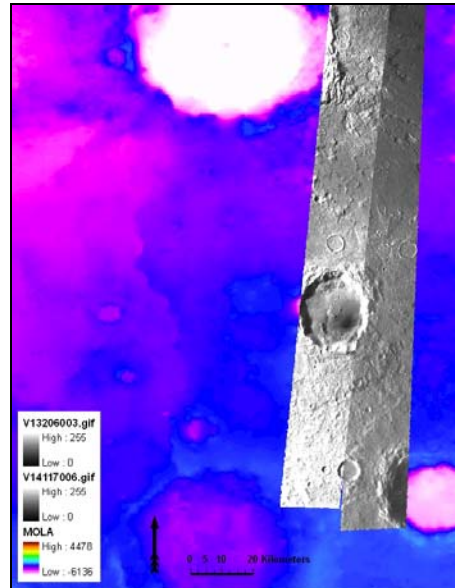


Fig. 37. Composite image for Crater 66 with MOLA base map and THEMIS images as high-resolution overlays.

Crater 66 has a total score of 0.7. Particularly striking in Fig. 38, are the features of wet mass movement. Both slumps and flows are present in this crater, particularly near the southern and northern parts of the crater (A and B). This is in accord with the general location of the crater in relation to the shoreline. According to the paleogeography, the resurge waters would have entered the crater from the north and potentially affected the northern walls more severely than the eastern or western walls. The crater's wall has collapsed in the southernmost parts of the crater (C).



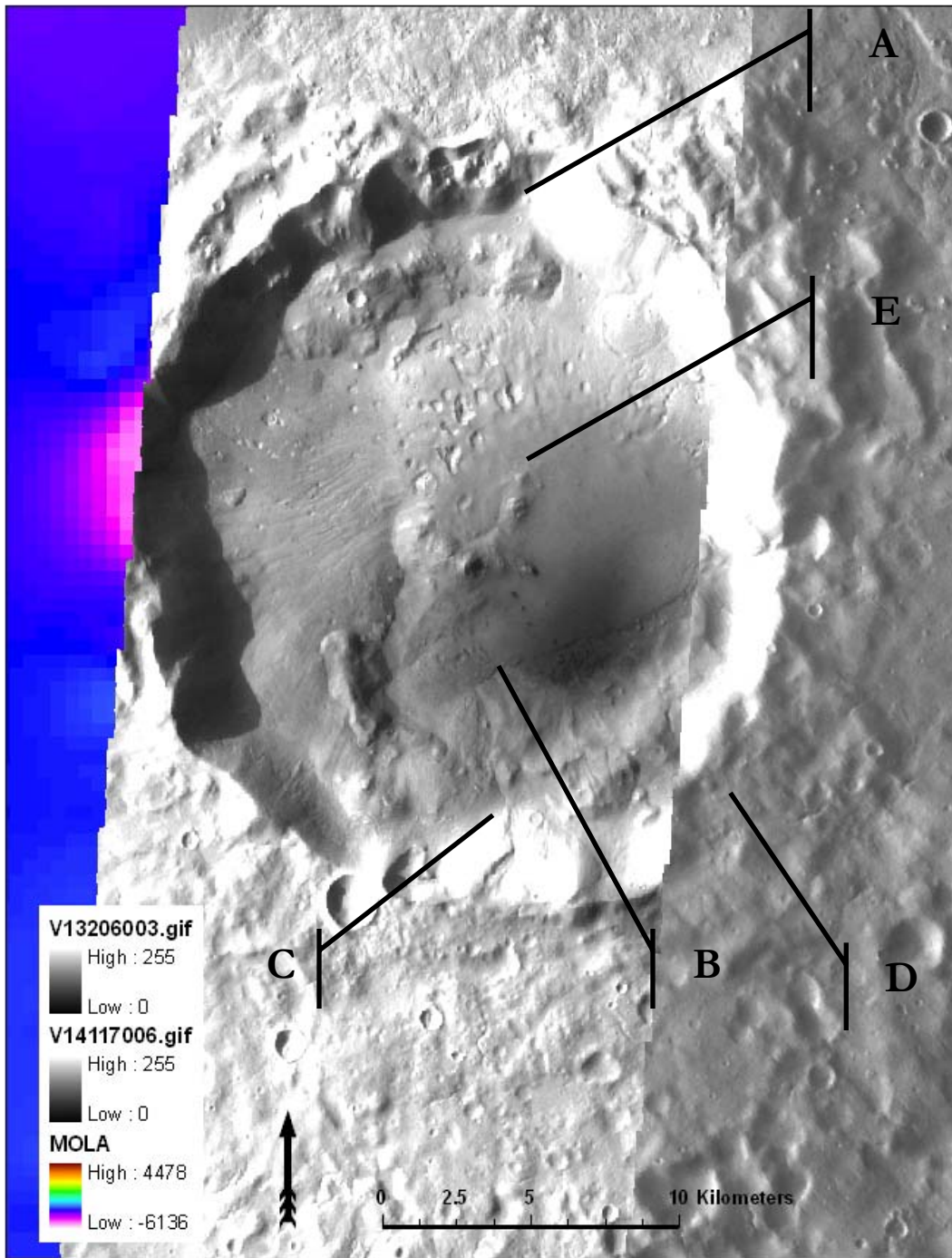


Fig. 38. A close-up of Fig. 36 showing THEMIS image overlay in detail. Features labeled A-E are discussed in the text.

Topography in and around Crater 66 is subdued and the rim is hardly elevated above average surface height (see D in Fig. 38). The central peak ring seem also to have been affected by resurge waters by having the entire northern half obliterated (E).

Crater 66 is roughly 32 km in diameter and therefore falls in the medium class (30-50 km diameter). Crater 66 has a low d/D ratio (0.02), which is average for this population of craters. A north-south profile of Crater 66 is shown in Fig. 39.

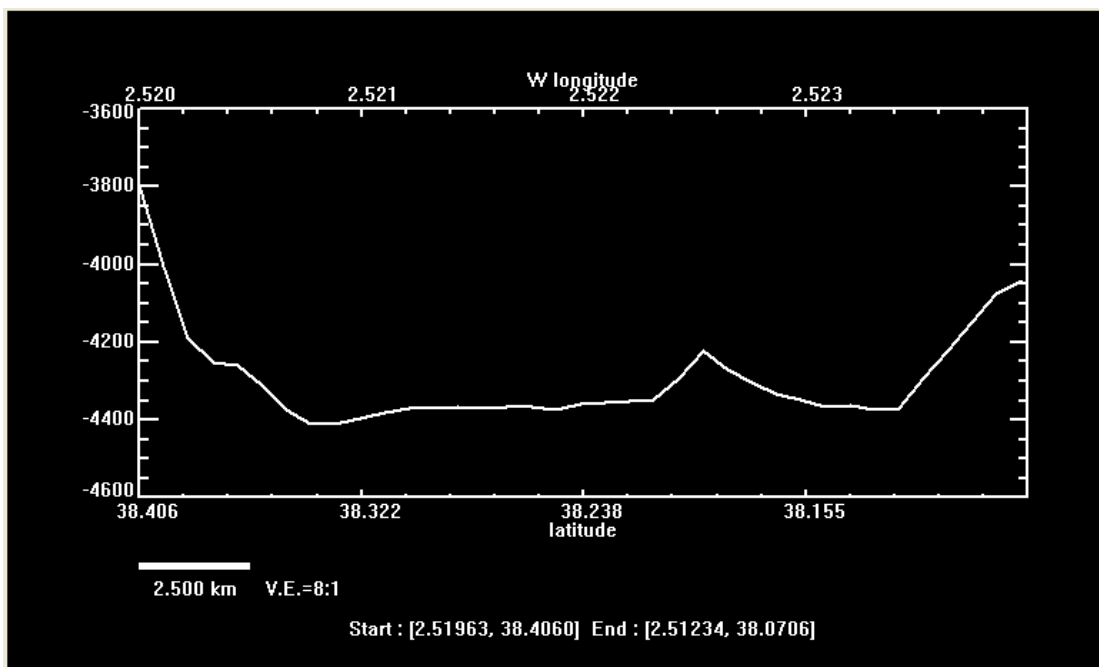


Fig. 39. Profile view of Crater 66 showing varying depth (in km) with variation in latitude (in degrees) from north to south. Vertical exaggeration is 8:1.

Slumping is evident from the profile shown in Fig. 39, particularly in the northern parts of this crater. One can clearly see a topographic high located in the southern half, but this uplift is only the southern part of the central peak ring terrace. The resurge waters have likely completely eroded the northern part of the central peak ring. The

sedimentary deposit directly north of this collapsed inner ring probably formed as a result of water resurge from the north, leaving blocks of rim and other material on the crater floor. The location of the gully that may have dumped this sediment is uncertain, but the water may have been too shallow to allow gully formation. The depths between the surrounding topography and the bottom of the crater floor vary between 300 m in the south to 600 m in the north. This supports the observation of structural rim failure and subdued topography in the southern crater wall.

## Type II candidates

### *Crater 6*

Crater 6 is located at roughly 35.34°N and 350.75°W. MOC images are draped over THEMIS images, which in turn are overlaid on top of the MOLA base map to create a layered, composite, context images with high-resolution details (Fig. 40).

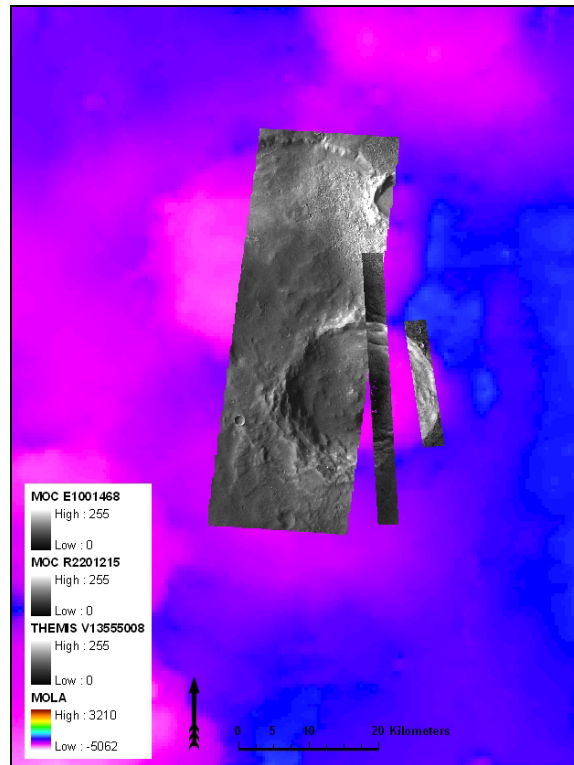


Fig. 40. Composite image for Crater 6 with MOLA base map, THEMIS image, and MOC narrow-angle images as high-resolution overlays.

Crater 6 has a total score of 0.7. As seen in Fig. 41, slumping is evident all around the rim (A), but no debris flows are present. The central terrace is not well developed and may be covered in post impact sediments. A few small gullies are present (shown with white dashed lines), but they are not distinct and possibly even post-impact.

It is mainly the rim collapse sedimentary deposit (B) in the northwest corner of the structure that indicates some resurgence.

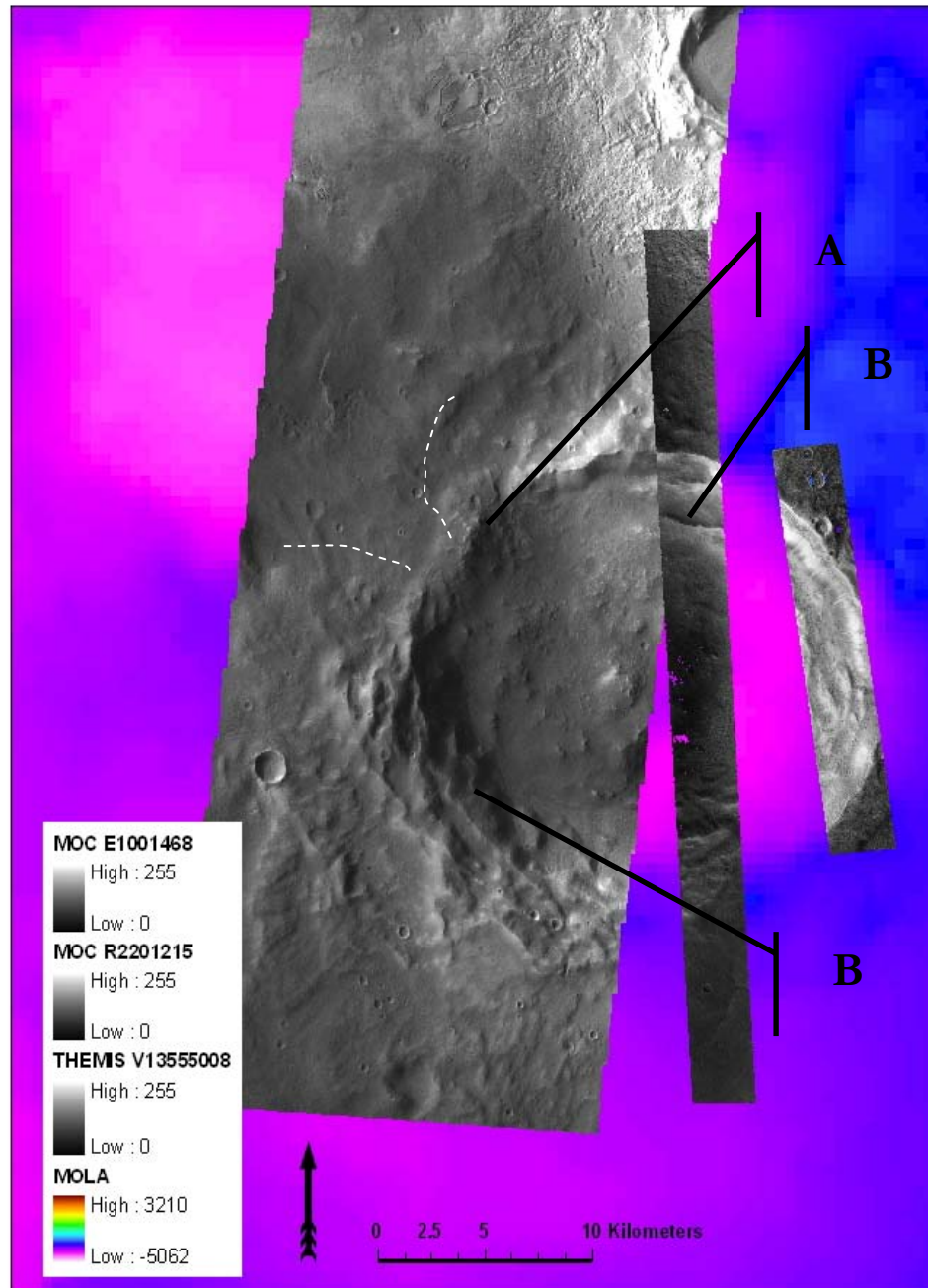


Fig. 41. Close-up of Fig. 40 showing MOC and THEMIS image overlays in detail. Features labeled A-B are discussed in the text.

Crater 6 has a diameter of approximately 26 km and falls in the small class (10-30 km diameter). The  $d/D$  ratio for Crater 6 is approximately 0.02; around average again for the exemplary candidates. A north-south profile of Crater 6 is shown in Fig. 42.

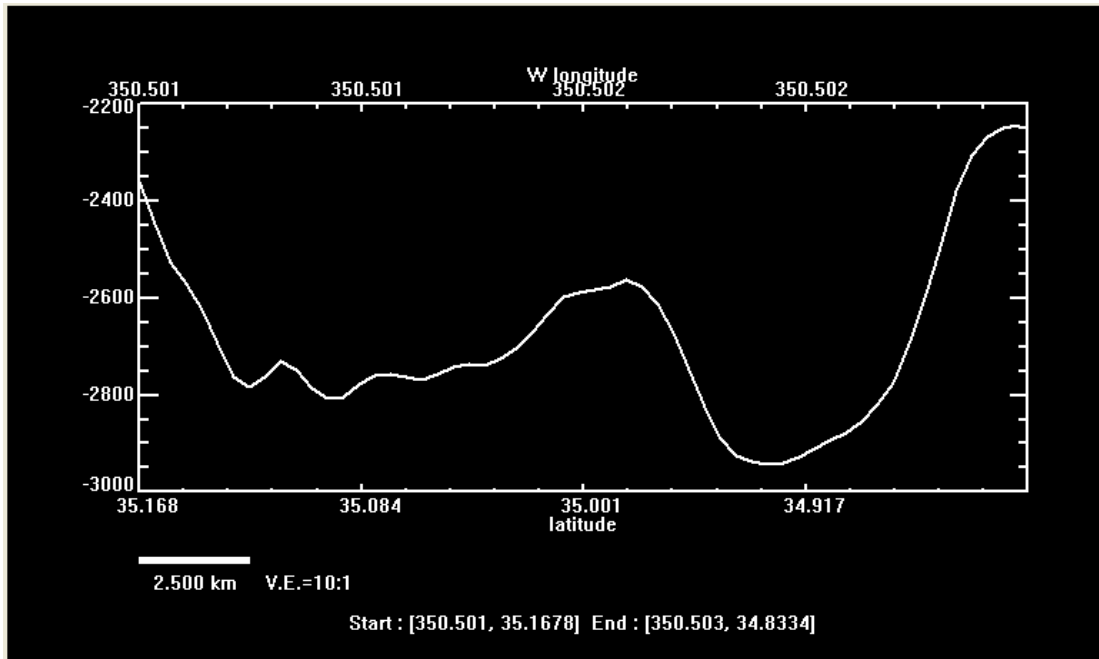


Fig. 42. Profile view of Crater 6 showing varying depth (in km) with variation in latitude (in degrees) from north to south. Vertical exaggeration is 10:1.

From the profile shown in Fig. 42, the terraced central uplift is the most prominent feature. Furthermore, large slumps are present in the northern half of the structure. The subdued topography of the crater walls is clear on the southern rim.

### Crater 17

Crater 17 is located at approximately 37.43°N and 354.30°W. MOC images are draped over THEMIS images, and both sets of images are draped over the MOLA base map to create a layered, context images with high-resolution details (Fig. 43).

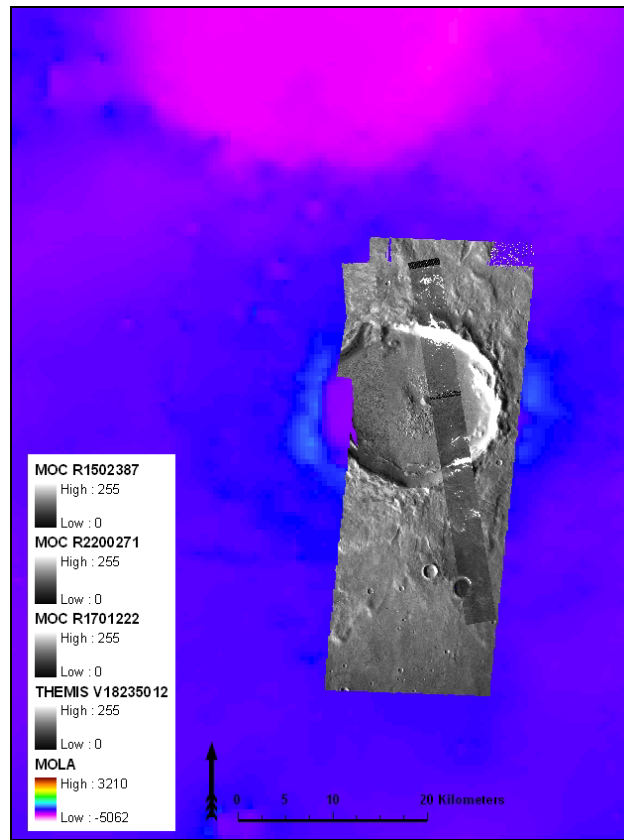


Fig. 43. Composite image for Crater 17 with MOLA base map, THEMIS image, and MOC narrow-angle images as high-resolution overlays.

Crater 17 has a total score of 0.7. This crater has been filled with post-impact sediments, but some of the characteristic features are still present in this structure. Fig. 44 shows the large, shallow, filled crater. Most of the central terrace is covered in sediments, and resurge sediments are present just south of the northern rim (A). Topography is subdued and the crater rim is not elevated above the surrounding

topography (B). The rim is breached in more than one place, and the breach in the north is possibly responsible for the sedimentary resurge deposit just south of the rim (A). The remains of what might have been a gully entering the crater from the north can also be seen in this area (Fig. 44). Features of wet mass movement are also evident in the form of slumping of the crater wall, evident particularly in the east.



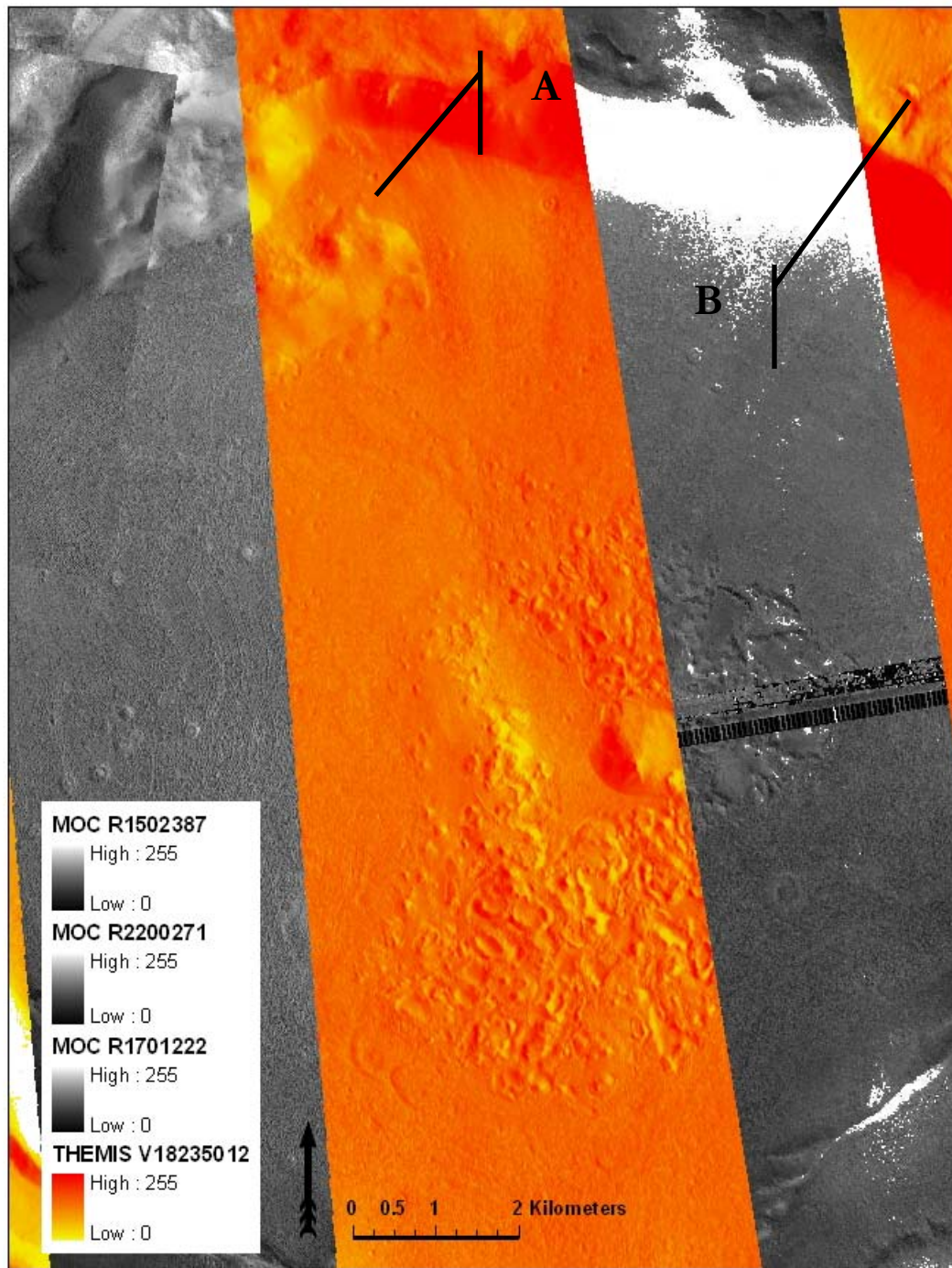


Fig. 44. Close-up of Fig. 43 showing MOC image overlay over THEMIS. Features labeled A and B are discussed in the text.

Crater 17 is roughly 23 km in diameter and falls in the small class (10-30 km diameter) along with Crater 6. Furthermore, similar to Crater 6, the d/D ratio for Crater 17 is approximately 0.02. Fig. 45 shows a north-south profile of Crater 17.

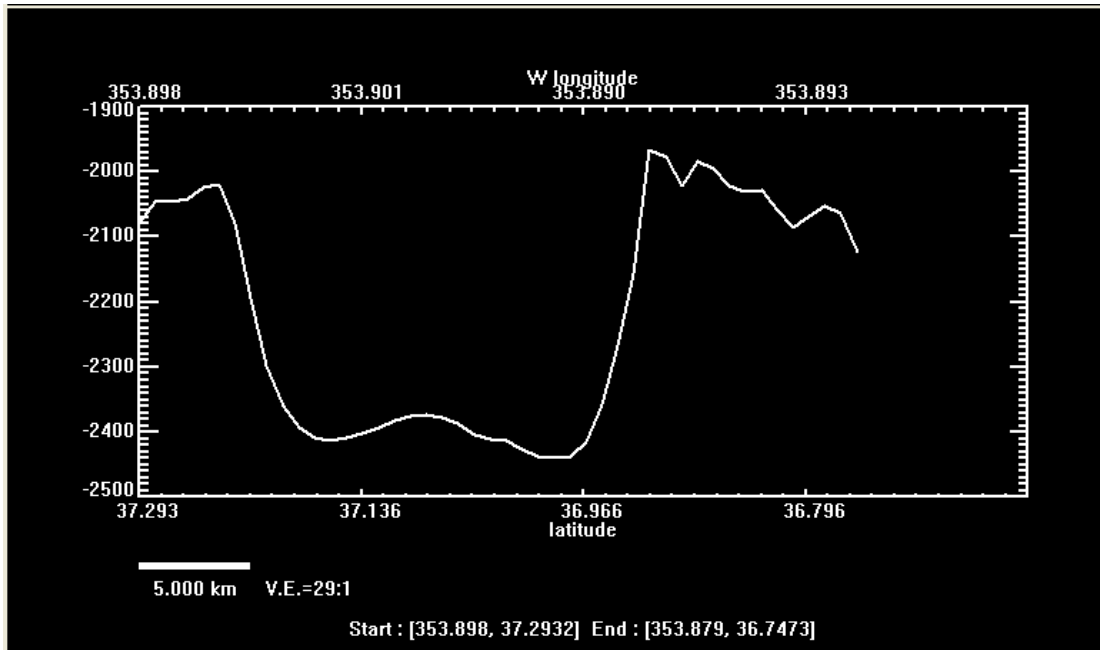


Fig. 45. Profile view of Crater 17 showing varying depth (in km) with variation in latitude (in degrees) from north to south. Vertical exaggeration is 29:1.

From the profile shown above the subdued topography of the crater walls is clear on both the northern and southern rims. Some deposits are evident in the center of the crater. Judging by the appearance of the crater floor in the images, these deposits are more likely the result of post-impact sedimentary fill than syn-impact resurge.

### Crater 45

Crater 45 is located at roughly 36.18°N and 351.96°W. THEMIS images are draped over the MOLA base map to create a layered, high-resolution image (Fig. 46).

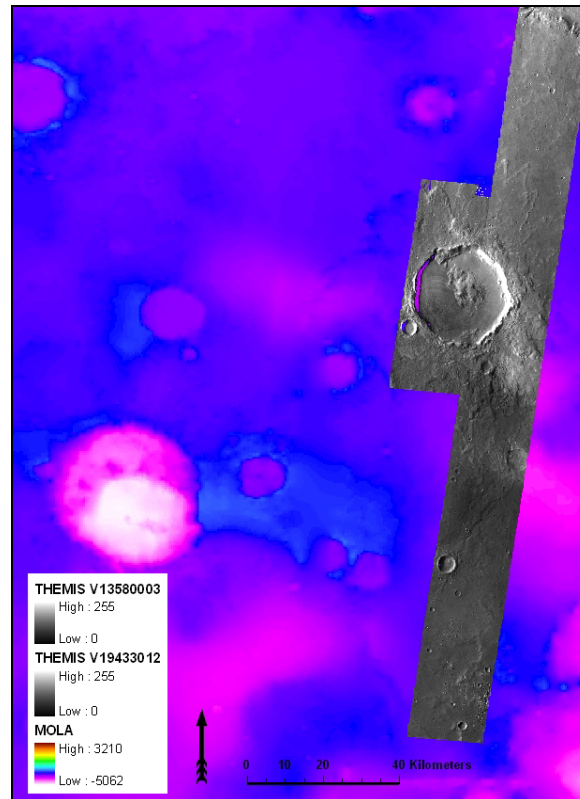


Fig. 46. Composite image for Crater 45 with MOLA base map and THEMIS images as high-resolution overlays.

Crater 45 has a total score of 0.7. The slumped resurged deposits (A) visible in the northern and southern parts of the structure (Fig. 47) could be post-impact. The smooth appearance of the crater floor clearly indicates a second, more recent sedimentation event. This could be from drainage into the crater basin. No drainage channels are visible, which suggests that the sedimentation might be from water rising from below the structure. If sediments are fluidized at a later stage from below, slumping

and flowing of the rim wall would be expected. It is therefore uncertain if the sediments were deposited at the time of impact by a resurge event. However, it seems plausible that this deposit could have been related to resurge, based on its relative location. The proposed ocean would lie north of the crater, resulting in forceful waves coming from the northerly direction. Deposits in the center of the crater (B) may or may not be impact-related. Relative spatial location suggests some link to the possible resurge deposit in the north. The crater is not elevated above the surrounding topography, indicating that either no rim formed initially, or that the rim has been modified and eroded, possibly through fluids related to resurge activity and/or long-standing water covering the crater. The breach in southern part of the rim could be part of rim collapse due to sediment saturation (C).

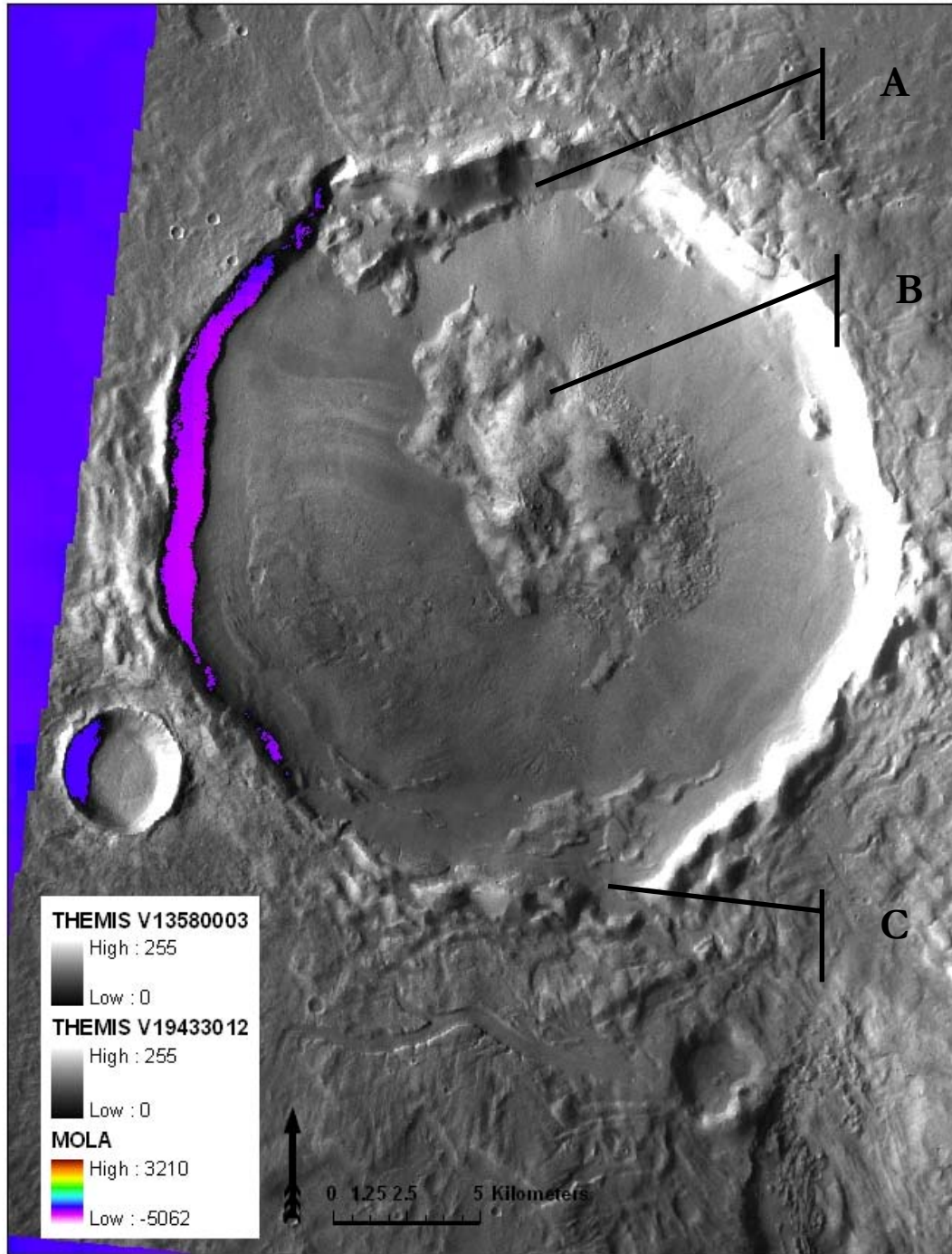


Fig. 47. Close-up of Fig. 46 showing THEMIS image overlay. Features labeled A-C are discussed above.

Crater 45 is roughly 31.5 km in diameter and hence falls in the medium class (30-50 km diameter). Fig. 48 shows a north-south profile of Crater 45. It is clear that a resurge or slump deposit is located in the northern parts of the crater. Judging by the visual images, the spike in the southern wall is not representative of the whole rim.

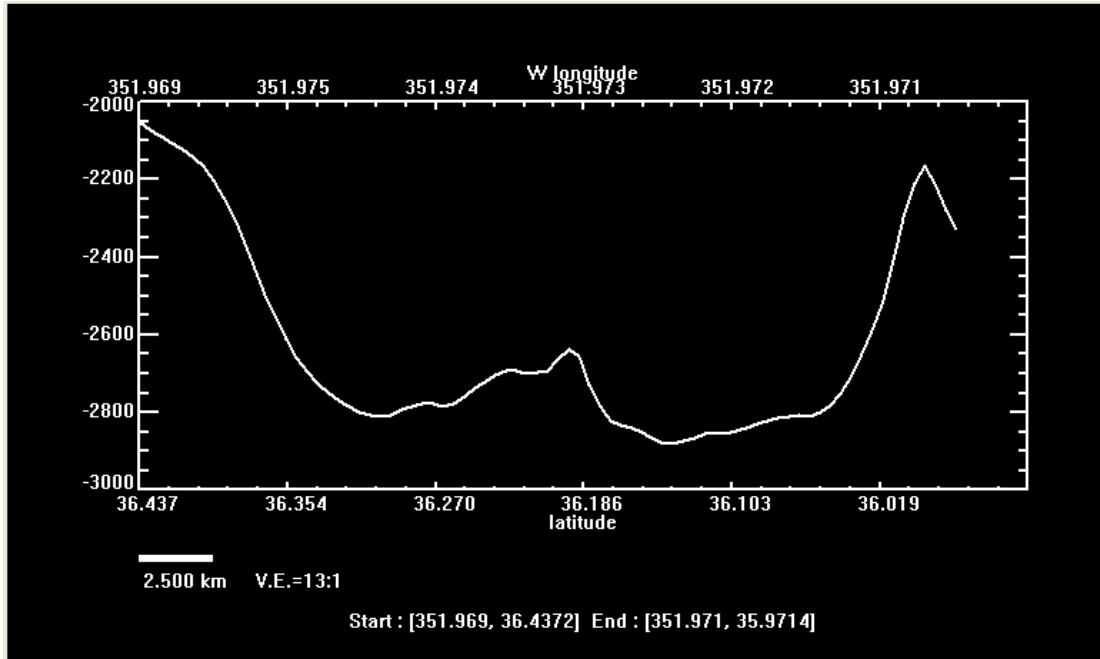


Fig. 48. Profile view of Crater 45 from north to south. Vertical exaggeration is 13:1.

### Crater 54

Crater 54 is located at roughly 34.94°N and 005.24°W. One THEMIS image is draped over the MOLA base map to create a layered image with selected parts in high resolution (Fig. 49).

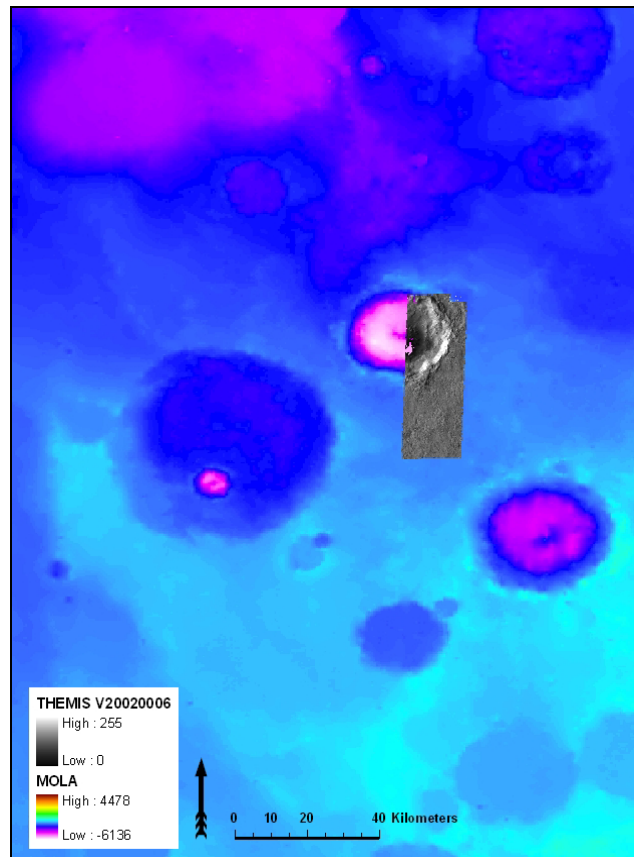


Fig. 49. Composite image for Crater 54 with MOLA base map THEMIS image as a high-resolution overlay.

Crater 54 has a total score of 0.7. Only one high resolution THEMIS image could be draped over the MOLA topography, but from the composite image in Fig. 50, numerous features could be identified. Features of wet mass movement are evident in both the form of slumping of the crater wall (A) as well as the flow of some debris flows.

A large well-developed debris flow tongue (B) is visible in the north northeast of the crater, and numerous smaller flows are also visible in the THEMIS images. The crater rim is not elevated above the topography, and in some places, the rim has collapsed (C). No gullies are observed in this crater, and no central terrace is evident. Some structural blocks are found on the crater floor (D), possibly deposited as rim material being washed into the crater as the water returns.



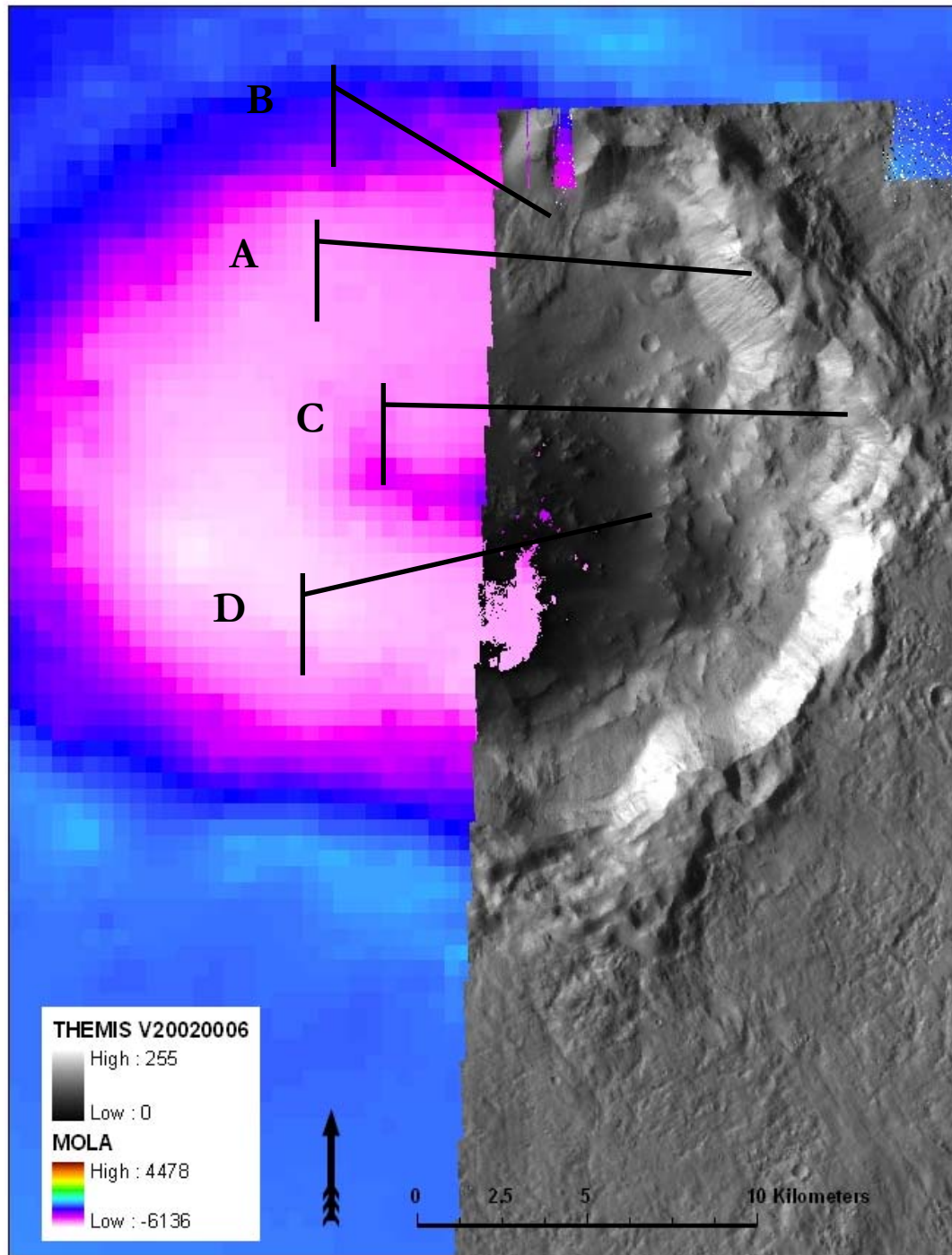


Fig. 50. Close-up of Fig. 49 showing THEMIS image overlay. Features labeled A-D are discussed in the text above.

Crater 54 is 36 km in diameter (very similar to Crater D) and hence falls in the medium class (30-50 km diameter). It is also close to Crater D in relative location (Fig. 58). A north-south profile of this crater is drawn in Fig. 51. The depths between the surrounding topography and the bottom of the crater floor vary greatly, with a maximum of 1500m. The central uplift and the subdued topography are the two features that are most evident from the profile. Some slumping is apparent in the southern rim area and sediment fills the northern half of the crater, possibly induced by debris flow.

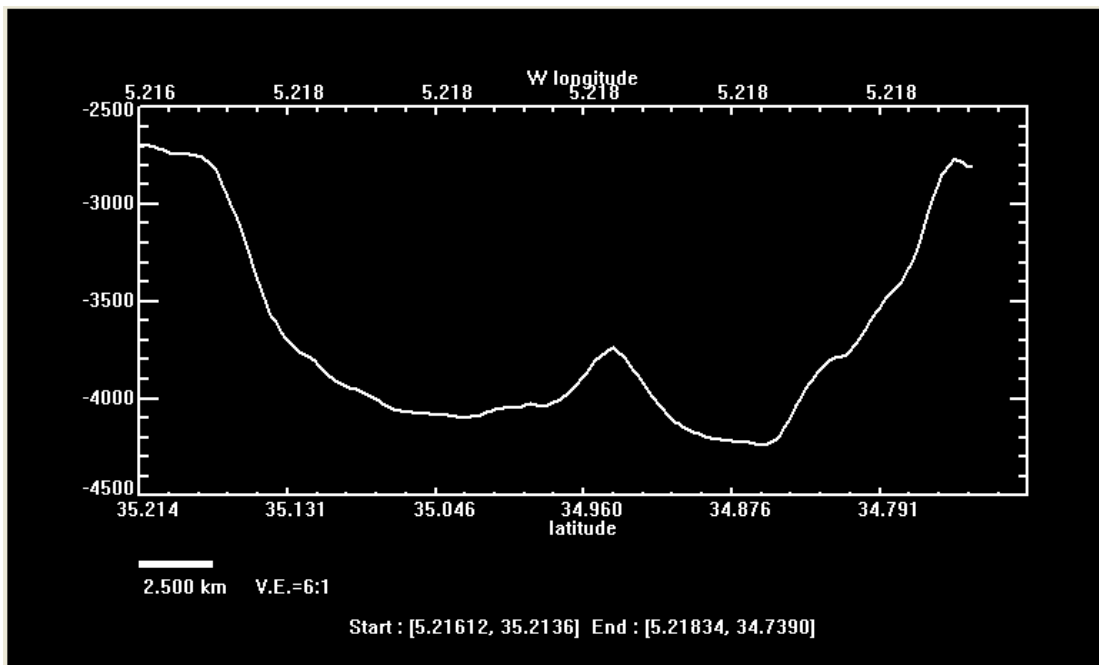


Fig. 51. Profile view of Crater 54 from north to south. Vertical exaggeration is 6:1.

*Crater 55*

Crater 55 is located at approximately 36.37°N and 001.29°W. MOC images are overlaid on top of the MOLA base map to create a layered image with selected parts in high resolution (Fig. 52).

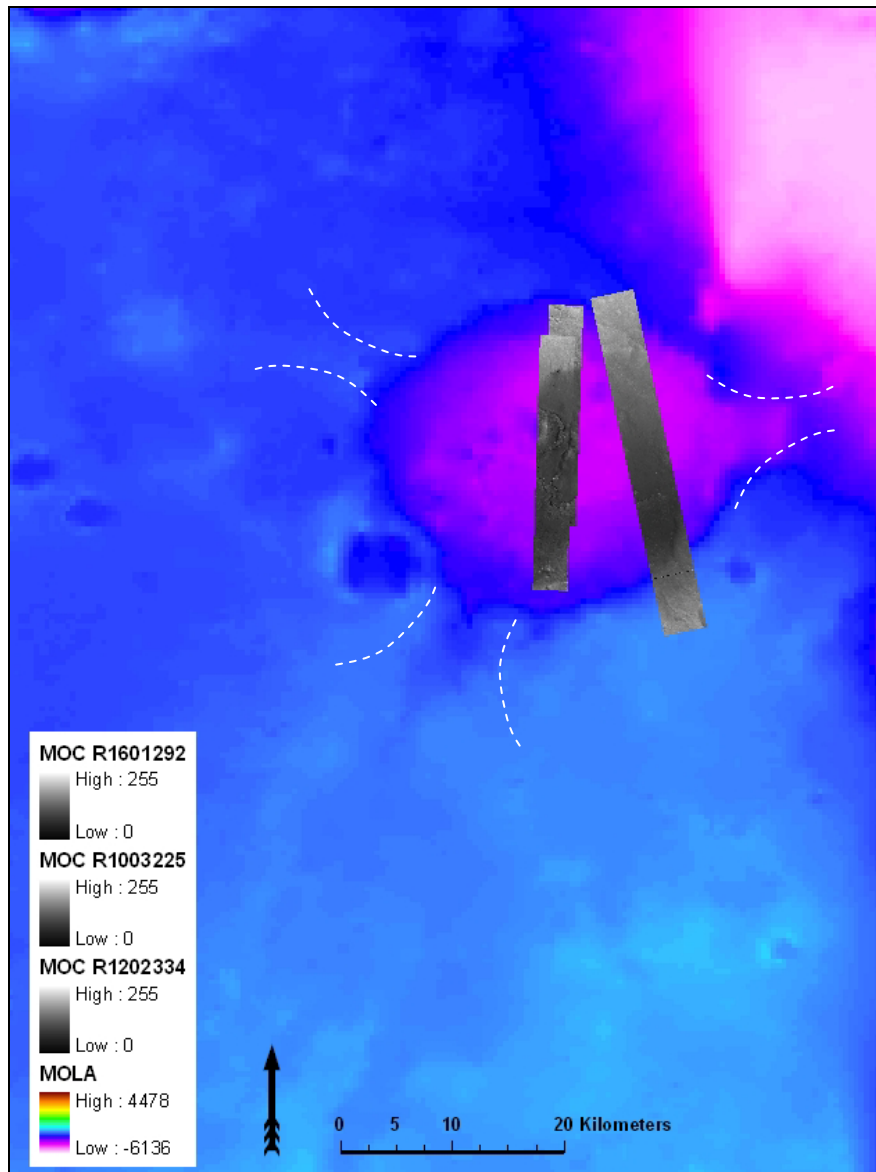


Fig. 52. Composite image for Crater 55 with MOLA base map and MOC narrow-angle images as high-resolution overlays.

Crater 55 has a total score of 0.7, as most of the craters in category type II. In Fig. 52, the radial gullies are the most remarkable features of this candidate crater (shown in dashed white lines). The gullies are not visible in any of the MOC images, but the MOLA topography has a high enough resolution to show these features. One large gully enters the crater from the southwest and is likely responsible for the large resurge deposit located in the southwestern section of the crater. The central terrace is shown in Fig. 53, indicated as feature A. Slumping is not common in this crater, but wet mass movement is observed in the form of debris flows in the south (B). Rim collapse is evident wherever gullies enter the crater depression, and also directly east of the crater's center (refer back to Fig. 52).

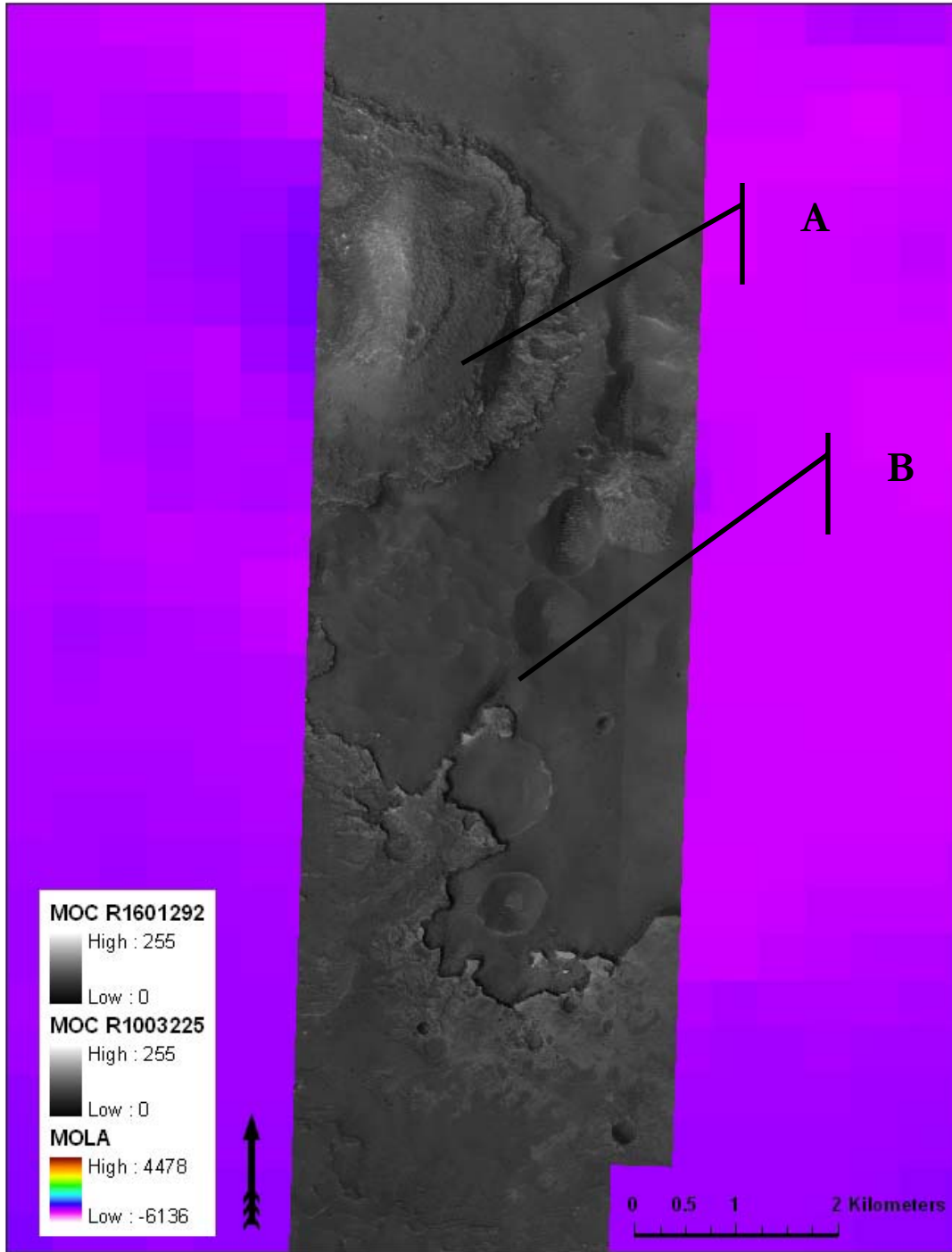


Fig. 53. Close-up of Fig. 52 showing MOC image overlay. Features labeled A and B are mentioned in the text above.

Crater 55 is also roughly 37 km in diameter, similar to Crater D and 54, and thus joins these craters in the medium class (30-50 km diameter). A profile of this crater is shown in Fig. 54. Craters 45, 54, and 55 all have low  $d/D$  ratios of around 0.02.

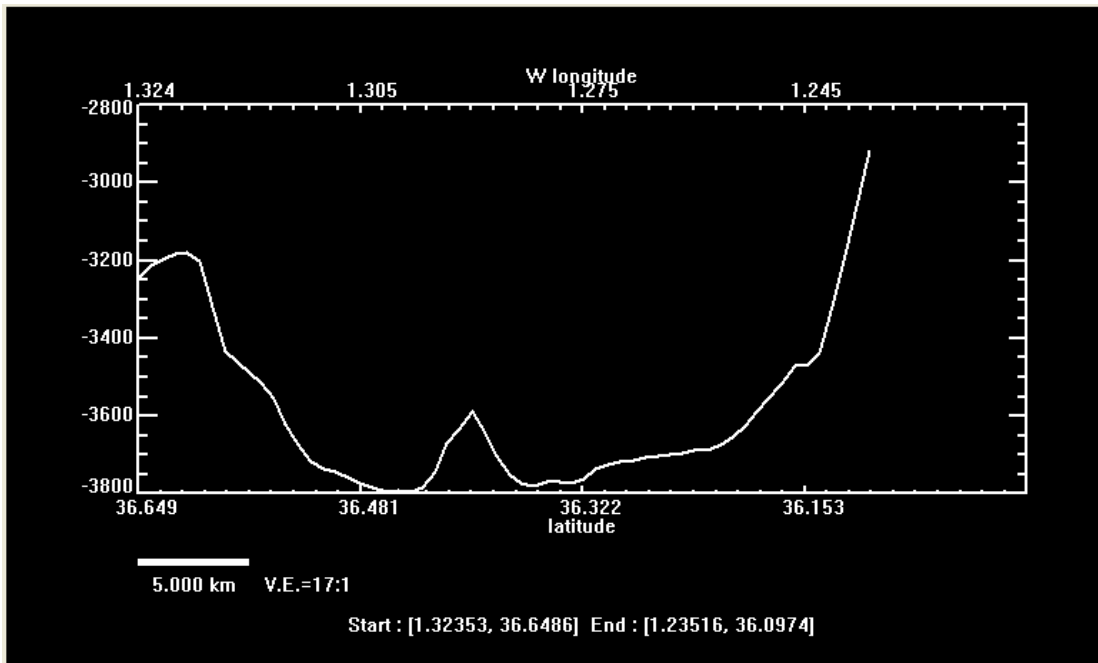


Fig. 54. Profile view of Crater 55 showing varying depth (in km) with variation in latitude (in degrees) from north to south. Vertical exaggeration is 17:1.

From the profile shown in Fig. 54 one can see a central uplift as well as the evidence of slumped units on both the northern and southern parts of the crater rim. The average change in elevation between the surrounding topography and the crater floor is 700m. The southern half of the profile also shows a terraced sedimentary unit, likely deposited by the gully entering from the southwest.

## Type III candidates

### *Crater 58*

Crater 58 is located at roughly 27.38°N and 353.95°W, the farthest south of all of the exemplary candidates. It is in a class of its own because of its large size and because of its relative location to the shorelines and other candidates. It falls within the Meridiani shoreline, but is not even close to the Arabia shoreline, thus decreasing its chances of having formed in an oceanic setting. THEMIS images are overlain on top of the MOLA base map to create a layered image with high-resolution features (Fig. 55).

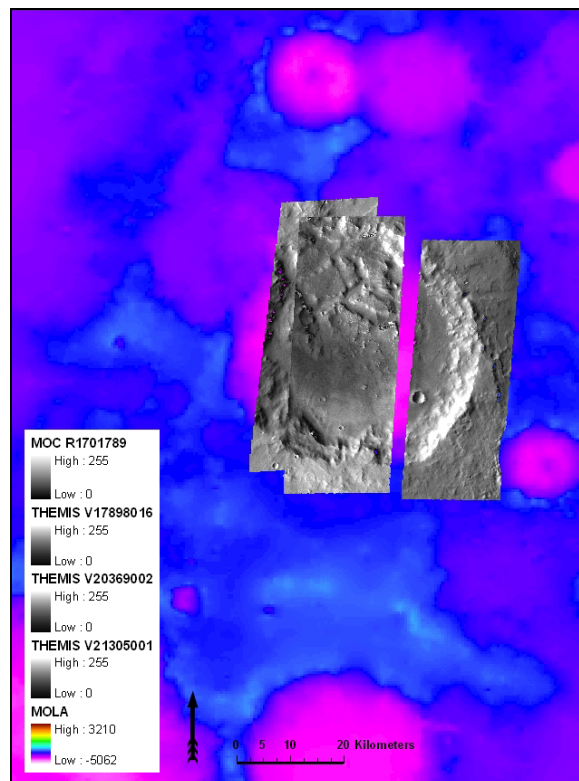


Fig. 55. Composite image for Crater 58 with MOLA base map and MOC wide and narrow-angle images as high-resolution overlays.

Crater 58 has a total score of 0.75. Despite its southern location, numerous indicative features are found in this structure Fig. 56 shows the resurge unit that enters the crater structure from the north (labeled A). This resurge unit has been subsequently modified and eroded. This is in accord with assumed age of the craters in this crater population. Radial gullies seem to enter the crater from a few different areas, mainly from the north (shown with white dashed lines). The MOLA topography indicates a large low-lying area directly to the north of this crater, and the rim in this vicinity is totally collapsed. Rim collapse indicates resurge, and the relative location of the crater with respect to the proposed shorelines make this a likely scenario. Features of wet mass movement are also present in both the form of slumping of the crater wall as well as debris flows, but these features are not well defined in this crater.



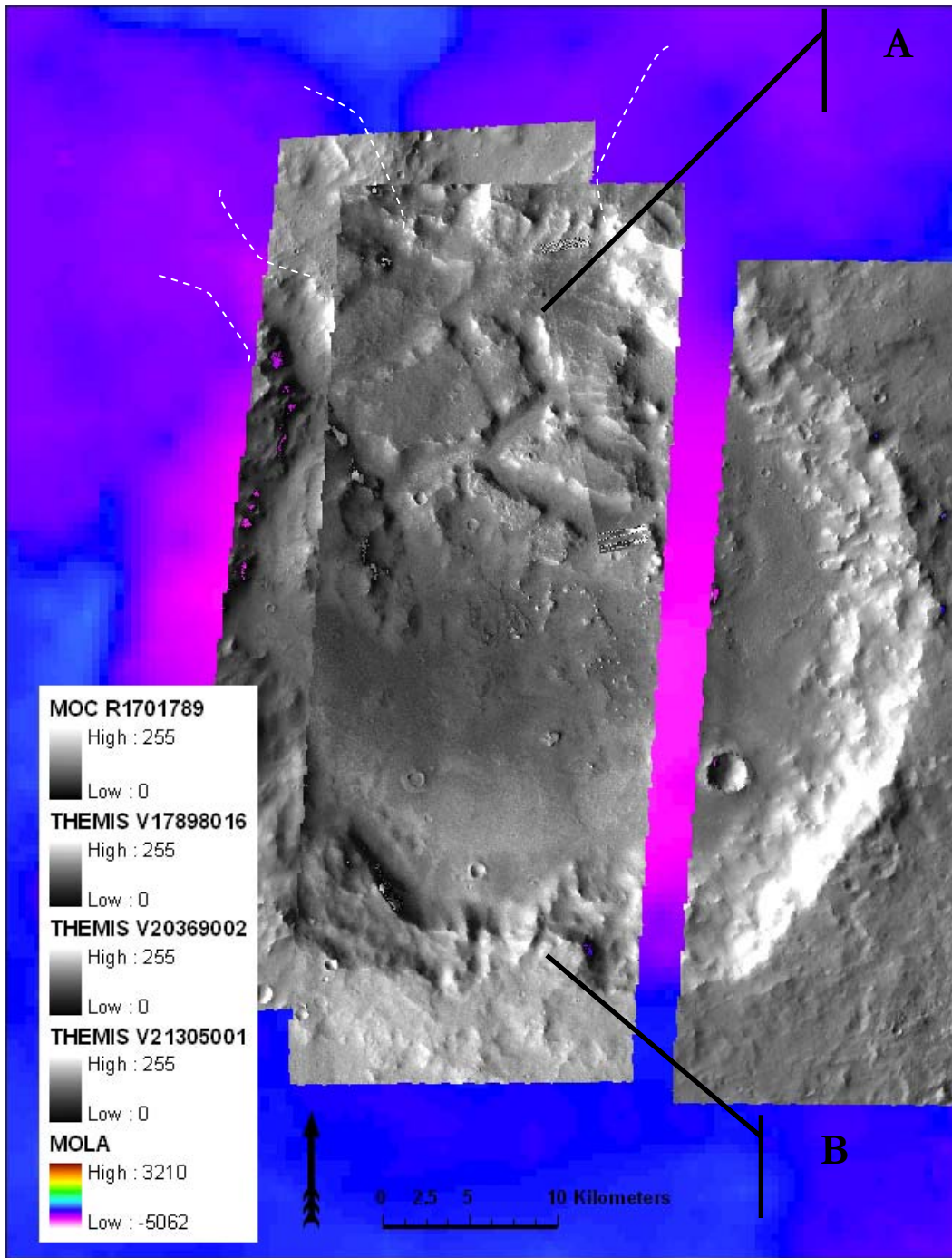


Fig. 56. Close-up of Fig. 54 showing MOC and THEMIS image overlay on top of MOLA topography. Features labeled A and B are discussed in the text. Radial gullies are indicated with white dashed lines.

Crater 58 is roughly 60 km in diameter and is the only exemplary candidate that falls in the large class (50-100 km diameter). A north-south profile of Crater 58 is shown in Fig. 57. From the profile shown in Fig. 57 one can see resurge deposit in the northern half of the crater. The rim here is largely destroyed. This resurge unit is likely responsible for the crater's low d/D ratio of around 0.02. The topography is subdued, particularly in the north.

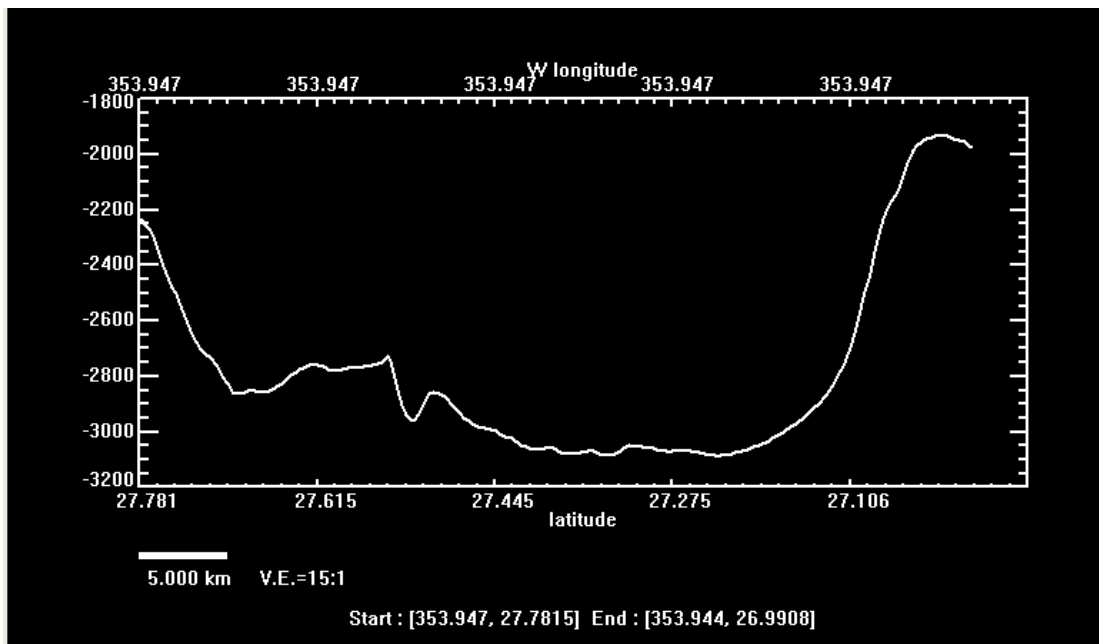


Fig. 57. Profile view of Crater 58 showing varying depth (in km) with variation in latitude (in degrees) from north to south. Vertical exaggeration is 15:1.

## Summary

Spatial correlation with the different types of candidates was not investigated in detail. However, based on only the nine exemplary candidates, there seems to be a direct correlation between location of the crater and its rating. Type I candidates are located in close proximity to the Arabia shoreline; and type II candidates are located a small distance away from the Arabia shoreline, in the direction of the Meridiani shoreline (see Fig. 58). In Fig. 58, Type I candidates are shown in blue, Type II candidates in green, and the single Type III candidate in red. It is impossible to comment on the spatial distribution of type III craters since there is only one. Based on the spatial distribution of the exemplary candidates, it seems more likely that the Arabia shoreline, instead of the Meridiani shoreline, was in fact the shoreline of the ancient Noachian ocean.

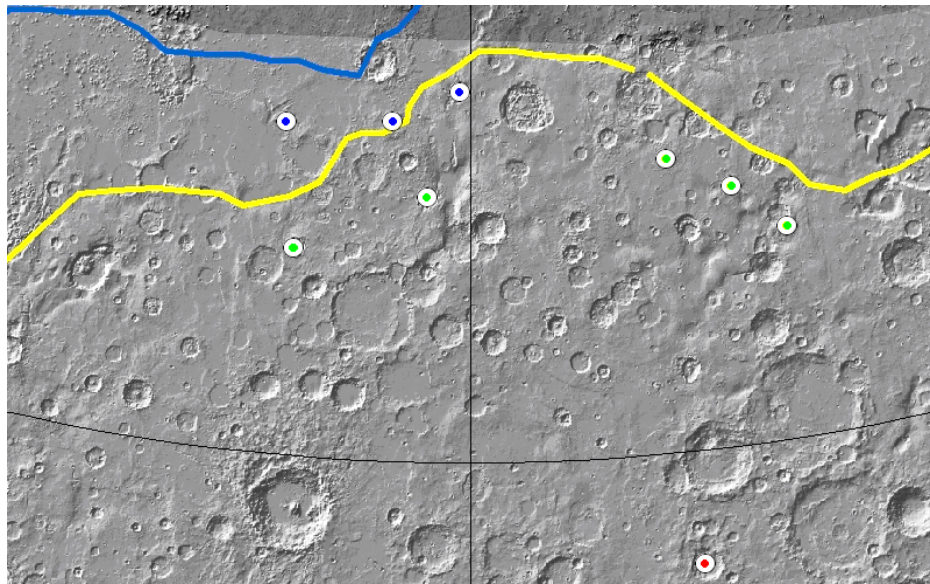


Fig. 58. Spatial distribution of candidate craters shown by type. Type I craters are shown in blue, type II craters shown in green, and type III craters shown in red.

Low depth-diameter ratio values were calculated for all of the exemplary candidates. The values may be anomalous, but low values are expected, especially if large amount of resurge deposition filled the crater shortly after formation.

Based on the quantification system designed in this study, nine craters were rated with total scores of 70% or higher and are subsequently classified as exemplary candidates. All of these craters exhibit signs of slumping, rim collapse and subdued topography. Furthermore, 77% of the exemplary candidates show signs of debris flows and resurge deposits, and 66% have radial gullies and/or central terraces.

## CONCLUSIONS

This study found 77 impact craters in the area of Arabia Terra on Mars that potentially formed in a shallow-marine environment. These craters are identified based on high-resolution imagery data from Mars Orbiter Camera (MOC) and Thermal Emission Imaging Spectrometer (THEMIS), in combination with topographic data from Mars Orbiter Laser Altimeter (MOLA). The classification and ranking of these craters is based on the presence of certain morphological features identified from shallow-marine craters on earth as well as potential candidates on Mars. A quantification system is designed based on the following features:

- Wet mass movement in the form of slumping (a brittle movement) and flowing (a ductile movement) as a result of sediment weakness induced by saturation
- Radial gullies or channels carved by sediment-loaded waters induced by violent resurge of water almost immediately after crater formation
- Resurge deposits in the form of mixed structural blocks and/or sedimentary deposits related to the return of water, either inside or outside of the crater
- Central terrace or flat-topped central uplifts indicative of marine origin and/or that the structure has been buried under water for some time

- Rim collapse and large amounts of inward collapse due to resurge activity or instability of the rim
- Subdued topography indicative of the amount of erosion that has taken place since formation.

The factors listed above are weighted based on importance to create a quantification system for rating and ranking potential candidates. From the quantification system, nine craters are rated with total scores of 0.7 or higher and are subsequently classified as exemplary candidates. All of these craters exhibit signs of slumping, rim collapse and subdued topography; suggesting that these features may be most important in shallow marine impact craters. Furthermore, 77% show signs of debris flows and resurge deposits, and 66% have radial gullies and/or central terraces.

The exemplary candidates are classified into three groups or types. Type I includes well-developed, mostly medium-sized examples; type II includes typical small and medium examples; and type III includes other large potential candidates. Three of the nine craters fall in the type I group; a further five falls in the type II group; and one falls within the type III group.

The results of this study are useful in helping develop a general classification and characterization of potential marine craters. However, a few limitations should be considered:

- The images either show a large amount of detail with very little context, or good context but little detail
- Many of the features that have been listed as characteristics of shallow-marine impact craters can also be formed in other ways and are therefore not entirely predictive
- Not much is known about the geomorphology of terrestrial shallow-marine impact craters, particularly from a remote-sensing point of view, and thus it is hard to compare terrestrial analogs with Martian examples.

This study only looked at MOLA, MOC, and THEMIS data for a small part of the Martian surface. Further studies could include the following:

- More imagery is already available with missions such as Mars Express and Mars Reconnaissance Orbiter, and will also be available in the near future with the Mars Phoenix mission that is on its way
- Analysis of spectrographic data of the candidate sites in order to determine composition and to draw conclusions about target material
- Other areas of the proposed shorelines could also be scrutinized for similar craters, as well as areas within large basins that may have been filled with water for extended periods of time.

This study concludes that evidence for potential shallow-marine impact craters can be found on the surface of Mars as exemplified by Arabia Terra.

## REFERENCES

- Abshire J.B., Sun X., and Afzal R.S. 2000. Mars Orbiter Laser Altimeter: receiver model and performance analysis. *Applied Optics* 39(15):2449-2460.
- Aharonson O., Zuber M.T., and Rothman D.H. 2001. Statistics of Mars' Topography from the Mars Orbiter Laser Altimeter: Slopes, Correlations, and Physical Models. *Journal of Geophysical Research* 106(23):723-735.
- Artemieva N.A. and Shuvalov V.V. 2002. Shock metamorphism on the ocean floor (numerical simulations). *Deep-Sea Research II* 49:959-968.
- Arizona State University Thermal Emission Imaging System Database <<http://themis-data.asu.edu/>> (Accessed 25 October 2007)
- Baker V.R. 2001. Water and the martian landscape. *Nature* 412:228-236.
- Baker V.R. 2006. Geomorphological Evidence for Water on Mars. *Elements* 2(3):139-143.
- Barlow N.G. 1993. Depth-diameter ratios for Martian impact craters: Implications for target properties and episodes of degradation. *LPI Technical Report* 93-06 Part 1.
- Barlow N.G. 2006a. Impact craters in the northern hemisphere of Mars: Layered ejecta and central pit characteristics. *Meteoritics and Planetary Science* 41(10):1425-1436.
- Barlow N.G. 2006b. Martian impact craters and their implications for target characteristics. Proceedings, 40<sup>th</sup> ESLAB Symposium – First International Conference on Impact Cratering in the Solar System. pp. 17-25.
- Barlow N.G., Barnes C.W., Barnouin-Jha O.S., Boyce J.M., Chapman C.R., Costard J.M., Craddock R.A., Garvin J.B., Greeley R., Hare T.M., Kuzmin R.O., Mouginiis-Mark P.J., Newsom H.E., Sakimoto S.E.H., Stewart S.T., and Soderblom L.A. 2003. Utilizing GIS in Martian Impact Crater Studies (abstract). Advances in Planetary Mapping Workshop - International Society for Photogrammetry and Remote Sensing.
- Boyce J.M., Mouginiis-Mark P., and Garbeil H. 2005. Ancient oceans in the northern



- lowlands of Mars: Evidence from impact crater depth/diameter relationships. *Journal of Geophysical Research* 110(E03008):15p.
- Canup R.M. and Asphaug E. 2001. Origin of the Moon in a giant impact near the end of the Earth's formation. *Nature* 412:708-712.
- Caplinger M.A., Jensen E., Edgett K., Eliason E.M., and Garcia P.A. 1999. An archive of MGS/MOC imaging data (abstract #1659). 30th Lunar and Planetary Science Conference. CD ROM.
- Carr M.H. 1995. The Martian drainage system and the origin of valley networks and fretted channels. *Journal of Geophysical Research* 100(E4):7479-7507.
- Carr M.H. and Garvin J.B. 2001. Mars Exploration. *Nature* 412:250-253.
- Carr M.H. and Head J.W. III 2003. Oceans on Mars: An assessment of the observational evidence and possible fate. *Journal of Geophysical Research* 108(E5):5042-5050.
- Chapman M.G., 2003. Sub-ice volcanoes and ancient oceans/lakes: A Martian challenge. *Global and Planetary Change* 35:185-198.
- Christensen P.R., Bandfield J.L., Hamilton V.E., Howard D.A., Lane M.D., Piatek J.L., Ruff S.W., and Stefanov W.L. 2000. A thermal emission spectral library of rock-forming minerals. *Journal of Geophysical Research* 105(E4):9735-9739.
- Christensen P.R., Jakosky B.M., Kieffer H.H., Malin M.C., McSween H.Y. Jr., Nealson K., Mehall G.L., Silverman S.H., Ferry S., Caplinger M., and Ravine M. 2004. The Thermal Emission Imaging System (THEMIS) for the Mars 2001 Odyssey Mission. *Space Science Reviews* 110:85-130.
- Christensen P.R. 2006. Water at the Poles and in Permafrost Regions of Mars. *Elements* 2(3):151-155.
- Clifford S.M. and Parker T.J. 2001. The Evolution of the Martian Hydrosphere: Implications for the Fate of a Primordial Ocean and the Current State of the Northern Plains. *Icarus* 154:40-79.
- Collins G.S. and Wünneman K. 2005. How big was the Chesapeake Bay impact? Insight from numerical modeling. *Geology* 33(12):925-928.
- De Villiers G., King D.T. Jr., and Marzen L.J. 2006. A study of Impact Craters on Mars with the use of GIS and Remote Sensing Applications (abstract). 3<sup>rd</sup> Annual GIS Symposium and Workshop.
- Dypvik H. and Jansa L.F. 2003. Sedimentary signatures and processes during marine

bolide impacts: a review. *Sedimentary Geology* 161:309-337.

Dypvik H., Burchell M.J., and Claeys P. 2004. Impacts into Marine and Icy Environments. In *Cratering in marine environments and on ice*, edited by Dypvik H., Burchell M.J., and Claeys P. Berlin: Springer-Verlag. pp.1-20.

Earth Impact Database <<http://www.unb.ca/passc/ImpactDatabase/>> (Accessed: 18 July 2007)

Edgett K.S. and Malin M.C. 2002. Martian sedimentary rock stratigraphy: Outcrops and interbedded craters of northwest Sinus Meridiani and southwest Arabia Terra. *Geophysical Research Letters* 29(24):2179-2183.

Edgett K.S. and Parker T.J. 1997. Water on early Mars: Possible subaqueous sedimentary deposits covering ancient cratered terrain in western Arabia Terra and Sinus Meridiani. *Geophysical Research Letters* 24(24):2897-2900.

Fairén A.G., Dohm J.M., Baker V.R. de Pablo M.A., Ruiz J., Ferris J.C., and Anderson R.C. 2003. Episodic flood inundations of the northern plains of Mars. *Icarus* 165:53-67.

Garvin J.B., Sakimoto S.E.H., Frawley J.J., and Schnetzler C. 2000. North Polar Region Craterforms on Mars: Geometric Characteristics from the Mars Orbiter Laser Altimeter. *Icarus* 144:329-352.

Gault D.E. and Sonnett C.P. 1982. Laboratory simulation of pelagic asteroidal impact: atmospheric injection, benthic topography and the surface wave radiation field. In *Geological Implications of Impacts of Large Asteroids and Comets on the Earth* edited by Silver L.T. and Schultz P.H. Geological Society of America Special Paper 190:69-92.

Geology Web Pages <<http://www.nicholas.duke.edu/eos/geo41/geo41.htm>> (Accessed 7 September 2007)

Gersonde R., Kyte F.T., Bleil U., Diekmann B., Flores J.A., Gohl K., Grahl G., Hagen R., Kuhn G., Sierro F.J., Volker D., Abelmann A., and Bostwick J.A. 1997. Geological record and reconstruction of the late Pliocene impact of the Eltanin asteroid in the Southern Ocean. *Macmillan Magazines* 390(6658):357-363.

Gersonde R., Deutsch A., Ivanov B.A., and Kyte F.T. 2002. Oceanic impacts – a growing field of fundamental geoscience. *Deep-Sea Research II* 49:951-957.

Ghatan G.J. and Zimbelman J.R. 2006. Paucity of candidate coastal constructional landforms along proposed shorelines on Mars: Implications for a northern lowlands-filling ocean. *Icarus* 185:171-196.

Gooding J.L. 1992. Soil Mineralogy and Chemistry on Mars: Possible Clues from Salts

- and Clays in SNC Meteorites. *Icarus* 99:28-41.
- Grieve R.A.F. 1987. Terrestrial Impact Craters. *Annual Reviews of Earth and Planetary Science* 15:245-270.
- French B.M. 1998. *Traces of Catastrophe: A Handbook of Shock-Metamorphic Effects in Terrestrial Meteorite Impact Structures*. LPI Contribution No. 954, Lunar and Planetary Institute, Houston. 120p.
- Hare T.M. and Tanaka K.L. 2000. Using MOLA and MOC in a GIS (abstract #1907). 31<sup>st</sup> Lunar and Planetary Science Conference. CD ROM.
- Hare T.M. and Tanaka K.L. 2001. Planetary Interactive GIS-on-the-Web Analyzable Database (PIGWAD) (abstract). 20<sup>th</sup> International Cartographic Congress.
- Hare T.M., Tanaka K.L., and Skinner J.A. 2003. GIS 101 for planetary research (abstract). Advances in Planetary Mapping Workshop - International Society for Photogrammetry and Remote Sensing.
- Hartmann W.K. 1966. Martian Cratering. *Icarus* 5:565-576.
- Hartmann W.K. and Davis D.R. 1975. Satellite-Sized Planetesimals and Lunar Origin. *Icarus* 24:504-515.
- Hartmann W.K. and Neukum G. 2001. Cratering Chronology and the Evolution of Mars. *Space Science Reviews* 96:165-194.
- Head J.W. III., Hiesinger H., Ivanov M., Kreslavsky M.A., Pratt S., and Thomson B.J. 1999. Possible Ancient Oceans on Mars: Evidence from Mars Orbiter Laser Altimeter Data. *Science* 286:2134-2137.
- Helfer H.L. 1990. Of Martian Atmospheres, Oceans, and Fossils. *Icarus* 87:228-235.
- Herkenhoff K.E., Squyres S.W., Arvidson R., Bass D.S., Bell J.F. III, Bertelsen P., Ehlmann B.L., Farrand W., Gaddis L., Greeley R., Grotzinger J., Hayes A.G., Hviid S.F., Johnson J.R., Jolliff B., Kinch K.M., Knoll A.H., Madsen M.B., Maki J.N., McLennan S.M., McSween H.Y., Ming D.W., Rice J.R. Jr., Richter L., Sims M., Smith P.H., Soderblom L.A., Spanovich N., Sullivan R., Thompson S., Wdowiak T., Weitz C., and Whelley P. 2004. Evidence from Opportunity's Microscopic Imager for Water on Meridiani Planum. *Science* 306:1727-1730.
- Holsapple K.A. 1993. The scaling of impact processes in planetary sciences. *Annual Reviews of Earth and Planetary Science* 21:333-373.
- Horton J.W. Jr., Ormö J., Powars D.S., and Gohn G.S. 2006. Chesapeake Bay impact structure: Morphology, crater fill, and relevance for impact structures on Mars.

*Meteoritics and Planetary Science* 41(10):1613-1624.

- Howenstein J. 2006. Analysis of the Depth-Diameter Relationship of Martian Craters. A Capstone Experience Thesis, Mount Holyoke College, South Hadley, Massachusetts, USA.
- Ivanov M.A. and Head J.W. 2001. Chryse Planitia, Mars: Topographic configuration, outflow channel continuity and sequence, and tests for hypothesized ancient bodies of water using Mars Orbiter Laser Altimeter (MOLA) data. *Journal of Geophysical Research* 106(E2):3275-3296.
- Johnson R.C. 2007. Wetumpka Impact Structure modeled as the exposed remains of a large, shallow-water, marine-target impact crater for analysis and interpretation of two drill cores taken from near the structure's geographic center. M.S. Thesis, Auburn University, Auburn, Alabama, USA.
- Kenkmann T. and Schönian F. 2005. Impact Craters on Mars and Earth: Implications by Analogy (abstract #3017). 36<sup>th</sup> Lunar and Planetary Science Conference. CD ROM.
- Kennett J.P. 1982. *Marine geology*. Englewood Cliffs: Prentice-Hall. 813p.
- King D.T. Jr., Neathery T.L., Petruny L.W., Koeberl C., and Hames W.E. 2002. Shallow-marine impact origin of the Wetumpka structure (Alabama, USA). *Earth and Planetary Science Letters* 202:541-549.
- King D.T. Jr., Ormö J., Petruny L.W., and Neathery T.L. 2006. Role of water in the formation of the Late Cretaceous Wetumpka impact structure, inner Gulf Coastal Plain of Alabama, USA. *Meteoritics and Planetary Science* 41(10):1625-1631.
- Kirk R.L. 2005. Mars. *Photogrammetric Engineering and Remote Sensing* 71(10):1111-1114.
- Kring D.A. 2005. Hypervelocity collisions into continental crust composed of sediments and an underlying crystalline basement: comparing the Ries (~24 km) and Chicxulub (~180 km) impact craters. *Chemie der Erde* 65:1-46.
- Koeberl C. 2001. Craters on the Moon from Galileo to Wegener: A short history of the impact hypothesis, and implications for the study of terrestrial impact craters. *Earth, Moon and Planets* 85-86:209-224.
- Kreslavsky M.A. and Head J.W. 2006. Modification of impact craters in the northern plains of Mars: Implications for Amazonian climate history. *Meteoritics and Planetary Science* 41(10):1633-1646.
- Leshin L.A. and Vicenzi E. 2006. Aqueous Processes Recorded by Martian Meteorites:

- Analysing Martian Water on Earth. *Elements* 2:159-164.
- Lindström M., Sturkell E.F.F., Ormö J., and Törnberg R. 1996. The Lockne Marine Impact in the Ordovician of Central Sweden. *Meteoritics and Planetary Science* 31:A80-A81.
- Lodders K. 1998. A survey of shergottite, nakhlite and chassigny meteorites whole-rock compositions. *Meteoritics and Planetary Science* 33:A183-190.
- Malin M.C., Danielson G.E., Ingersoll A.P., Masursky H., Veverka J., Ravine M.A., and Soulanille T.A. 1992. The Mars Observer Camera. *Journal of Geophysical Research* 97(E5):7699-7718.
- Malin M.C. and Edgett K.S. 1999. Oceans or seas in the Martian northern lowlands: High resolution imaging tests of proposed coastlines. *Geophysical Research Letters* 26(19):3049-3052.
- Malin M.C. and Edgett K.S. 2000. Evidence for Recent Groundwater Seepage and Surface Runoff on Mars. *Science* 208:2330-2335.
- Malin M.C. and Edgett K.S. 2003. Evidence for Persistent Flow and Aqueous Sedimentation on Early Mars. *Science* 302:1931-1934.
- Malin Space Science Systems Mars Orbiter Camera Database  
<<http://www.msss.com/mgs/moc/index.html>> (Accessed 25 October 2007)
- McSween H.Y. Jr. 2006. Water on Mars. *Elements* 2(3):135-137.
- Melosh H.J. 1980. Cratering Mechanics: Observational, Experimental, and Theoretical. *Annual Reviews of Earth and Planetary Science* 8:65-93.
- Melosh H.J. 1989. *Impact Cratering: A Geologic Process*. New York: Oxford University Press, Inc. 245 p.
- Mouginis-Mark P.J. 1987. Water or Ice in the Martian Regolith? Clues from Rampart Craters Seen at Very High Resolution. *Icarus* 71:268-286.
- NASA 2006. Strategic Plan. National Aeronautics and Space Administration. (NP-2006-02-423-HQ).
- Neumann G.A. 2001. Some aspects of processing extra-terrestrial LIDAR data: Clementine, NEAR, MOLA. *International Archives of Photogrammetry and Remote Sensing* 34:73-80.
- Ormö J. and Lindström M. 2000. When a cosmic impact strikes the sea bed. *Geological Magazine* 137(1):67-80.

- Ormö J. and Muinonen P. 2000. Impact Craters as Indicators for Oceanic Phases on Mars (abstract #1266). 31<sup>st</sup> Lunar and Planetary Science Conference. CD ROM.
- Ormö J., Shuvalov V.V., and Lindström M. 2002. Numerical modeling for target water depth estimation of marine target impact craters. *Journal of Geophysical Research* 107(E12):3-11.
- Ormö J., Dohm J.M., Ferris J.C., Lepinette A., and Fairén A.G. 2004. Marine-target craters on Mars? An assessment study. *Meteoritics and Planetary Science* 39(2):333-346.
- Ormö J., Lindström M., Lepinette A., Martinez-Frias J., and Diaz-Martinez E. 2006. Cratering and modification of wet-target craters: Projectile impact experiments and field observations of the Lockne marine-target crater, Sweden. *Meteoritics and Planetary Science* 41(10):1605-1612.
- Paige D.A. 2005. Ancient Mars: Wet in Many Places. *Science* 307:1575-1576.
- Parker T.J., Saunders R.S., and Schneeberger D.M. 1989. Transitional morphology in the west Deuteronilus Mensae region of Mars: Implications for modification of the lowland/upland boundary. *Icarus* 82:111-145.
- Pike R.J. 1977. Apparent depth/apparent diameter relation for lunar craters. Proceedings, 8<sup>th</sup> Lunar Science Conference. Pp. 3427-3436.
- Pike R.J. 1980. Formation of Complex Impact Craters: Evidence from Mars and Other Planets. *Icarus* 43:1-19.
- Perron J.T., Mitrovica J.X., Manga M., Matsuyama I., and Richards M.A. 2007. Evidence for an ancient martian ocean in the topography of deformed shorelines. *Nature* 447:840-843.
- Pierazzo E. and Melosh H.J. 1999. Hydrocode modeling of Chicxulub as an oblique impact event. *Earth and Planetary Science Letters* 165(2):163-176.
- Poag C.W. 1997. The Chesapeake Bay bolide impact: a convulsive event in Atlantic Coastal Plain evolution. *Sedimentary Geology* 108:45-90.
- Poag C.W., Koeberl C., and Reimold W.U. 2004. *The Chesapeake Bay Crater: Geology and Geophysics of a Late Eocene Submarine Impact Structure*. New York: Springer-Verlag. 522 p.
- Ramsey M.S. and Christensen P.R. 1998. Mineral abundance determination: Quantitative deconvolution of thermal emission spectra. *Journal of Geophysical Research* 103(B1):577-596.
- Reiss D., Hauber E., Ivanov B.A., Michael G., Jaumann R., Neukum G., and The HRSC

- Co-investigator Team 2006. Rampart craters in Thaumasia Planum, Mars: Onset diameters, ages, and implications for the Hesperian hydrology. *Geophysical Research Abstracts* (volume 8 abstract #06506). 3<sup>rd</sup> European Geoscience Union General Assembly.
- Roark J.H., Masuoka C.M., and Frey H.V. 2004. GRIDVIEW: Recent improvements in research and education software for exploring Mars topography (abstract #1833). 35<sup>th</sup> Lunar and Planetary Science Conference. CD ROM.
- Schaefer F., Thoma K., Behner T., Nau S., Kenkman T., Wünneman K., Deutsch A. and the MEMIN-Team 2006. Impact experiments on dry and wet sandstone. *Proceedings, 40<sup>th</sup> ESLAB Symposium – First International Conference on Impact Cratering in the Solar System*. pp. 131-136.
- Schultz P.H. and Lutz A.B. 1988. Polar wandering of Mars. *Icarus* 73:91-141.
- Sharp R.P. 1968. Surface Processes Modifying Martian Craters. *Icarus* 8:472-480.
- Shuvalov V.V. and Trubestkaya I.A. 2002. Numerical Modeling of Marine Target Impacts. *Solar System Research* 36(5):417-430.
- Smith D.E., Zuber M.T., Frey H.V., Garvin J.B., Head J.W., Muhleman D.O., Pettengill G.H., Phillips R.J., Solomon S.C., Zwally H.J., Banerdt W.B., and Duxbury T.C. 1998. Topography of the Northern Hemisphere of Mars from the Mars Orbiter Laser Altimeter. *Science* 279:1686-1692.
- Smith D.E., Zuber M.T., Frey H.V., Garvin J.B., Head J.W., Muhleman D.O., Pettengill G.H., Phillips R.J., Solomon S.C., Zwally H.J., Banerdt W.B., Duxbury T.C., Golombek M.P., Lemoine F.G., Neumann G.A., Rowlands D.D., Aharonson O., Ford P.G., Ivanov A.B., Johnson C.L., McGovern P.J., Abshire J.B., Afzal R.S., and Sun X. 2001. Mars Orbiter Laser Altimeter: Experiment summary after the first year of global mapping of Mars. *Journal of Geophysical Research* 106(23):689-722.
- Smith D.E., Neumann G., Arvidson R.E., Guinness E.A., and Slavney S. 2003. Mars Global Surveyor Laser Altimeter Mission Experiment Gridded Data Record. NASA Planetary Data System, MGS-M-MOLA-5-MEGDR-L3-V1.0.
- Solomon S.C., Aharonson O., Aurnou J.M., Banerdt W.B., Carr M.H., Dombard A.J., Frey H.V., Golombek M.P., Hauck S.A. II, Head J.W. III, Jakosky B.M., Johnson C.L., McGovern P.J., Neumann G.A., Phillips R.J., Smith D.E., and Zuber M.T. 2005. New Perspectives on Ancient Mars. *Science* 307:1214-1220.
- Squyres S.W. 1989. Water on Mars. *Icarus* 79:229-288.
- Squyres S.W., Grotzinger J.P., Arvidson R.E., Bell J.F. III, Calvin W., Christensen P.R., Clark B.C., Crisp J.A., Farrand W.H., Herkenhoff K.E., Johnson J.R.,

- Klingelhöfer G., Knoll A.H., McLennan S.M., McSween H.Y. Jr., Morris R.V., Rice J.W. Jr., Rieder R., and Soderblom L.A. 2004. In Situ Evidence for an Ancient Aqueous Environment at Meridiani Planum, Mars. *Science* 306:1709-1714.
- Squyres S.W., Knoll A.H., Arvidson R.E., Clark B.C., Grotzinger J., Jolliff B.L., McLennan S.M., Tosca, N., Bell J.F. III, Calvin W.M., Farrand W.H., Glotch T.D., Golombek M.P., Herkenhoff K.E., Johnson J.R., Klingelhöfer G., McSween H.Y. Jr., and Yen A.S. 2006a. Two Years at Meridiani Planum: Results from the Opportunity Rover. *Science* 313:1403-1407.
- Squyres S.W., Aharonson, O., Arvidson R.E., Bell J.F. III, Christensen P.R., Clark B.C., Crisp J.A., Farrand W.H., Glotch T., Golombek M.P., Grant J., Grotzinger J., Herkenhoff K.E., Johnson J.R., Jolliff B.L., Knoll A.H., McLennan S.M., McSween H.Y. Jr., Moore J.M., Rice J.W. Jr., and Tosca N. 2006b. Planetary Science: Bedrock formation at Meridiani Planum. *Nature* 443:E1-E2.
- Sturkell E.F.F, Ekelund, A., and Törnberg, R. 1998. Gravity modeling of Lockne, a marine impact structure in Jämtland, central Sweden. *Tectonophysics* 296:421-435.
- Suspected Earth Impact Sites Database  
<[http://web.eps.utk.edu/ifsg\\_files/SEIS/SEIS\\_introduction5.pdf](http://web.eps.utk.edu/ifsg_files/SEIS/SEIS_introduction5.pdf)> (Accessed: 19 July 2007)
- Tanaka K.L., Skinner J.A. Jr., and Hare, T.M. 2005. Geologic Map of the Northern Plains of Mars. Prepared for the National Aeronautics and Space Administration by the United States Geological Survey to accompany *Scientific Investigations Map* 2888. 32p.
- Tsikalas F., Gudlaughsson S.T., and Faleide J.I. 1998. The anatomy of a buried complex impact structure: The Mjøltnir Structure, Barents Sea. *Journal of Geophysical Research* 103:30469-30484.
- Venechuk E.M., Allen C.C., and Oehler D.Z. 2005. Layers, bright rim craters, and faulting in the Arabia Terra, Mars. Proceedings, 21<sup>st</sup> LPI Summer Intern Conference. pp.34-36.
- Von Dalwigk I. and Ormö J. 2001. Formation of resurge gullies at impacts at sea: The Lockne crater, Sweden. *Meteoritics and Planetary Science* 36:359-369.
- Wohletz K.H. and Sheridan M.F. 1983. Martian Rampart Crater Ejecta: Experiments and Analysis of Melt-Water Interaction. *Icarus* 56:15-37.
- Wright S.P. 2003. Thermal infrared data analyses of Meteor Crater, Arizona: Implications for Mars spaceborne data from the Thermal Emission Imaging



- System. M.S. Thesis, University of Pittsburgh, Pittsburgh, Pennsylvania, USA.
- Wünnemann K. and Lange M.A. 2002. Numerical modeling of impact-induced modifications of the deep-sea floor. *Deep-Sea Research II* 49:969-981.
- Wyatt M.B. and McSween H.Y. Jr. 2006. The Orbital Search for Altered Materials on Mars. *Elements* 2(3):145-150.
- Zuber M.A. 2007. Mars at the tipping point. *Nature* 447:785-786.